FINAL REPORT

For the U.S. Department of Transportation Solicitation #DTPH56-07-BAA-000002
Under Contract Number DTPH56-08-T-000009

ADAPTATION OF MWM-ARRAY AND MFL TECHNOLOGY FOR ENHANCED DETECTION/CHARACTERIZATION OF DAMAGE FROM INSIDE PIPELINES

Prepared for

James Merritt
U.S. Department of Transportation
Pipeline and Hazardous Materials Safety Administration
Office of Pipeline Safety
793 Countrybriar Lane
Highlands Ranch, CO 80129

By JENTEK Sensors, Inc.
110-1 Clematis Avenue
Waltham, Massachusetts 02453-7013
(781) 642-9666
jentek@shore.net

March 26, 2012

Table of Contents

1 EXECUTIVE SUMMARY 3
2 INTRODUCTION 4
3 PROJECT TASKS 4
4 IMPACT FROM RESEARCH RESULTS SECTION 5
5 FINAL FINANCIAL SECTION 6
6 DETAILED TECHNICAL RESULTS 6
6.1 MWM and MWM-Arrays 6
6.2 Measurement Grid Methods 12
6.3 Scanning fixtures 15
6.3.1 External scanners 15
6.3.2 Internal scanners 17
6.4 Demonstration Results 20
6.4.1 Near-Surface Corrosion Imaging (External) 20
6.4.1.1 Initial measurements on flat plates 20
6.4.1.2 Measurements on laboratory pipe sections 26
6.4.1.3 Measurements on a pipe section removed from service 37
6.4.1.4 Measurements on risers 38
6.4.2 In-line inspection imaging (Near-surface material loss from inside the pipeline) 44
6.4.2.1 Initial measurements on laboratory pipe sections 44
6.4.2.2 Pull Test 1 Results 48
6.4.2.3 Pull Test 2 Results 58
6.4.3 Hybrid MFL and MWM-Array methods 71
6.4.3.1 MFL and MWM Feature Comparison 71
6.4.3.2 Hybrid MFL/MWM Investigation 72
6.4.4 Far-Surface Material Loss (Corrosion) Imaging 86
6.4.5 Mechanical Damage Imaging 95
6.5 Technology Transition 99
6.5.1 ILI Tool Requirements 99
6.5.2 Commercialization Plan 99
6.5.3 Development of Industry Standards and Training Information 100
6.5.4 Increased Industry Awareness of the MWM-Array Technology 101
6.5.5 Recommendations for future work 101
6.6 References 102

1 Executive Summary

This report describes the results of a development project aimed at providing rapid nondestructive evaluation (NDE) methods for the detection of damage in carbon steel pipelines from the inside through coatings and liners. This was accomplished by adapting JENTEK's MWM-Array technology to accommodate the coating and liner thicknesses and properties typically used in the oil and gas industry and mounting the MWM-Arrays to prototype scanning fixtures for demonstrating an inspection capability from inside the pipeline. The MWM-Array uses a time-varying magnetic field to induce eddy-currents in the steel components and detects variations in the magnetic field due to damage in the steel component. This technology has been successfully applied in the aerospace and manufacturing industries and provides substantially improved performance for imaging surface and buried damage through coatings and for curved surfaces compared to conventional NDE methods. This project has demonstrated the feasibility of using the MWM-Array technology as an NDE tool for inspection of steel pipelines from inside the pipeline. We are confident that a fieldable solution based on this technology will be available in the near-future.

This project has achieved a number of milestones toward establishing the feasibility of integrating MWM-Array technology into In-Line Inspection (ILI) tools for detection and characterization of damage from inside the pipelines. These results include:

- Demonstrated high spatial imaging resolution for near-surface material loss damage through non-conducting coatings using MWM-Arrays in the laboratory.
- Demonstrated capability to image mechanical damage through non-conducting coatings.
- Fabricated several large flexible MWM-Arrays to image damage through coatings and liners.
- Fabricated prototype ILI tools to facilitate imaging steel component material condition from inside the pipeline.
- Performed two pull tests to demonstrate imaging of near-surface damage with MWM-Arrays with integrated impedance measurement instrumentation.
- Performed a series of simulations to demonstrate adaptation of MWM-Array technology to enhance MFL operation.
- Performed measurements with a hybrid MFL/MWM-Array design which demonstrated successful MWM-Array operation in the presence of magnet bias fields.
- Fabricated a large flexible MWM-Array with solid-state sense elements to support low frequency operation.
- Demonstrated feasibility of independently measuring steel magnetic relative permeability, steel thickness, and lift-off for steel plates up to 6.35 mm (0.25-in.) thick. This low-frequency measurement capability allows near-surface and far-surface material loss to be separately identified.
- Performed finite element simulations for sensor array responses over discrete areas of material loss to confirm observed measurement responses and provide means for compensating for flaw geometry effects on material loss depth estimates.

These results have demonstrated that the model-based methods and high spatial imaging resolution capabilities of the MWM-Array technology can be integrated into ILI tools. Recommendations for future work leading to commercial application of this technology in ILI tools include expanding the instrument capabilities for complete circumferential coverage by increasing the number of data acquisition channels and increasing the data acquisition rates, extending capabilities of the impedance measurement instrumentation to lower operating frequencies to accommodate thicker steel walls and metallic coatings, hardening of the instrumentation for field operation including sealing for protection in harsh environments, and demonstrating fieldable capabilities in a flow loop.

2 Introduction

The combination of ever increasing energy consumption throughout the world and finite non-renewable fossil fuel resources has led the oil and gas industry to seek hydrocarbon products in relatively harsh environments. These hydrocarbon products often contain highly corrosive components at high temperatures and new internal coatings and liners are being applied to prevent corrosion and damage. Example coatings include metallic corrosion resistant alloys and example non-metallic liners include high density polyethylene. With a typical coating or liner thickness of 0.125 to 0.15-in., these materials can help to mitigate/prevent damage from occurring, but they also make inspections of the pipeline wall more difficult. Conventional in-line inspection (ILI) methods, such as magnetic flux leakage (MFL) have a limited ability to reliably inspect through such coatings and liners. In addition, with the emergence of newer ILI platforms that can perform inspections during and against flow, new sensor technology is needed to provide enhanced assessment of the extent and type of damage in pipelines.

In this project, JENTEK's novel Meandering Winding Magnetometer (MWM®) Array technology was adapted to provide an improved method for detection and characterization of damage in pipelines, from inside the pipelines. This magnetic field-based sensor technology has been successfully applied in the aerospace and manufacturing industries and provides substantially improved performance for imaging surface and buried damage through coatings and for curved surfaces compared to conventional NDE methods [1-5]. Here, the sensor arrays and JENTEK's model-based inverse methods were used to determine electromagnetic and geometric properties of the pipeline material, which are then related to specific damage conditions of interest. The team for this project was JENTEK, Chevron, NDT Systems and Services, and Applus/RTD.

3 Project Tasks

This project was part of a consolidated contract aimed at developing instrumentation for characterizing damage in pipelines, including external corrosion, internal corrosion, stress corrosion cracking (SCC), and mechanical damage, with one set of tasks (No. 304) for inspection from outside the pipeline and another (this project, No. 306) for inspection from inside the pipeline. Funding for this project and the consolidated contract is complemented by funding from Chevron on a program titled "Development of Enhanced Inspection Tool through Protective Barriers."

The following summarizes the tasks associated with this project.

Task 1: Develop and demonstrate capability to image internal corrosion and mechanical damage with and without liners/coatings using high frequency MWM-Array eddy current technology.

Task 2: Investigate low-frequency MWM-Array capability for inspection through typical pipeline wall thicknesses and liners, and demonstrate preliminary capability for enhanced imaging of either mechanical damage, external SCC, or external corrosion.

Task 3: Evaluate the benefits of MFL and MWM-Array methods independently and investigate integration of these methods for use on a selected ILI platform. This task will also include an investigation into the use of JENTEK multivariate inverse methods to enhance MFL designs and performance.

Task 4: Develop a detailed plan for the field measurements to be performed during the option Demonstration Program.

Task 5: Develop commercialization plans for transition of the developed and demonstrated capabilities into near-term use.

Task 6: Submit quarterly reports, recommendations for the optional field demonstration(s), and a final report.

Task 7: Perform one (or more, depending on platform provider resource and matching fund commitments) field capability demonstration, including preliminary integration with a conventional pig for piggable lines, or with a suitable platform for unpiggable lines.
Task 8: Develop input for training manuals and standards.
Task 9: Expand demonstration scope to allow additional support from ILI OEMs.
Task 10: Evaluate transition requirements for integration with ILI tools.

The first year of the project was aimed at demonstrating an imaging capability for near-surface (internal) corrosion and damage with and without liners or coatings in the laboratory. The second year was aimed at extending the capability to permit damage inspection through thicker coatings and/or external damage from the inside. The third year was aimed at performing a predemonstration field inspection and developing commercialization and transition plans. The fourth year, as part of the expansion effort, was aimed at performing an enhanced field inspection demonstration capability.

4 Impact from Research Results Section

Eddy current technology is widely used in the aerospace industry and is expected to experience increasing use in petrochemical applications because new eddy current sensor arrays permit rapid and reliable imaging of pipeline material condition. The emphasis of the technology development in this project was on inspection through coatings, but the methods can also be applied to inspections with coatings removed. Both with and without coatings, these methods can provide information about the material condition that can assist with characterization of damage conditions and support assessment decisions. This project helped to establish the capabilities of imaging eddy current sensor arrays for damage inspection and characterization through coatings. This was accomplished through adaptation of the MWM-Array eddy current sensor technology for pipeline materials and preliminary capability demonstration measurements in a pair of pull tests.

To accommodate the desired spatial resolution for the inspection, the sensor array lift-off (proximity to the pipeline wall surface), the thickness of the pipeline wall, and the presence of coatings or liners, the sensor design and operating conditions can be adjusted. For example, to inspect through thin pipeline walls and thin coatings or liners, a sensor design with a geometry (e.g., spatial wavelength) that is comparable to the thickness should be used. A sensor with a geometry that is too small would not be able to inspect through the coating and a sensor with a geometry that is too large would have reduced sensitivity to the presence of small features. Similarly, the operating frequency of the instrumentation can be adjusted to accommodate different inspection requirements. Since the induced eddy current density varies with the excitation frequency and is largest on the steel surface nearest the sensor, high excitation frequencies are typically used for near-surface damage inspections. For inspections through the steel wall, for example for internal corrosion damage with an external inspection, low excitation frequencies are required.

This research advances pipeline safety by providing improved inspection capabilities for damage from inside the pipelines. The technology gaps addressed by this program included: 1) high resolution imaging of internal damage for gas pipelines; 2) higher resolution images of external damage for oil and gas pipelines; 3) stress imaging around mechanical damage sites; and 4) an ability to account for interferences/external structures. This research program provided significant advances toward addressing these gaps. However, additional development work is required for hardening of the instrumentation for field operation, expanding the instrument capabilities to complete circumferential coverage, extending capabilities of the impedance measurement instrumentation to lower operating frequencies to accommodate thicker steel walls and metallic coatings, and demonstrating fieldable capabilities in a flow loop.

5 Final Financial Section

This section reviews the financing associated with this project. Table 1 shows that the matching requirements for the project were satisfied. Note that this project was part of a consolidated program with DOT Project 304 and the total amount from partner cost sharing for the consolidated program through the Chevron "Inspection through protective barriers" program as well as Chevron internal expenses was $1,231,301. Of this amount, $676,301 is recognized for cost sharing in Project 306 and the remainder ($555,000.) was recognized as cost sharing in Project 304.

Table 1. Project Funding Summary.

Project	Abbreviated Title	Expenditures	
		As of 11/30/11	Anticipated by end of Project 306
DOT 306	Inspection from inside pipeline	$629,176.	$632,393.
Partner cost sharing	Chevron "Inspection through protective barriers" program plus Chevron internal expenses	$676,301.	$676,301.
Total		$1,305,477.	$1,308,694.

6 Detailed Technical Results

This section reviews the basic geometry for the MWM and MWM-Arrays, the multivariate inverse methods for converting measurement data into meaningful material and geometric properties, the scanning fixtures developed for use with these sensor arrays, results from numerous demonstration measurements, and issues for transitioning the technology into widespread field-use.

6.1 MWM and MWM-Arrays

MWM and MWM-Arrays are inductive, eddy-current-based sensors that are conformable and provide inspection and monitoring capabilities for conducting materials, such as steel pipeline walls and drill pipe [6]. MWM and MWM-Array technology is covered by numerous U.S. patents including 5,453,689; 5,629,621; 5,793,206; RE39,206; 7,049,811; 7,467,057; and 7,589,526. These patents cover not only the MWM and MWM-Array winding construct, but also the multivariate inverse methods and related calibration and measurement procedures. As shown in Figure 1, the original MWM sensor geometry had a meandering primary winding for creating a spatially periodic magnetic field when driven by an electrical current – hence the MWM name. Secondary windings (sense elements) are located on opposite sides of the primary for sensing the response.

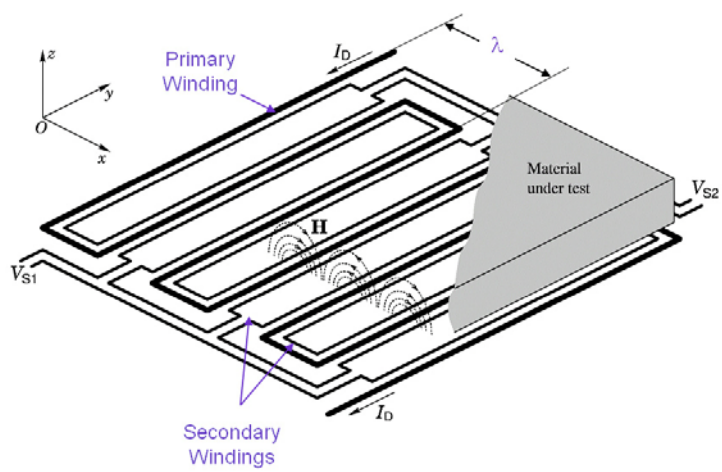

Figure 1. Original MWM sensor geometry [6].

Printed circuit microfabrication techniques are typically employed to produce the sensors, resulting in highly reproducible (i.e., essentially identical) sensors. By fabricating the windings on a thin and flexible substrate, a conformable sensor is produced. These thin and conformable sensors can be scanned across a surface, mounted on an exposed surface, or embedded within or between coating/pipeline layers or under an overwrap or repair. The relatively simple layout for the windings permits operation over a wide frequency range, typically between 1 kHz and 40 MHz. For inspection through steel pipeline walls, for example for internal corrosion inspection from the outside, a lower frequency capability (<100 Hz) is required.

The depth of penetration of the magnetic field into the test material depends upon both the input current frequency and sensor geometry (drive winding spatial wavelength λ) as shown in Figure 2(left). The penetration depth is limited by the skin depth at high frequencies and by the sensor geometry at low frequencies. At low frequencies the magnetic fields from a larger spatial wavelength sensor will penetrate further into the material under test than the fields from a shorter spatial wavelength sensor. Note that the spatial wavelength λ of Figure 1 indicates the spatial periodicity for the drive. For the MWM-Arrays of Figure 3 the relevant dimension is the gap between the drive and sense element, which is defined as $\lambda/4$ and illustrated in Figure 2(right).

Thus, while small sensor arrays can be used to create high spatial resolution property images, large sensor arrays are required for inspecting through thick materials, either steels, coatings, or insulation. For bare metal or very thin (less than 0.5 mm (0.020-in.)) coatings, very high resolution imaging is achieved with the FA28 MWM-Array of Figure 3(a). The FA24 MWM-Array shown in Figure 3(b) has larger dimensions than that of the FA28 and permits inspection through thin (up to 6.35 mm (0.25-in.)) coatings. As part of this project, larger versions of the MWM-Arrays were fabricated. The VWA001 MWM-Array shown in Figure 3(c) has a variable spatial wavelength, where the distance between the drive winding and sense element can be adjusted, which enables both deep penetration and relatively high resolution compared to other typical low frequency eddy current methods. The VWA003 MWM-Array shown in Figure 3(d) is similar to the VWA001 except that the drive winding and sensor array are smaller, which makes the sensor array easier to use. For comparison, the VWA001 has a 22-in. long drive winding and the linear array contains thirty-seven sense elements that are 6.5 mm (0.25-in.) square to provide a net scan width of 235 mm (9.25-in.), while the VWA003 has a 9-in. long drive winding and the linear array contains fifteen sense elements that are 6.5 mm (0.25-in.) square to provide a net scan width of 97.5 mm (3.75-in.). The VWA005 MWM-Array shown in Figure 3(e) has sense elements similar to the VWA003. However, the connection leads to the sense elements are longer, which allows the sensor array to be placed farther within the VWA003 drive winding and permits larger gaps between the drive winding and sense elements. In addition, a different style of connector is used to connect each sense element to the probe electronics. This connector requires less surface area than the previous connector and is better suited toward use as a sensor array for integration onto an ILI tool where space is limited.

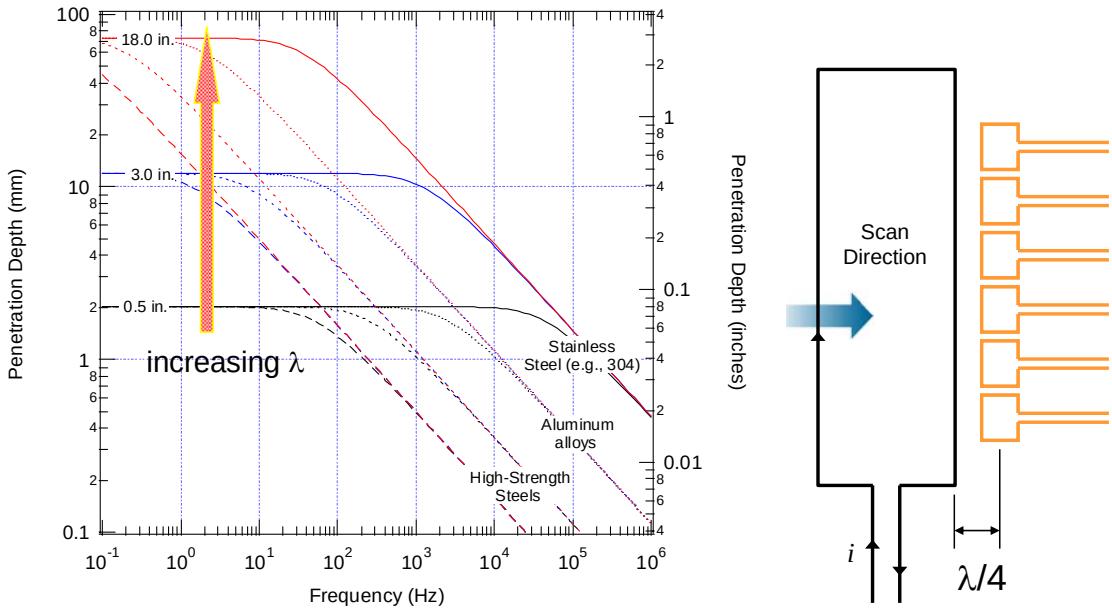

Figure 2. (Left) Depth of penetration variation with sensor dimension. (Right) schematic diagram of a sensor array.

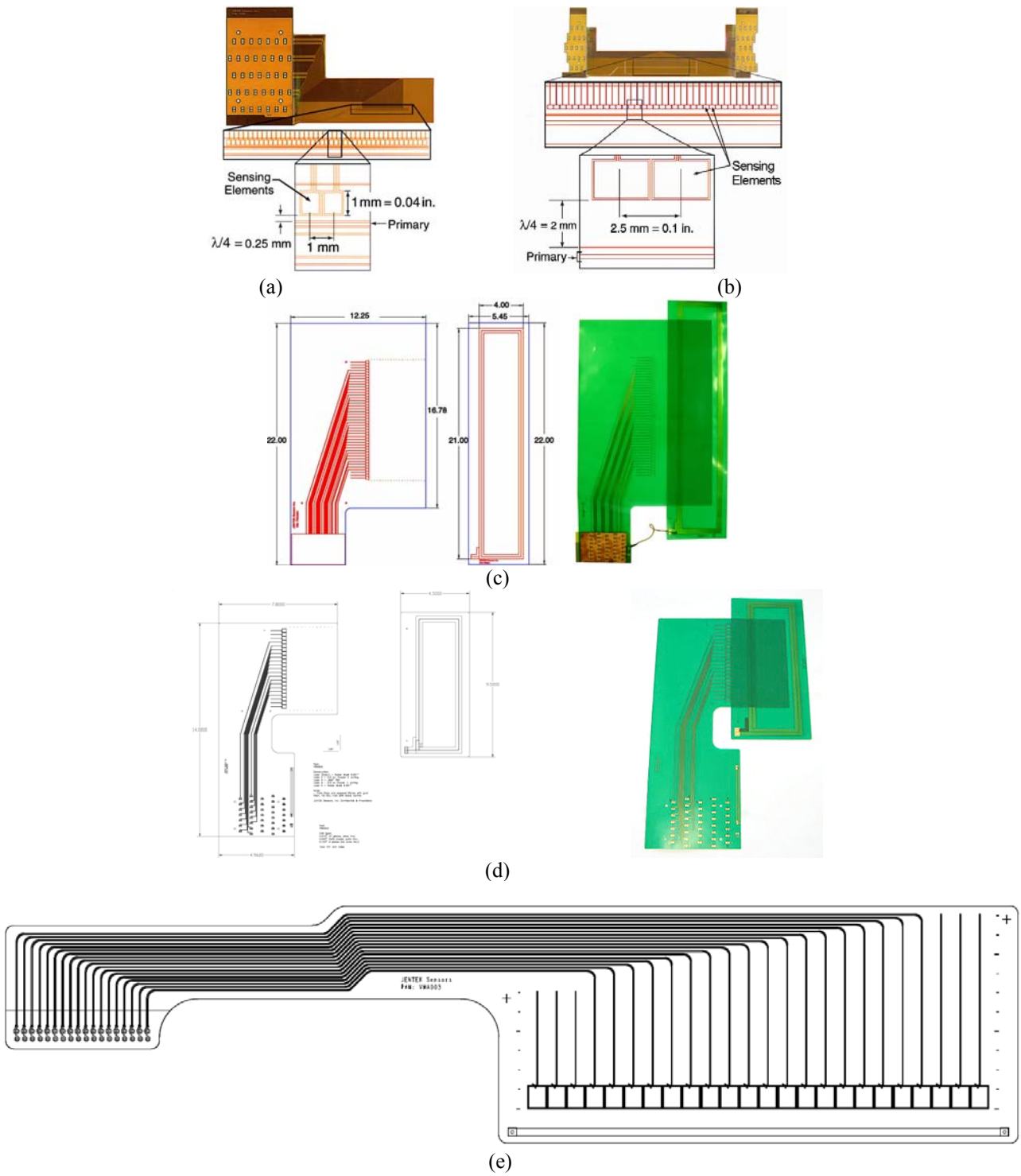

Figure 3. Several MWM-Arrays: (a) FA28; (b) FA24; (c) VWA001; (d) VWA003; and (e) VWA005 [6].

Several simulations were performed to verify that the dimensions of the arrays were reasonable. These simulations also support the use of low frequency sense elements for scanning through the thickness of the steel pipeline walls. For example, one way to estimate the effect of the finite dimensions of the drive winding on the sense element response is to calculate the field variation along the sense

elements when the sensor array is in air. The response in air can be calculated using a "stick-model" for the current carrying wires in the sensor array.

For this analysis, a simplified geometry for the sensor array was used, as shown in Figure 4. For this geometry, assume that the drive winding is a single rectangular loop of dimensions 2*L* and *d* that is placed at a gap distance *g* from a linear array of sense elements. The length of the sense element array is *w*. Assuming that the net current in each leg of the drive winding is *i*, then the current from each segment can be easily evaluated using an algebraic vector form of the Biot-Savart Law for current sticks: [7]

$$\bar{\mathbf{H}} = \frac{i}{4\pi}\frac{\bar{c}\times\bar{a}}{\left|\bar{c}\times\bar{a}\right|^2}\left(\frac{\bar{a}\cdot\bar{c}}{\left|\bar{c}\right|}-\frac{\bar{a}\cdot\bar{b}}{\left|\bar{b}\right|}\right)$$

where, i is the current in the segment, $\bar{b}$ is a vector from the observation point to the start of the segment, $\bar{c}$ is a vector from the observation to the end of the segment, and $\bar{a}=\bar{c}-\bar{b}$. This expression provides the vector magnetic field intensity for arbitrary points around the drive winding. For the analysis here, only the field along the sense element array is to be determined. Assuming that the sensor array is narrower than the drive winding length ($|y|<L$), the field can be expressed as

$$\bar{\mathbf{H}} = \hat{i}_z\frac{i}{4\pi}\left\{\sqrt{\left(\frac{1}{L-y}\right)^2+\left(\frac{1}{g+d}\right)^2}+\sqrt{\left(\frac{1}{L+y}\right)^2+\left(\frac{1}{g+d}\right)^2}-\sqrt{\left(\frac{1}{L-y}\right)^2+\frac{1}{g^2}}-\sqrt{\left(\frac{1}{L+y}\right)^2+\frac{1}{g^2}}\right\}$$

where $\hat{i}_z$ is a unit vector in the *z*-direction. Since the drive winding and sense elements are assumed to be in the same plane (*z*=0), the magnetic field is only in the *z*-direction.

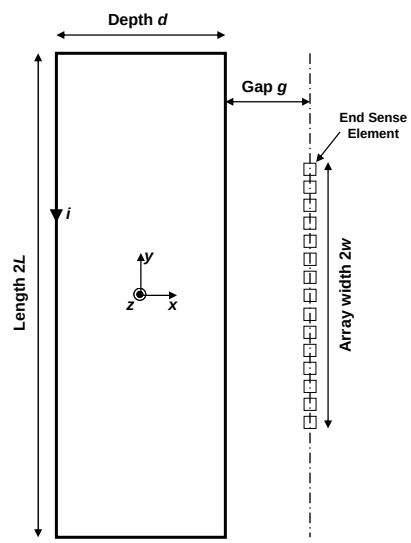

Figure 4. Model geometry for calculating nominal field variation across a linear array of sense elements.

Figure 5 shows the field variation with position along the array of sense elements. The field is at a maximum at the center and decays with position along the array; the field value is normalized to the maximum field at the center of the array. The field is relatively uniform near the center of the array but decreases near the ends of the drive winding. The end effect increases with the gap size and reduces the length over which the field would be considered uniform. Varying the drive winding dimension *d* (or *d/L*) does not have a significant effect on the field distribution in the vicinity of the sense elements; however, this dimension is expected to have an effect on the penetration of the magnetic field through thick coatings or insulation.

Figure 6 shows contour plots of the field variation with gap distance and the end position of the sense element array. The gap distance and sense element array end position are relative to the half-length of the drive winding. The field variation is expressed as a percentage change in the field at the end position of the sense element array compared to the field at the center of the array. The field at the end of the sense element array decreases as the sense element array width and the gap distance becomes large compared to the half-length of the drive winding. For the VWA001, the drive winding is approximately 21-in. long and 4.0-in. wide with a sense element array width of 9.25-in. The drive-sense gap is typically varied from 1.0 to 4.0-in. This yields normalized dimensions of *d/L* =0.381, *w/L* =0.393, and *g/L* from 0.095 to 0.381. From Figure 6, the field variation across the sensor array is less than 5%; since this variation is relatively small, the calibration procedure (air or reference part calibration) is sufficient to remove the baseline variation in the field due to the finite drive winding length.

For comparison, the VWA003 has a drive winding that is approximately 9.0-in. long and 3.0-in. wide with a sense element array width of 3.75-in. that is 1.0-in. from the drive winding. This yields normalized dimensions of *d/L* =0.667, *w/L* =0.417, and *g/L* =0.222. Figure 7 shows the corresponding contour plots of the field variation between the end sense element and the center sense element. For the VWA003, the field variation is expected to be less than 4%, which is comparable to the VWA001.

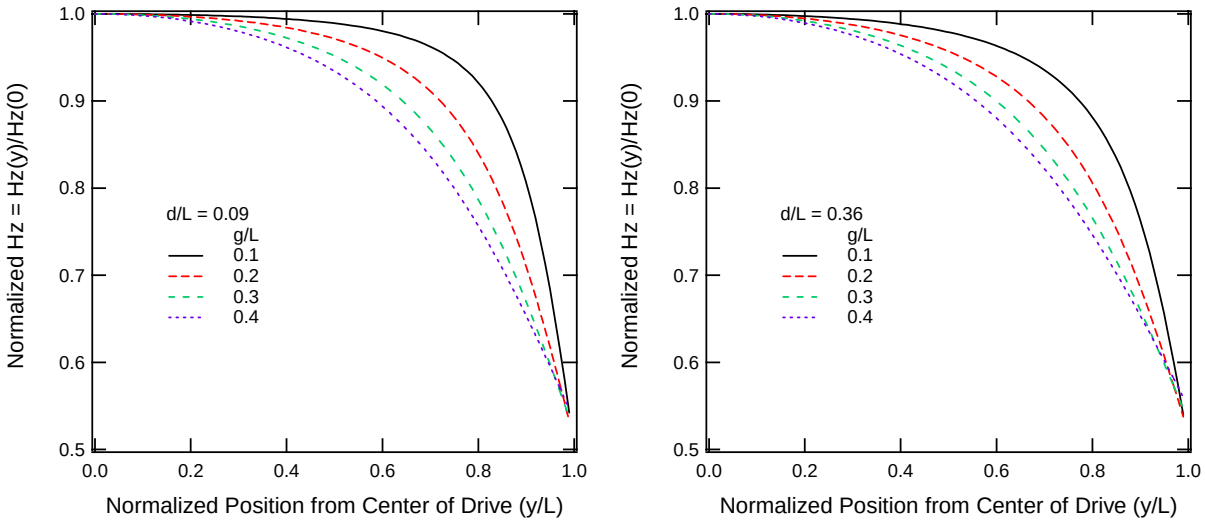

Figure 5. Field variation with position along the sense element array for (left) d/L = 0.09 and (right) d/L = 0.36.

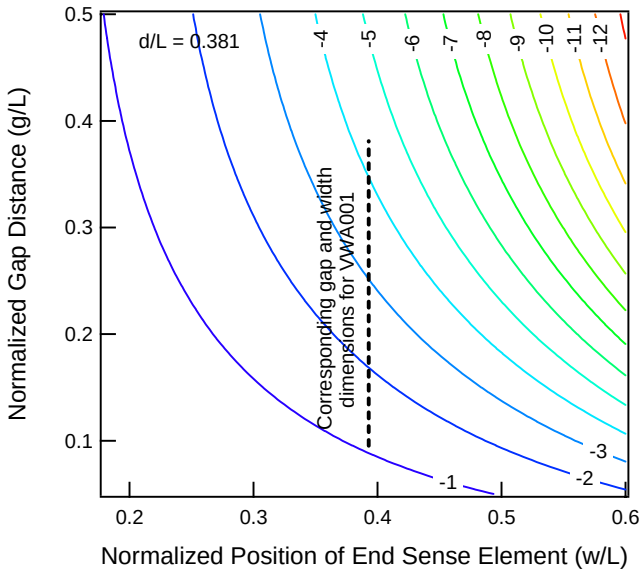

Figure 6. Percent change in field variation at the end sense element compared to a sense element at the center of the array for d/L = 0.381, which corresponds to the dimensions of the VWA001.

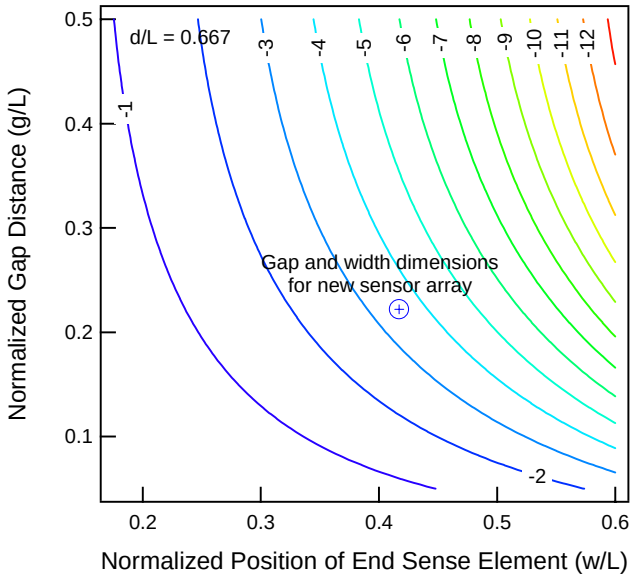

Figure 7. Percent change in field variation at the end sense element compared to a sense element at the center of the VWA003 for d/L = 0.667.

6.2 Measurement Grid Methods

MWM and MWM-Array responses are converted into material or geometric properties using measurement grids [8]. These grids convert two known values, such as the magnitude and phase (or real and imaginary parts) of the transimpedance, into the unknown properties of interest, such as electrical conductivity, magnetic permeability and lift-off. The grids are generated using a forward model and properties of the test material to create two-dimensional databases, or precomputed responses, which can be displayed graphically to support procedure development. Figure 8(left) shows a conductivity/lift-off grid and data from one channel of an MWM-Array in scans performed with four different insulating coating (shim) thicknesses. This figure illustrates how the conductivity and lift-off (representing the total thickness of the insulating layers) can be independently measured. For magnetizable steels, the magnetic

permeability is often determined, which in turn is related to the material microstructure and the residual or applied stress at a given location. If the coatings are smooth with at most a gradual thickness variation or the sensor proximity to the surface is maintained with a scanning fixture, then the lift-off provides information about the surface topology and can be used to indicate the presence of near-surface corrosion or damage. Higher-order databases are used for the determination of more than two unknown properties of interest, such as coating thickness (via sensor lift-off or proximity), metal wall thickness, and metal electrical conductivity and/or magnetic permeability. Figure 8(right) illustrates a lattice as a family of grids.

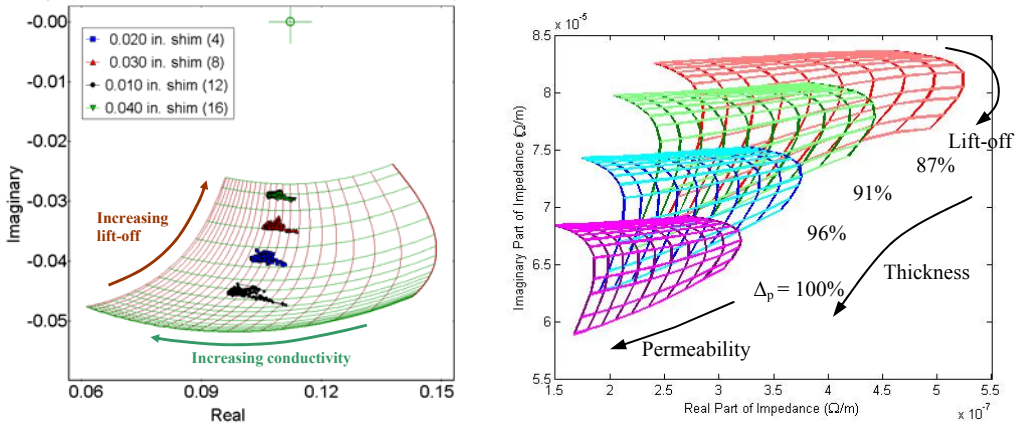

Figure 8. Representative measurement grid (left) and lattice (right) [6].

The ability to model the responses for the MWM-Arrays accurately significantly reduces calibration and scanner fixture requirements. For example, in some situations an "air calibration" can be used, permitting measurement of a component's absolute magnetic permeability or electrical conductivity without calibration reference standards. In-place recalibration and calibration verification are possible with these absolute-property sensors. Furthermore, the lift-off (proximity to the steel pipe wall surface) of each sense element is measured independently, which inherently compensates for variations in barrier coating thickness and the scanning fixture does not need to hold the sensor array at a fixed distance from the pipe wall surface.

Early in the project several types of simulations were performed in order to refine the sensor designs to accommodate the relatively thick coatings of interest for pipeline inspections. As an initial assessment of the sensitivity of the sensors, measurement lattices were generated for several situations. These lattices can be visualized as a series of measurement grids where three (or more) unknowns are to be determined. Good sensitivity is generally reflected by open grids having a large space between the grid lines. For example, Figure 9 (left) shows the simplified layer geometry for determining the properties of a weather jacket or a metallic corrosion resistant alloy. The unknowns to be determined are the sensor proximity to the jacket (lift-off) as well as the conductivity and thickness of the jacket/alloy. Representative lattices suitable for aluminum alloy weather jackets are shown in Figure 10. The sensor response varies with the excitation frequency and, by using two or more measurement frequencies, the conductivity and the thickness of the jacket can be determined.

Once the properties of the jacket have been established, low frequency measurements can be used to determine the steel pipeline condition. Figure 9 (right) shows the simplified layer geometry including the jacket and the steel pipeline. Assuming that higher frequency measurements were performed to determine the jacket conductivity and thickness as well as the lift-off, this information is then incorporated into the measurement grid lattices for determining the thickness of any insulation or air gaps, if present, and the presence of corrosion in the pipeline. Representative measurement grid lattices for the determining the relative permeability of the pipeline, the thickness of the pipeline, and the insulation

thickness are shown in Figure 11 for λ/4 = 0.5-in. and in Figure 12 for λ/4 = 5.0-in. The low frequencies, on the order of 10-100 Hz are required to see through the jacket and through the pipeline itself. These simulations indicate that the shorter spatial wavelengths will be able to see through moderate coating thickness less than approximately 1-in., but larger dimensions such as λ/4 = 5.0-in., are required for inspection through thicker insulating layers.

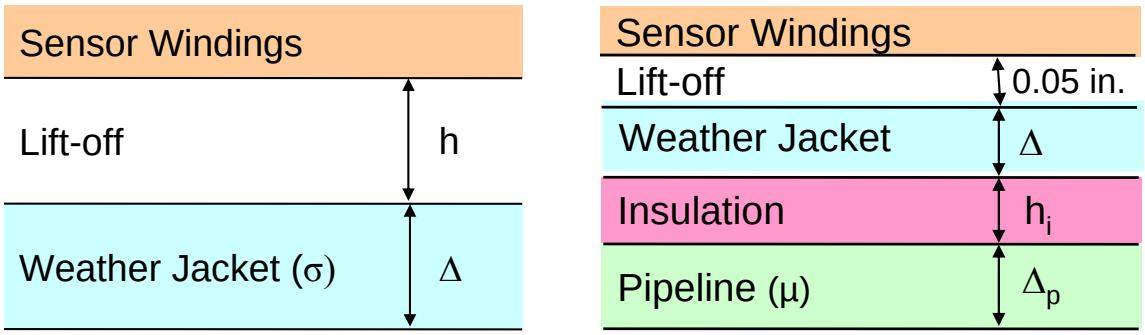

Figure 9. (Left) Simplified geometry for measurements to determine weather jacket properties. (Right) Representative layered geometry for an insulated pipeline including a weather jacket.

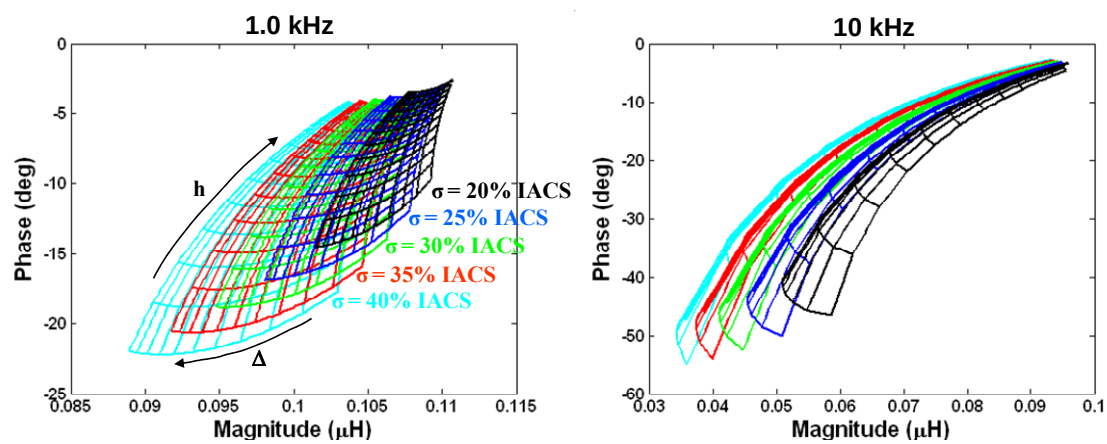

Figure 10. Conductivity/thickness/lift-off measurement grid lattices at two frequencies for λ/4= 0.13-in. and relatively high values for the electrical conductivity. The lift-off was varied from 0.01 to 0.12-in. and the Δ was varied from 0.05 to 0.15-in.

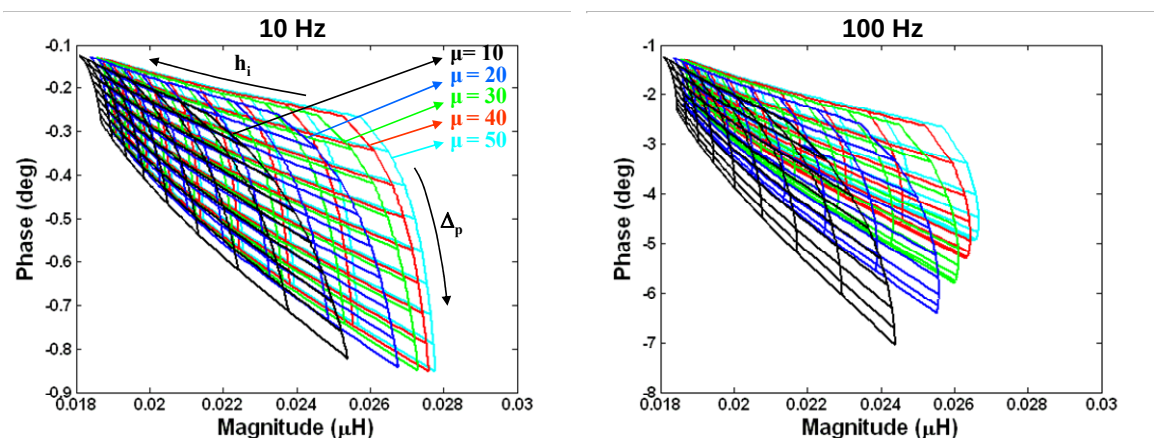

Figure 11. Pipeline-permeability/pipeline-thickness/insulation-thickness lattices for λ/4=0.5-in. The pipeline thickness Δ_p varied from 0.1 to 0.5-in. and the insulation thickness (h_i) varied from 0.2 to 1.0-in.

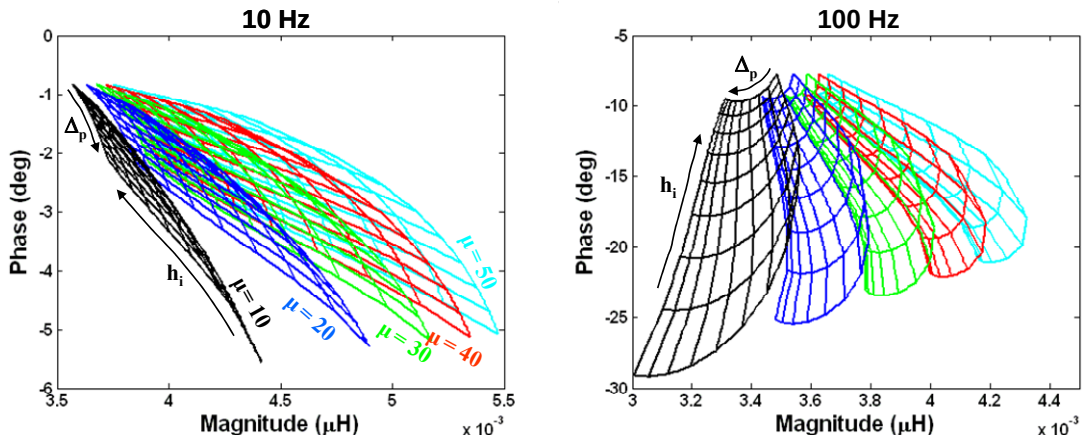

Figure 12. Pipeline-permeability/pipeline-thickness/insulation-thickness lattices for $\lambda/4$=5.0-in. The pipeline thickness Δ_p varied from 0.1 to 0.5-in. and the insulation thickness (h_i) varied from 1.0 to 5.0-in.

6.3 Scanning fixtures

Internal and external scanning fixtures were developed as part of this joint program. The external scanners were convenient for testing the effects of different sensor winding geometries and establishing the sensitivity of each sensor geometry to near-surface material loss and damage conditions for various sensor lift-offs and coating thicknesses. The internal scanners were developed to demonstrate measurement capability for MWM-Arrays examining the pipeline condition from inside the pipeline and to investigate integration requirements for placing the measurement instrumentation into an internal scanning tool.

6.3.1 External scanners

In the effort to provide field support equipment for the scanning arrays as part of the inspection program from the outside, several types of scanning fixtures were investigated. The first type of fixture is shown in Figure 13 and is suitable for use with small MWM-Arrays, such as the FA28 or FA24, for damage imaging through very thin or thin coatings. The sensor array is wrapped around a rigid plastic and foam support layer and positioned underneath the probe electronics. A position encoder is used to record the array position during a scan and, depending upon the configuration, one or more wheels are used to hold the sensor array near the test material surface. This type of scanner was used as part of the testing of the hybrid MWM-Array/MFL configurations.

A second type of fixture is shown in Figure 14. This scanner fixture has four wheels to provide stability during scans on a pipeline. A plastic sheet is used as a back support to hold the sensor in place during the scan and attaches to the scanner fixture with a rigid clamp on one side and a ratcheting clamp on the top. The sheet passes over a tensioning bar to help hold the sensor array against the pipe. A foam layer is placed between the sensor array and the plastic sheet to provide some compliance. The primary mechanism to accommodate coating thickness variations are the linear springs placed at the top of the fixture. The probe electronics fit inside the fixture and a linear position encoder is also placed at the side of the fixture. This fixture accommodates a minimum pipeline diameter of 6-in. and coating thickness of 0.5-in. to 2.0-in.

A smaller scanner for hand-held, local inspections was also fabricated. This scanner is aimed at using smaller VWA arrays, such as the VWA003, that can be held and placed against the pipeline easily. There are two configurations of interest. The first configuration is an open-faced design; a prototype is shown in Figure 15. Similar to the wrap-around design, the sensor array extends out from the side of the probe electronics and a position encoder is placed on the small fixture holding the probe electronics. The sensor

array is held in place with a foam backing. In this current embodiment, two hands are required for scanning and there can be variability in holding the sensor array against the insulation surface. However, this is a more compact inspection tool as well. The second configuration has the sensor array wrapped around a support fixture and placed underneath the probe electronics. This would make scanner easier to use with a single hand, but requires careful consideration of the effect of the material used on the back side of the sensor array; since the sensor array is designed to inspect through thick layers of insulation, without shielding, it is also sensitive to the presence of conducting and/or magnetic materials (such as the probe electronics) behind the sensor array. The first configuration was pursued since it does not have the complications associated with the shielding layer.

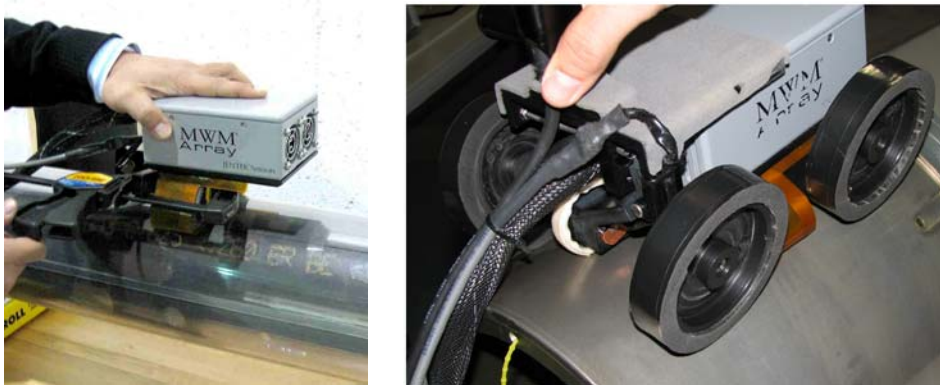

Figure 13. Photographs of a single-sided scanner for use with an FA24 and smaller MWM-Arrays.

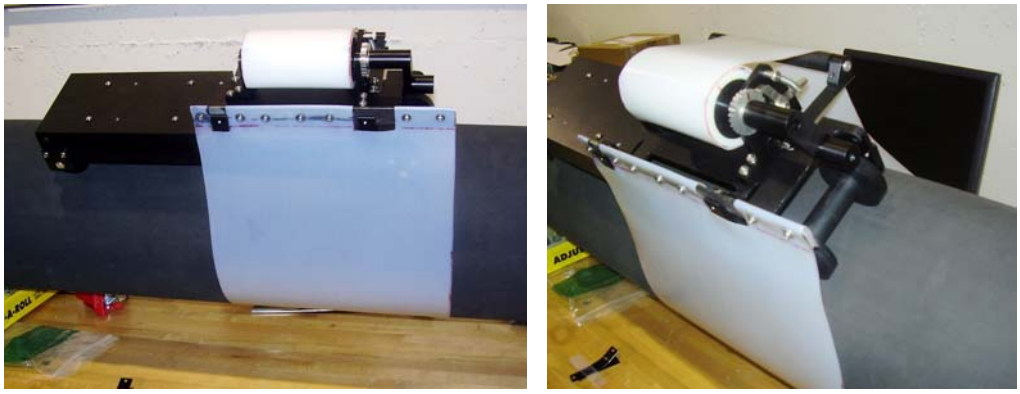

Figure 14. Photographs of the next generation wrap-around scanning fixture.

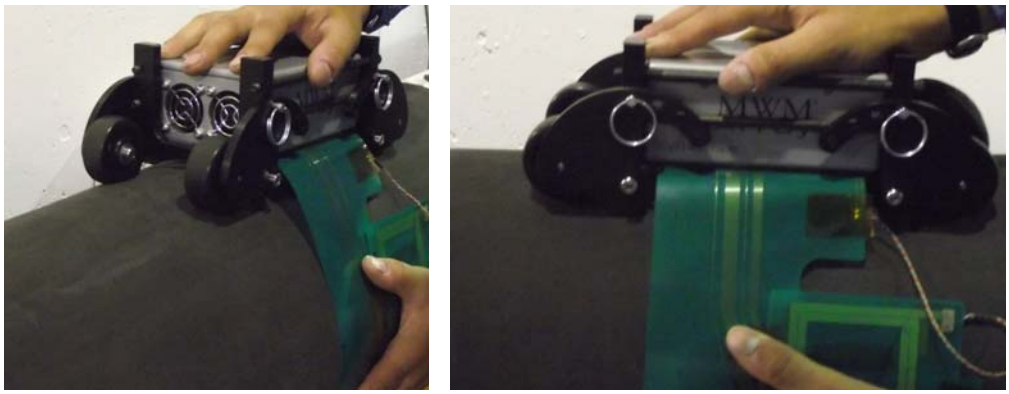

Figure 15. First generation prototype hand-held scanner.

6.3.2 Internal scanners

For performing initial internal scans of the pipe sections, an ILI tool developed in a complementary program by JENTEK for the Navy was used. This tool served as a test bed for testing instrumentation configurations and helped to provide a foundation for understanding sensor array adaptation issues. For example, issues that were investigated during these initial measurements included: 1) sensor mounting onto the tool; 2) sensor placement near the material surface during scanning; 3) measurement noise effects from long cables; and 4) imaging resolution trade-offs with scan speed. The scanner, as shown in Figure 16, is designed for scanning inside small (4-inch) diameter tubes and incorporates its own motors for translation along the pipe. In this configuration, a single MWM-Array and probe electronics are mounted onto the scanner fixture. An umbilical cable connects the probe electronics and position encoder cable to impedance measurement instrumentation located outside the pipe section. An external laptop computer is used to control data acquisition and store the acquired data.

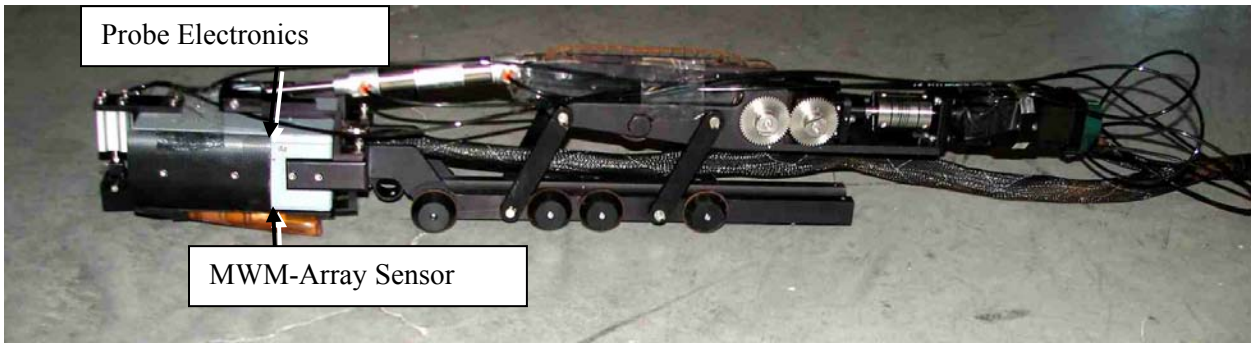

Figure 16. Photograph of the ILL tool to serve as a test platform for testing instrumentation configurations with an FA28 MWM-Array sensor and probe electronics installed.

For the first pull test, an MWM-Array was mounted into a prototype scanning fixture as shown in Figure 19. The inner cylindrical central housing held the probe electronics unit and the MWM-Array was positioned on spring-loaded arms that brought the MWM-Array support fixture into contact with the pipe wall surface. A slot in the central housing allowed a cable to run from the probe electronics unit to the MWM-Array. Rubber rings at each end kept the scanning fixture approximately centered during the scans. The flexible MWM-Array was mounted onto a rigid backing that was slightly recessed from the main body of the fixture. An optical encoder was mounted onto the same fixture that held the MWM-Array to provide position information during the scan. The nominal lift-off was 1/16th-in. between the sensor and the pipe wall. The MWM-Array and probe electronics were connected to the impedance measurement instrument through a cable that was approximately 66-ft long. After each pull, the cable was disconnected from the instrument and pulled through the pipe section, and then reattached to the instrument when the prototype scanning fixture was returned to the inlet. Two slings were attached to the tool, one to interface with the winch which pulled the tool through the pipe and one to carry the cable that was used to pull the winch cable back through the pipe at the end of each run.

Figure 17. Photographs of the prototype scanning fixture with FA24 MWM-Array.

For the second pull test, the prototype scanning fixture was modified to accommodate two MWM-Arrays and the impedance measurement instrumentation, with data acquisition computer, were integrated into the tool itself. This modified prototype tool was intended to demonstrate that the instrumentation could be integrated into an ILI tool form factor and could successfully operated multiple arrays. Figure 18 shows a photograph of this second generation tool. Figure 2 shows the integration of the impedance instrument into the ILI demonstration tool. This instrumentation was identical to JENTEK's 8000-series instrumentation. The layout was changed to fit within the envelope of the ILI tool. Only a power supply cable was required for this configuration. Ongoing work is aimed at incorporating a power supply within the tool itself so that the tool can provide stand-alone operation.

For this tool, two VWA005 sensors were mounted on the sensor carriage and twisted pair ribbon cables carried the signals to the probe electronics unit. In the standard instrumentation, a 2 meter cable connects the probe electronics unit to the 8000-series instrument. This cable was removed and the probe was connected directly to the impedance measurement electronics. The single board computer was a Microsoft Windows based processor that ran the full GridStation software to perform the data processing and visualization.

Some items remain from the 8000-series instrument that are not needed for an ILI tool. The probe was housed in the same box as it is when it is a stand-alone unit separate from the instrument. This is necessary because the mounting of the probe electronics was not as adaptable as some of the other electronics boards. As a result, this unit occupies more space than is necessary. The connectors (see Figure 2) are also not required, but have been retained because the interface that they provide was not easily modified. These could be eliminated in an integrated design. The final item is the multifunction board (Figure 2, below the connectors). Only a small portion of this board that contains the drive circuitry is needed for the ILI tool and this circuitry could be transferred to another location in an integrated tool.

Not shown in Figure 2 is the position encoder wheel. For the pull tests, an encoder was mounted on an arm on the rear of the tool. The encoder wheel rides against the pipe wall and the position was read by a magnetic encoder. Magnetic encoders can be sealed against the environment more easily than other technologies while providing high resolution (0.001-in. for this demonstration). The encoders used during this test are sealed to IP68, which means that it is protected from dust and can be submerged in water. This technology is appropriate for ILI applications with minor redesign of the housing and cabling to ensure protection against pipeline pressures.

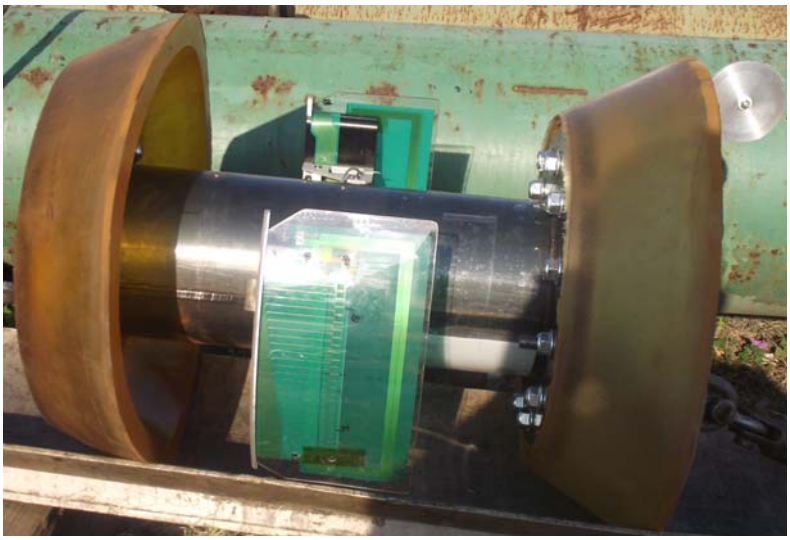

Figure 18. JENTEK's second generation prototype ILI tool. The 8000-series instrumentation is housed inside the cylindrical chamber. Two VWA005 MWM-Array sensors are mounted on either side of the tool. Only a power line tether was used during the trials.

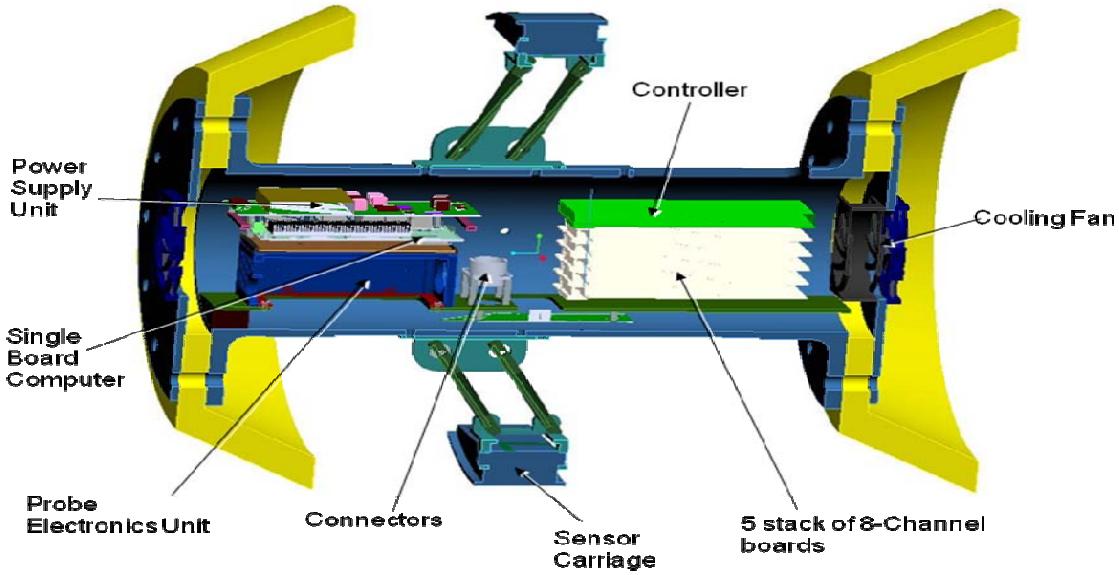

Figure 19. Schematic of JENTEK's 8000-series instrumentation integrated into the ILI demonstration tool. The layouts of the electronic components were altered to fit within the cylindrical envelope of the ILI tool.

6.4 Demonstration Results

6.4.1 Near-Surface Corrosion Imaging (External)

High frequency measurements were performed on a variety of samples. For near-surface damage inspections with insulating barrier coatings, high frequency magnetic fields readily penetrate the coating and respond to the condition of the underlying steel pipe wall. Initial and baseline measurements were performed on flat steel plates as new sensor arrays became available. This was followed by laboratory testing on a pipe section with several external machined areas of material loss for a range of coating thicknesses. These demonstrated the capability to inspect near-surface material loss and the results directly relate to the ability to measure internal material loss from the inside of the pipeline.

6.4.1.1 Initial measurements on flat plates

Numerous measurements were performed on flat plates having machined areas of material loss. These measurements demonstrated the basic capability of the MWM-Arrays and measurement grid methods to independently measure the material condition (magnetic relative permeability of the steel) and lift-off (sense element proximity to the steel surface). These measurements also helped to establish the accuracy of the models for each sensor and contributed to procedure refinements to improve the material loss estimates.

The plates were machined from 4340 steel and had dimensions of 12-in. by 12-in. by 0.125-in. In several of these plates, five regions were machined on one side of the plate to represent areas of material loss. The dimensions of these regions are listed in Table 2. Figure 20 shows a photograph of the machined steel plates. By stacking the plates, with and without machined flaw regions and with different sides closest to the sensor array, variety of flaw configurations and thicker materials could be simulated.

Table 2. List of flaw dimensions for the flat plate specimen and corresponding sense element channels.

Flaw Number	Length (in.)	Width (in.)	Depth (in.)	Channel (through flaw center)
1	1.0	0.5	0.050	35
2	2.0	0.5	0.075	28
3	3.0	1.0	0.100	20
4	2.0	0.5	0.050	12
5	1.0	0.5	0.025	3

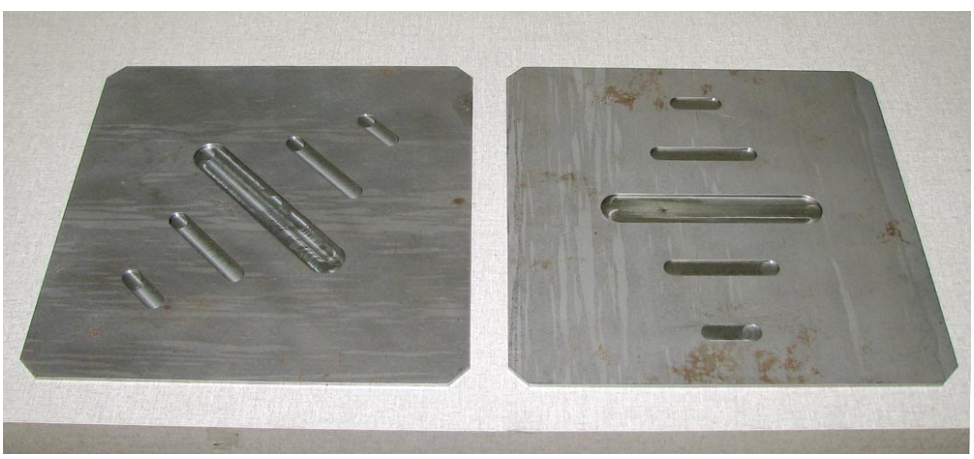

Figure 20. Photograph of flat machined steel plates for simulated corrosion loss.

Baseline demonstration measurements for simulated material loss were performed using JENTEK's medium-size FA122 MWM-Array sensor and a machined steel plate. Figure 21(left) shows the FA122 on a steel plate. The FA122 has a linear array of sense elements and a drive winding microfabricated onto a flexible insulating substrate. This array has thirty-seven 6.35 mm (0.25-in.) square sense elements and a scan width of approximately 9.25 in. A linear position encoder attached to the probe electronics provides the array position during the scan. Figure 21(right) shows a flat plate scanning fixture for the FA122, along with the impedance measurement instrumentation and laptop computer running JENTEK's GridStation software environment for data acquisition and analysis. This fixture provides a rigid support that helps maintain the position of the array relative to the probe electronics and position encoder. A foam layer behind the sensor array helps the sensor array conform to the surface of the material being examined.

Figure 21. (Left) Photograph of the medium-sized FA122 and a machined steel plate. (Right) Photograph of the instrument and FA122 MWM-Array mounted to a scanning fixture. Note that the FA122 is underneath the plastic scanner fixture.

Measurements were performed with several different thicknesses of insulating shims and paper to simulate coating or insulation thicknesses up to 12.7 mm (0.500-in.). A second plate was placed behind the machined plate so that the total steel thickness was 6.35 mm (0.25-in.) in the unflawed areas. Figure 22 shows a series of lift-off images as the simulated coating thickness is varied for a high frequency excitation of 631 kHz. The color scale was adjusted in each image to highlight the presence of the flaw regions. The larger flaws are apparent even for the larger coating thicknesses, but the smaller flaw regions approach the background signal variation for thicker coatings. This suggests that the sensitivity of a given sensor to a given flaw size (area and depth) will decrease as the coating thickness increases; however selection of other sensor designs, as described below, can offer improved sensitivity for thicker coating layers. The color variations at the sides of the images are edge effects as the sensor array moves over the edges of the steel plate. These effects are more pronounced for the higher coating thicknesses as the sensor magnetic fields responds to a large area.

Note that the left and bottom scales of the images of Figure 22 are expressed in inches while the scale on the right of the images indicates the sensor element channel number. In this case the sensor array was calibrated using a measurement in air and a measurement with a shunt sensor in which the sense elements are shorted. This is a robust method of calibration since it does not rely on knowledge of a reference material, but it requires having a shunt that is essentially identical to the sensor array. The striping in the images for the larger coating thicknesses is associated with a poor calibration for channel 22. The image quality generally improves for larger samples, where edge effects are not present.

Figure 23 shows the 631 kHz measurement grid and data used for the multivariate inverse methods. The grid lines reflect the nonlinear sensor response variation with magnetic permeability (μ) and sensor lift-off (h) for an infinite half-space of material. The measurement grids inherently account for the

nonlinearity in the sensor response. In this case, an electrical conductivity of 3.75% IACS was assumed for the grid and which is typical for steel. Also plotted on the grid are data points for channel 7, which is between the two lower machined sections on the sample, for measurement points when the sensor array is over the steel plate (data points 300-600). These data points essentially follow a line of constant permeability as the lift-off or coating thickness is varied, which validates the models used for the sensor array.

Figure 24 shows B-scan plots across each of the flaws indicated in the scan images. Table 2 lists both the flaw dimensions as well as the sense element channel number corresponding to each flaw. Distant from the flaws, the change in lift-off reflects the different coating thicknesses and some channel-to-channel variability, which increases with coating thickness. However, in each case, the lift-off increases, often substantially, over the machined areas, which is consistent with these being areas of near-surface material loss.

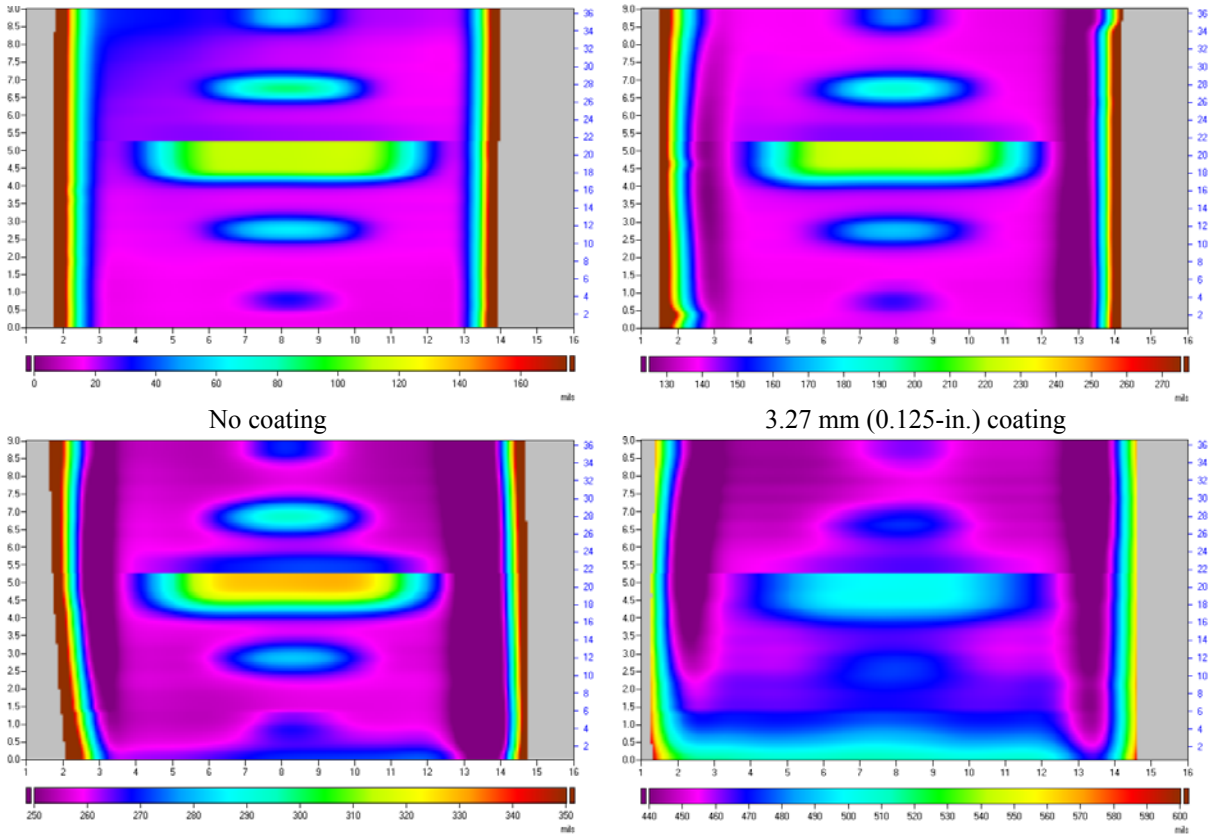

Figure 22. Images obtained from a series of scans with the FA122 over the machined steel plate and with different simulation coating thicknesses.

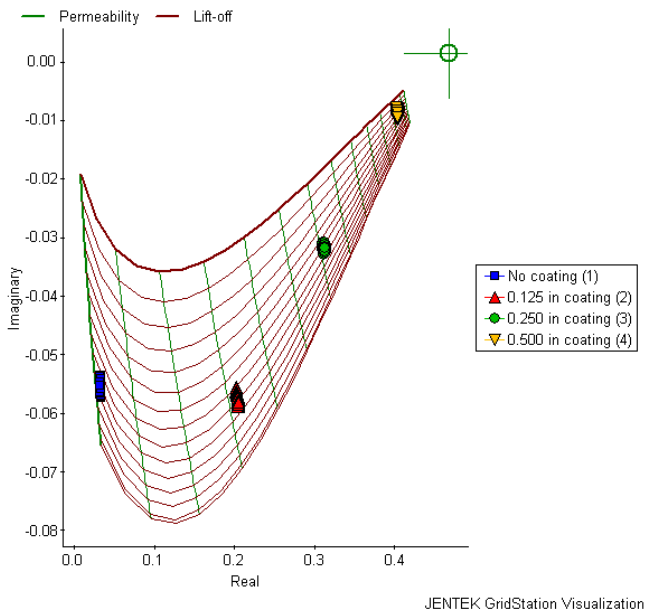

Figure 23. Measurement grid and data for an FA122 channel over the machined steel plate (from channel 7, which is between the machined regions) for several varied coating thicknesses.

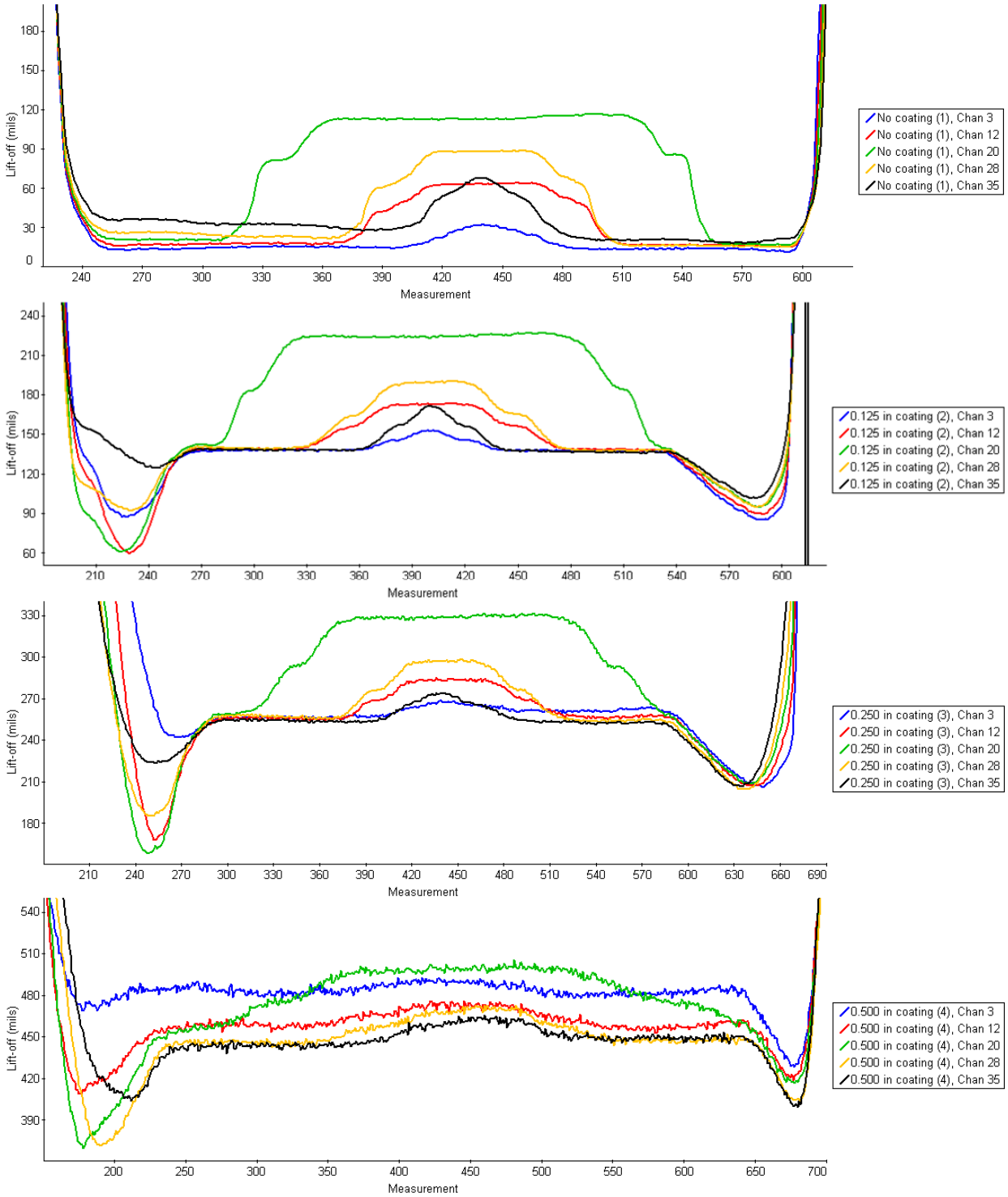

Figure 24. B-scans for comparing the FA122 responses for no coating and several insulating layer thicknesses to emulate varied coating thicknesses.

To illustrate the baseline performance of this sensor, Figure 25 shows plots of the nominal coating thickness (left) and depth of the material loss regions (right) as the coating thickness is varied. For the nominal coating thickness, there is a slight lift-off of approximately 0.010 to 0.015 inches for the small coating thicknesses due to the geometry of the sensor and the presence of protective layers placed on the sensor surface. For large coating thicknesses, there is a slight underestimate of the coating thickness; this estimate could be improved by selecting a better value for the electrical conductivity of the steel or by using multiple frequency measurements to determine the electrical conductivity simultaneously with the permeability and lift-off. Figure 25(left) also shows a plot of the measured distance obtained with a sensor model assuming a periodic geometry, which leads to a substantial underestimate of the coating thickness. This indicates the value of using the correct model in the data inversion as it makes the measurements more reliable.

For the depths of the material loss regions shown Figure 25(right), the measured values tend to underestimate the depth because the geometry of the material loss is not considered in the basic measurement grids; the basic measurement grids assumed planar material layers. This suggests that a procedure for improving the estimates of the material loss would include (1) detecting regions of material loss and roughly determining its spatial extent and (2) using a flaw-based measurement grid that incorporates this spatial information and measurement response information to obtain the depth estimate.

As a simple example of such as measurement procedure, consider the hybrid measurement grids of Figure 26, which relate the actual flaw depth to the effective lift-off change that would be expected from a planar material layer model. These responses were obtained from a three-dimensional boundary element model for the FA122 geometry assuming a steel substrate with long flaws that were 0.5 or 1.0 inches wide. The response of a sense element over the center of the flaw is indicated. As expected, the effective lift-off tends to underestimate the actual flaw depth, which the underestimate being more significant at larger coating thicknesses. However, compensation for the coating thickness and flaw geometry is accomplished by passing the measured effective lift-off and coating thickness through the hybrid measurement grids to obtain corrected material loss measurements. The result of this process, shown in Figure 27, indicates that this type of correction yields reasonable material loss values.

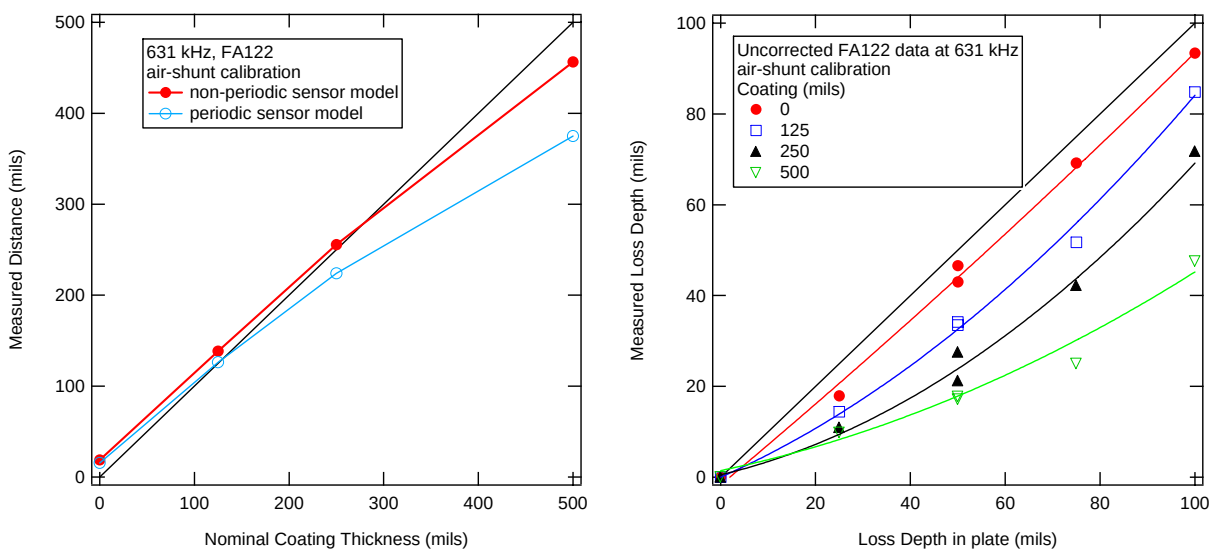

Figure 25. (Left) Nominal coating thickness measured with the FA122 at locations distant from the machined flaw regions. (Right) Nominal depth for each of the machined flaw regions using a uniform layer model that did not correct for the area of the flaw.

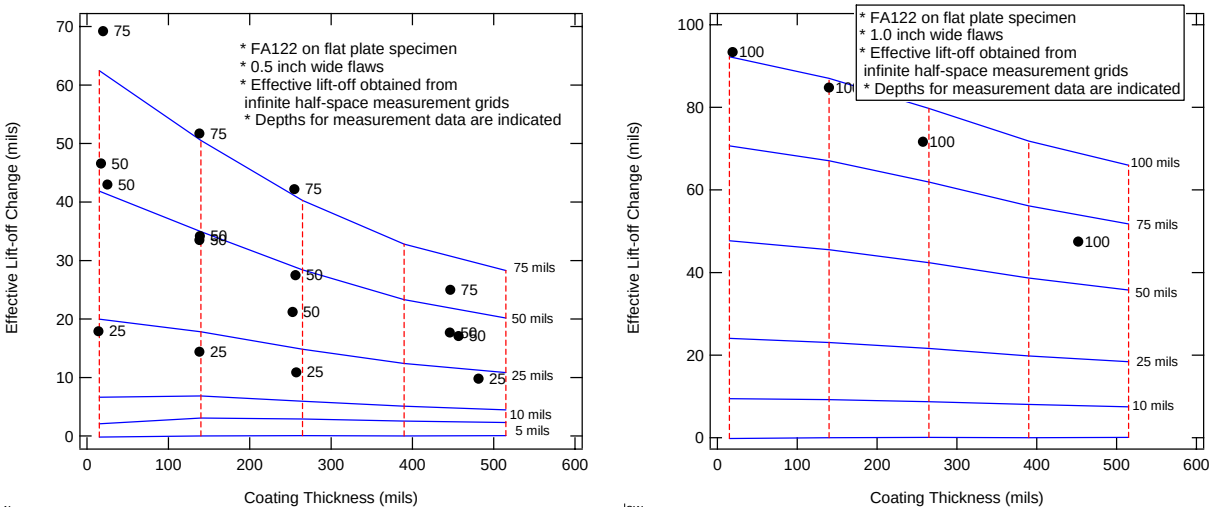

Figure 26. Hybrid measurement grids relating the flaw depth and coating thickness to the effective lift-off change obtained from a planar model. (Left): For 0.5-in. wide flaws. (Right): For 1.0-in. wide flaws.

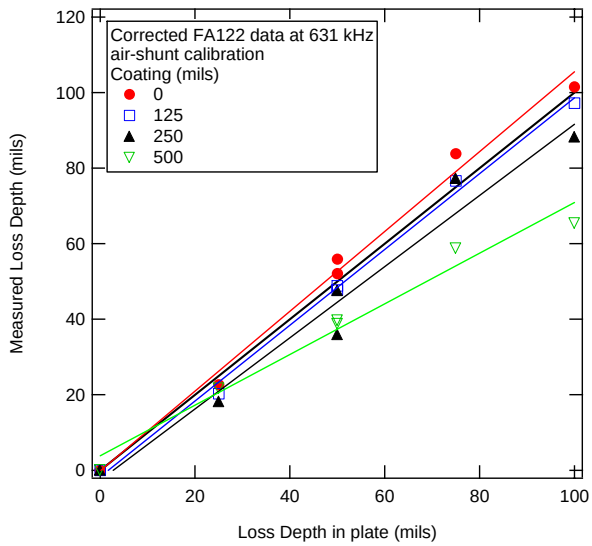

Figure 27. Plot of the depth for each of the machined flaw regions using the hybrid measurement grids of Figure 26.

6.4.1.2 Measurements on laboratory pipe sections

Numerous laboratory measurements were performed on a steel pipe section. This pipe section was 4 ft long, with an outer diameter of 6.625-in. and a wall thickness of 0.28-in. A series of flaws were machined into the outside surface to represent external material loss. This pipe section had four rows of flaws located every 90° around the circumference of the pipe. The flaws were machined to depths corresponding to 5%, 10%, 25%, and 50% material loss. The nominal flaw sizes are 0.25, 0.5, 1.0 and 2.0 inches in diameter, but the curvature of the surface and the shallow flaw depth resulted in a rectangular shape for the shallower and larger flaws. The flaws are positioned near the center of the pipe in order to provide some room for moving a sensor array and scanning fixture along the pipe. These depths were chosen since they are appropriate for repair/replace maintenance decisions for pipelines.

Figure 28 shows a photograph of this pipe section along with a small-size FA24. This pipe section is loaded on top of rollers; this allows the section to be rotated so that additional scans could be made and an image of the surface topology spanning the circumference of the pipe section can be obtained. Two

layers of 0.010-in. thick plastic sheets were wrapped around the pipe section to simulate the presence of a thin (0.020-in. thick) insulating coating. During the measurements, the sensor array was moved along the top surface of the pipe section. For these measurements, an air-shunt calibration was performed. This type of calibration uses a measurement in air and a measurement with a shunt sensor in which the sense elements are shorted. This is a robust method of calibration since it does not rely on knowledge of a reference material, but it requires having a shunt that is essentially identical to the sensor array. The frequencies used were 10, 100, and 631 kHz.

Figure 29 shows property images obtained for the FA24 MWM-Array at a frequency of 100 kHz. The left and bottom axes are expressed in inches. The regions of material loss are clearly visible as areas of increased lift-off as the effective distance between the sensor array and the steel surface increases. The shapes of the regions are also appropriate; for the shallower and larger flaws the regions are rectangular in shape. The flaw regions are also apparent in the relative permeability image. Since the magnetic permeability can vary with material condition, such as residual stress, this may reflect property changes associated with the flaw machining process. Note that a scan was made over each of the four rows of material loss; scans were not made over the intermediate regions that did not contain flaws. Figure 30 shows B-scan (individual sense element response) plots of the lift-off response for a sense element that passed over the center of each region. The lift-off varies with material loss as expected. These plots show that each of the material loss regions is detected.

Figure 28. (Left) Photograph of an FA24 MWM-Array being scanned over a pipe section with a thin coating. (Right) Photograph of the pipe section with machine loss and on a test table.

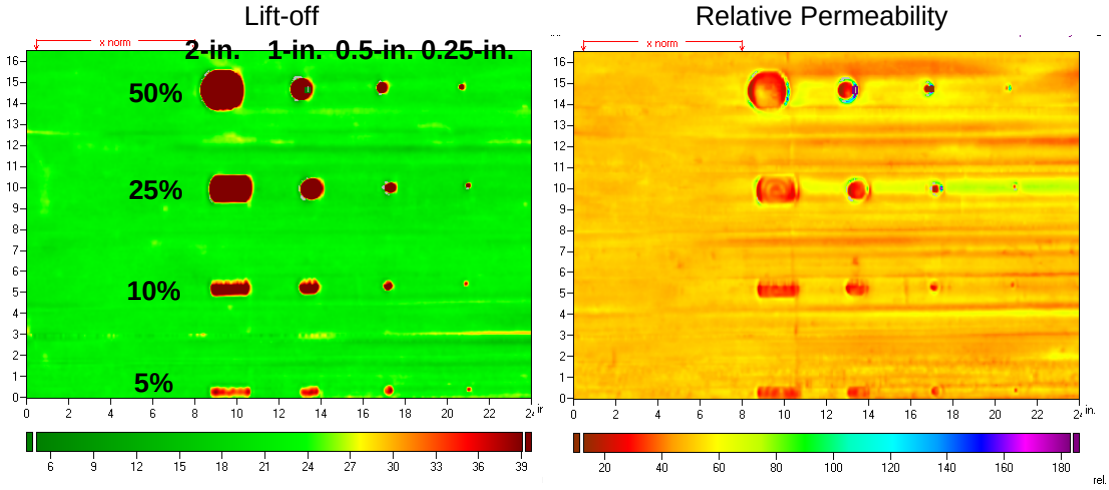

Figure 29. C-scan lift-off (left) and permeability (right) images obtained from a series of scans with an FA24 MWM-Array at 100 kHz for the pipe section having flaws machined in the outside surface and a thin (0.020-in.) plastic coating.

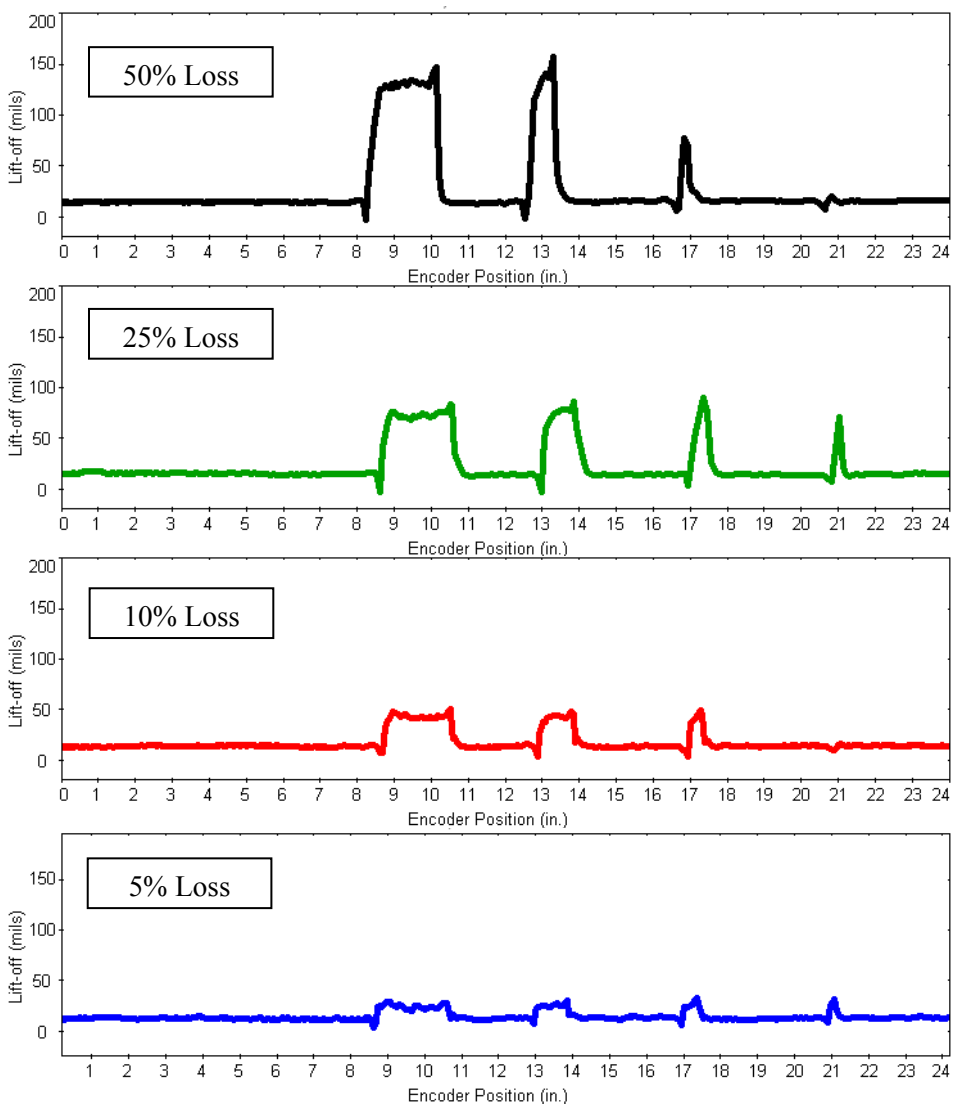

Figure 30. B-scan lift-off plots for an FA24 sense element with a 0.020-in. thick coating.

Similar measurements were performed with the larger VWA001 sensor array scanned over the external pipe section. For the measurements with the VWA001, a 0.5-in. thick layer of Neoprene was wrapped around the surface to represent a medium thickness coating. Figure 31 shows the pipe section with Neoprene and the scanning fixture with the sensor array in place. For these measurements a 1-inch gap was used between the linear array of sense elements and the drive winding. The scanner fixture has a linear position encoder at the front and two support wheels in the back. The plastic sheet is used to hold the sensor in place during the scan and attaches to the scanner fixture on each side. This sheet replaces the foam and rigid backing used for flat-plate measurements and provides some flexibility for scanning pipelines having different sizes.

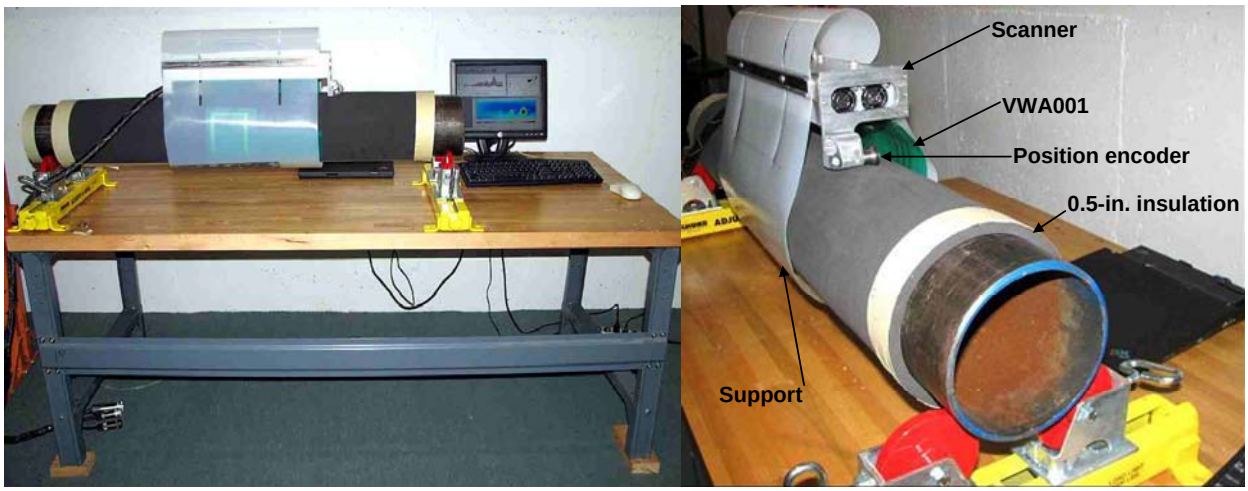

Figure 31. Photographs of the external material loss steel pipe section wrapped with a 0.5-in. layer of Neoprene along with the scanning fixture for the larger sensor arrays. The plastic sheet is attached to both sides of the scanner and holds the VWA001 in place around the pipe section during the scan.

Figure 32 shows lift-off data obtained with the VWA001 over a 0.5-in. coating. Many of the machined areas are visible in this image with the larger diameter and deeper flaws appearing most clearly. This image was created from several scans at different circumferential positions over the surface. The fixture does not appear to hold all of the sense elements in contact with the coating surface and there are background variations in the lift-off associated with how the scanner fixture holds the array in position. Improving the fixture will enhance the imaging capability of the sensor arrays. The B-scan plot can also be used to determine the presence of damage. For example, while the 0.5-in. material loss region is difficult to see in the C-scan image, there is a local increase in lift-off for the sense element channels that went over the flaw.

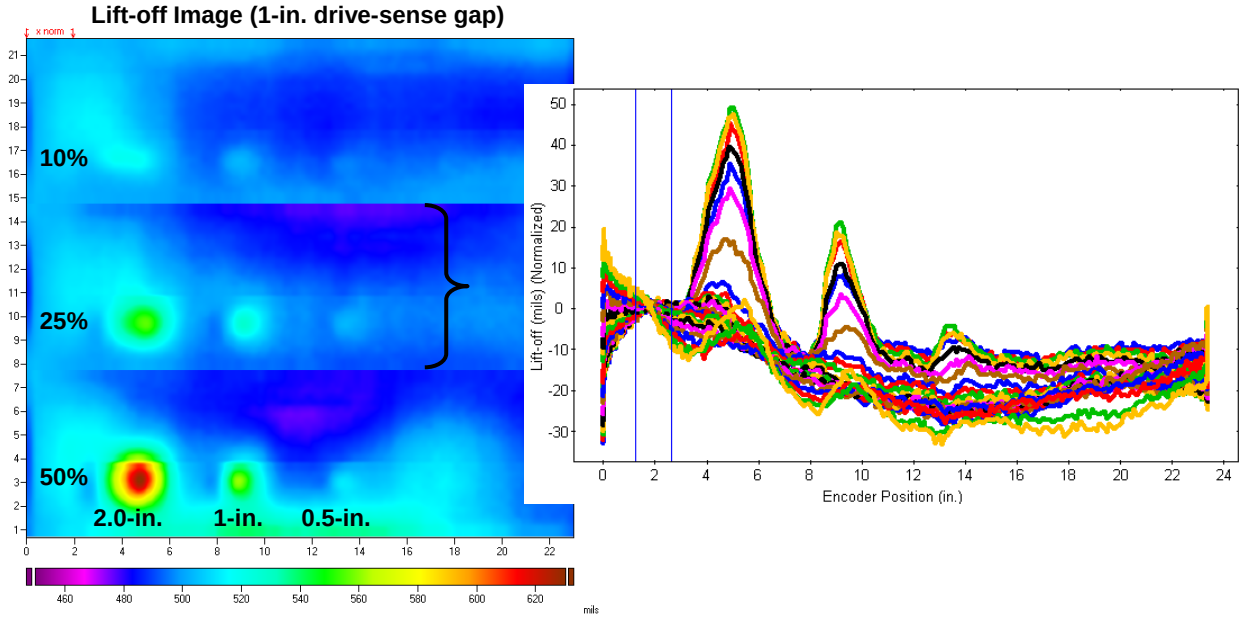

Figure 32. C-scan lift-off image obtained from a scan with the VWA001 at 631 kHz over the 50% material loss flaws for the external material loss pipe section and a 0.5-in. layer of Neoprene.

A series of measurements were performed to determine the sensitivity to different operating condition parameters. These parameters include the excitation frequency, drive-sense gap spacing, the type of

calibration performed, the use of extra signal amplification, and the use of different probe electronics, as well as the different coating thicknesses. Figure 33 shows a series of lift-off images obtained with the VWA001 and a drive-sense gap of 25.4 mm (1.0-in.) for a range of coating thicknesses. The images show the 25% and 50% material loss regions, with the high spatial resolution images obtained for coating thicknesses of 0.5 and 1.0-in. For larger coating thicknesses the larger flaws are still visible but there is a noticeable degradation of the flaw images. For the 1.75-in. thick coating the sensor array only passed over the 50% material loss regions. Here, two types of calibrations were performed. An air-shunt calibration was performed for the 0.5 and 1.0-in. coating thicknesses since the sense element impedance change between the air value and the proximity of the steel pipe was large compared to the measurement noise. However, for the larger coating thicknesses, a reference calibration was performed where reference measurements were performed on the coated pipe with and without a 0.10-in. shim. This lift-off change led to a shift in the sense element impedance that was distinct from the measurement noise and provided a better alignment of the sensor response with the measurement grids. Although the air-shunt calibration is preferred, since it requires fewer assumptions about the steel and coating properties, the reference calibration is useful when the inspection requires measurements of small impedance changes.

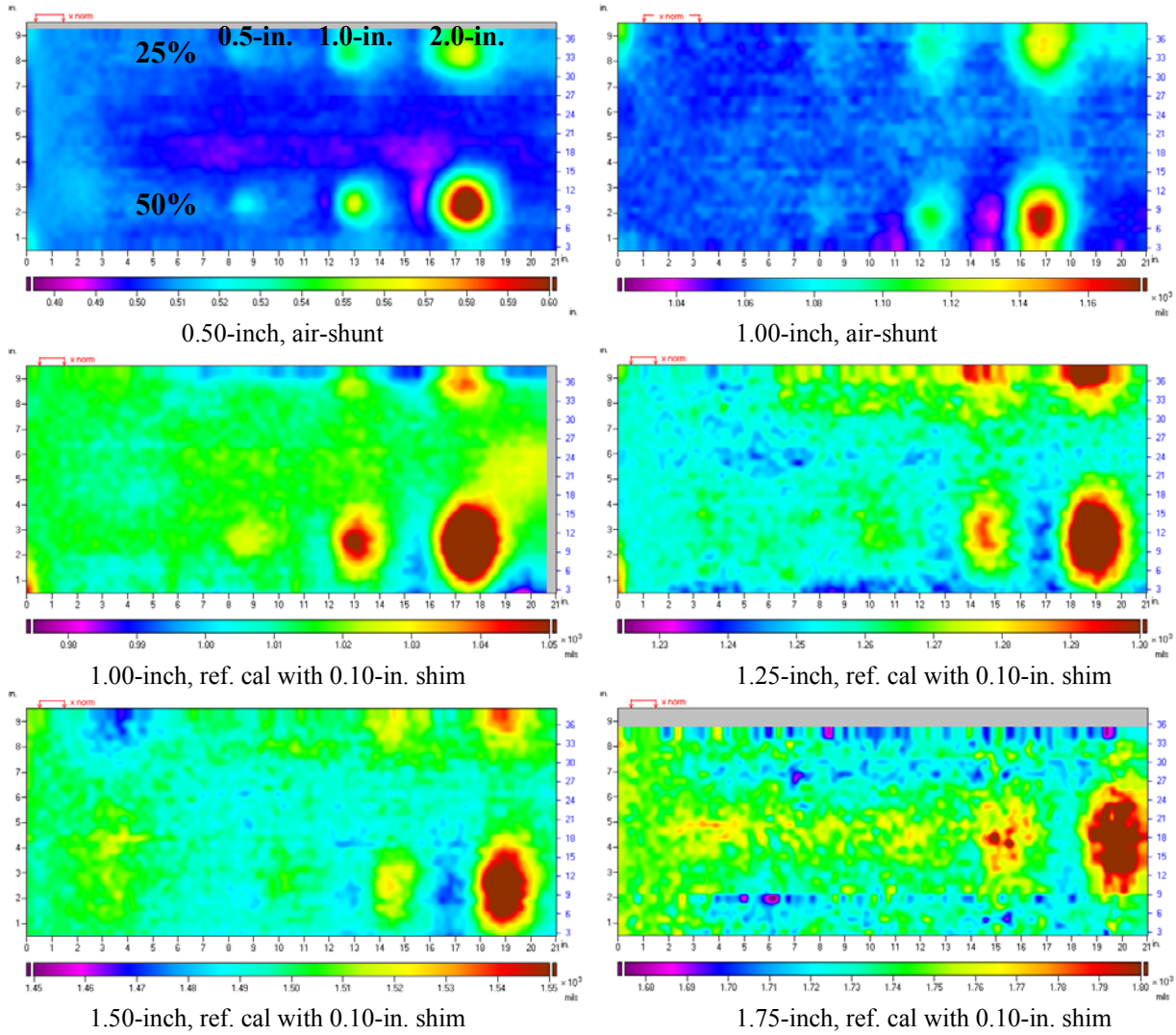

Figure 33. Effective lift-off images for the steel pipe with manufactured material loss regions using a VWA001 with a 25.4 mm (1.0-in.) drive-sense gap and a frequency of 100 kHz.

Figure 34 contains plots of the effective lift-off change associated with a single sense element that passed over the centers of the 50% material loss regions. This lift-off change is taken as the difference between the lift-off at each location and an average lift-off obtained for an unflawed region at the beginning of the scan. An 11 point moving average was applied and the peak in the response for the 2-in. diameter flaw at 100 kHz was used to align the measurement scans. The 12.7 mm (0.5-in.) coating data used an air-shunt calibration while the other measurement used a reference calibration. For the moderate thickness coatings (0.5 and 1.0-in. thick), all three material loss regions are visible at the higher frequencies (100 and 631 kHz), but only the two larger loss regions are visible at the lower frequency of 10 kHz. Also there is a visible decrease in the measurement noise (for example, for the 44.5 mm (1.75-in.) thick coating) as the frequency increases. This suggests that the near-surface material loss measurement through insulating coatings should use a relatively high frequency.

Although each of these regions has the same maximum depth of 3.56 mm (0.14-in.), the change in the effective lift-off depends upon the size of the flaw region. Since the peak value for the material loss does not change appreciably with the coating thickness, it appears that the size of the flaw region has a more significant effect than the coating thickness on the measurement response. Models and measurement grids that account for the size of the flaw region can improve the depth estimate. The measured response to each flaw region reflects a combination (or convolution) of the sensor dimensions as well as the flaw dimensions. The width of the material loss is approximately the response width at half the maximum value.

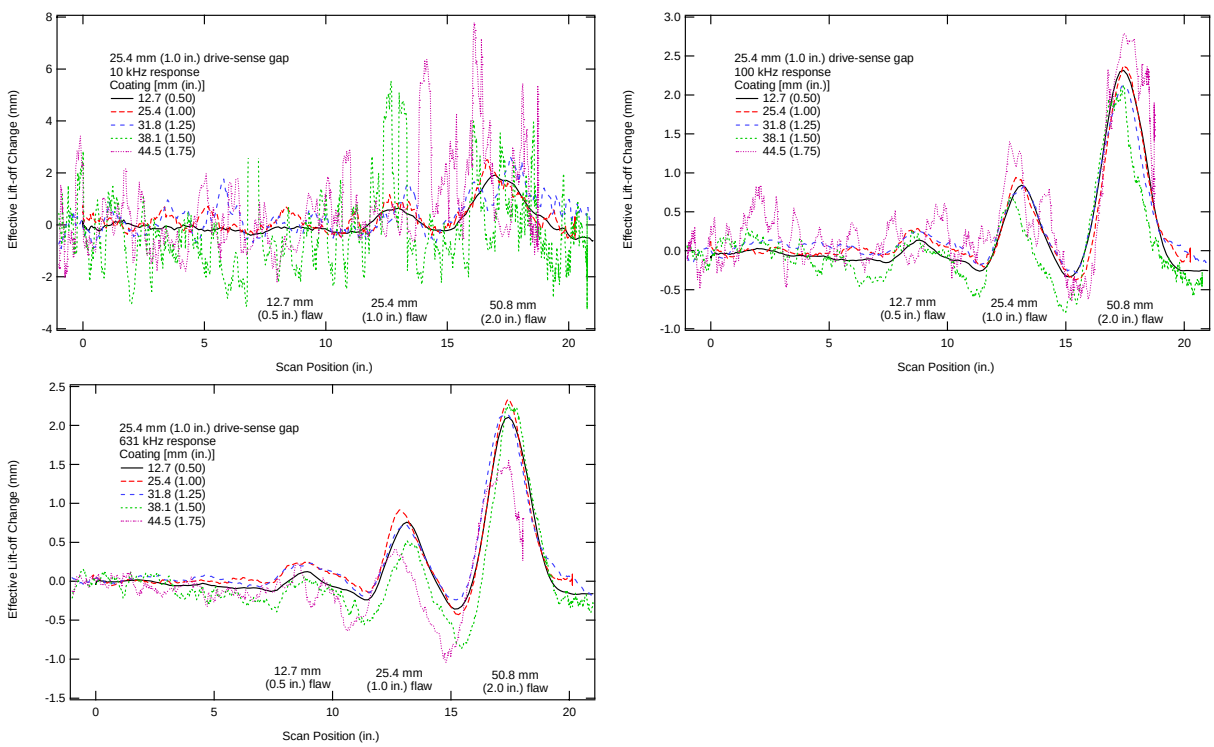

Figure 34. Effective lift-off change plots for the 50% material loss regions for a VWA001 with a 25.4 mm (1.0-in.) drive-sense gap as the coating thickness is varied.

In order to reduce the size of the array to make it easier to use during an inspection, configurations with the sense elements placed inside the drive winding loop were investigated. This brought the sense elements closer to the return segment of the drive winding so that the sense elements respond to both the near drive winding segment as well as the return segment. By making the distance to the return segment comparable to the distance to the near segment, the net magnetic field in the vicinity of the sense elements

is larger. However, this also required passing the sense element connector leads over the drive winding connections; copper tape was used as a shielding material over most of these leads to minimize this stray coupling. In the following, the copper shielding was used for the VWA001 but not the VWA003.

Measurements were performed with both the VWA001 and the VWA003 arrays with a gap distance between the sense elements and the near drive segment 12.7 mm (0.5-in.). These measurements were taken on a flat steel plate with various insulation coating thicknesses. Figure 35 shows results for a single channel of the VWA001 at 10 kHz and 100 kHz. The data follow a line of constant magnetic permeability as the lift-off increases. Although the grids still collapse at high lift-offs (coating thicknesses) near the air point, the grid itself is better behaved than in Figure 35 and does not wrap around on itself. This indicates a decreased sensitivity to measurement noise. Similar results are observed with the VWA003 as shown in Figure 36.

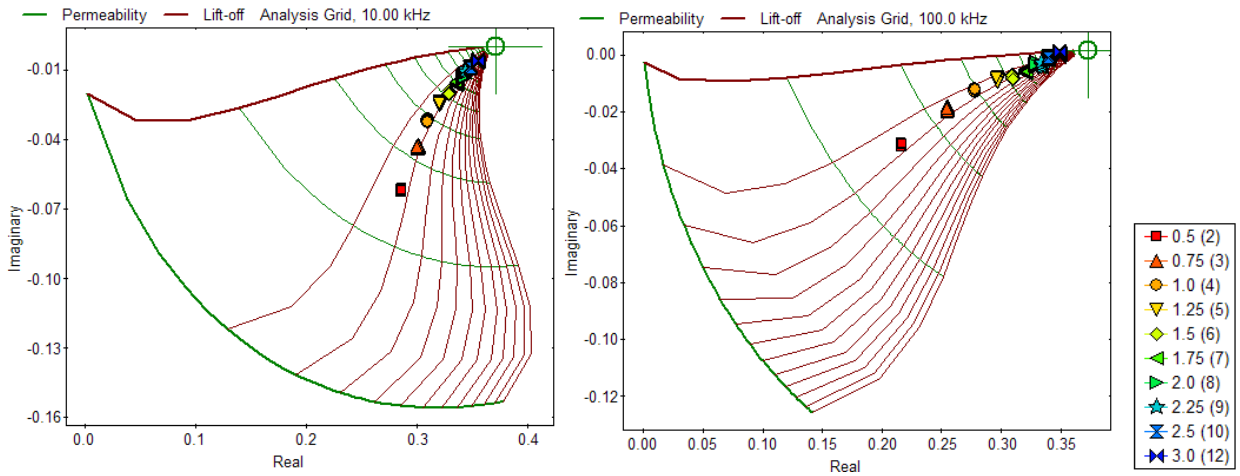

*Figure 35. Results for a VWA001 sense element array **inside** the drive winding, a HF probe, and a 12.7 mm (0.5-in.) drive-sense gap. The frequency was (left) 10 kHz and (right) 100 kHz.*

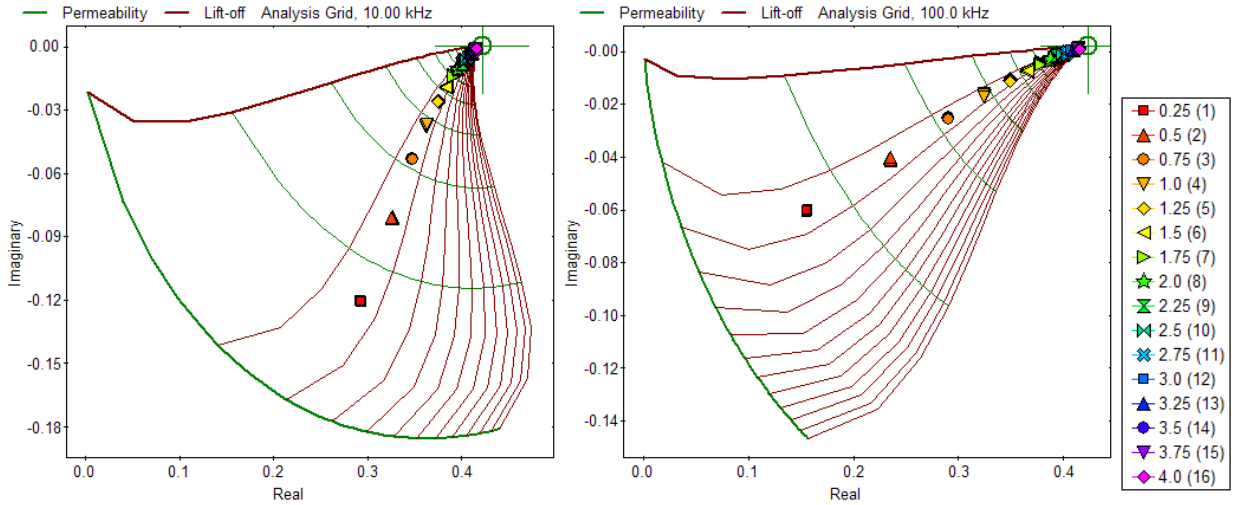

*Figure 36. Results for a VWA003 sense element array **inside** the drive winding, a HF probe, and a 12.7 mm (0.5-in.) drive-sense gap. The frequency was (left) 10 kHz and (right) 100 kHz.*

Figure 37 shows the estimated properties obtained with the sense elements inside the drive windings. For the VWA001, measurements were taken up to a coating thickness of 75 mm (3.0-in.) but for the VWA003 measurements were taken for coatings up to 100 mm (4.0-in.) thick. In both cases, the lift-off

provides a reasonable estimate of the coating thickness and the permeability values are reasonable. Note that both of these measurements used an air calibration and better results (e.g., better lift-off correlation with coating thickness and a more constant relative permeability) can be expected with a reference calibration**. This is the first demonstration that shows that these eddy-current sensor arrays are sensitive to the steel properties through 100 mm (4 in.) of insulation.** With the added benefit of requiring a smaller sensor footprint, on-going tests are evaluating this configuration for measurements on pipe sections. This approach can also be used with the low frequency sensor array to improve sensitivity to far-surface material loss with inspecting through the pipeline wall.

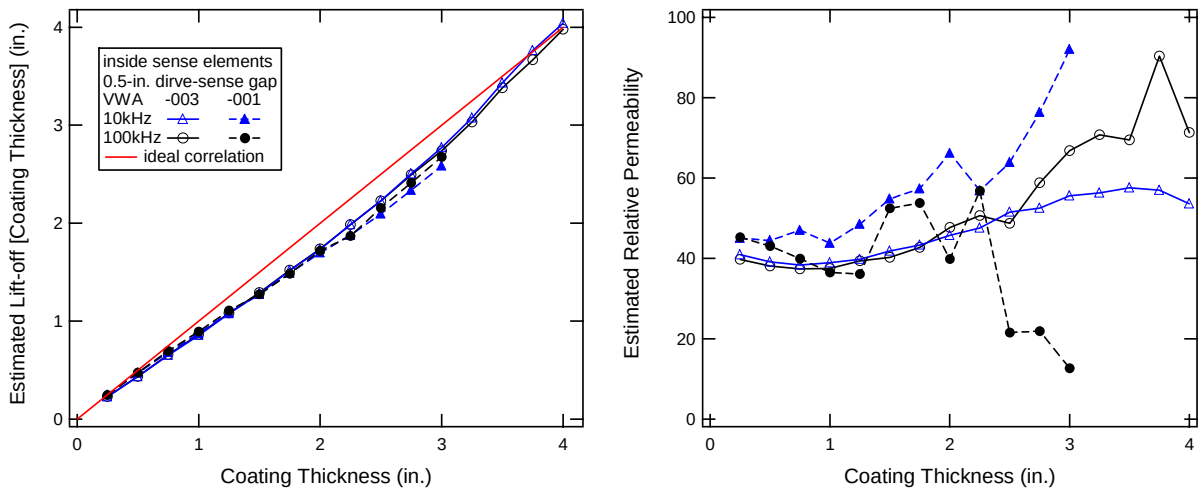

*Figure 37. Estimated properties for both the VWA001 and VWA003 with the sense elements **inside** the drive windings for a 12.7 mm (0.5-in.) drive-sense gap and a flat steel plate.*

Several measurements were also performed with the scanning fixture of Figure 14 and the VWA001. The sense element array was positioned inside the drive winding with a 12.7 mm (0.5-in.) spacing between the near drive segment and the sense elements. An air-shunt calibration was performed and low frequency probe electronics were also used. The nominal coating thickness was 12.7 mm (0.5-in.), but in some cases an extra 3.18 mm (0.125-in.) layer of Neoprene was placed underneath the nominal coating in order to test the capability of the scanning fixture to accommodate coating thickness variations. The data was processed using refined permeability/lift-off measurement grids assuming an electrical conductivity of 3.75 %IACS for the steel.

Figure 38 shows the results of an axial scan over flaws having a depth corresponding to a 50% material loss. The 50.8 mm (2.0-in.) and 25.4 mm (1.0-in.) diameter flaws are clearly visible in both the lift-off and permeability images at 100 kHz. Similar results were obtained at 10 kHz. The 12.7 mm (0.5-in.) diameter flaw is visible in the lift-off image but not the permeability image; the color scale can be readjusted and B-scan plots can be used to highlight the presence of this smaller flaw. This baseline scan demonstrates that reasonable flaw images can be obtained on curved pipeline materials through coatings with the sense element array moved inside the drive winding. The estimated lift-off is slightly smaller than the actual coating thickness, which is consistent with the flat plate results of Figure 37. Better agreement is expected with improved sense element designs that have longer lead connections so that the lead shielding layers are farther from the drive winding.

Figure 39 shows the same type of axial scan except a 280 mm (11-in.) wide inner layer of 3.18 mm (0.125-in.) thick Neoprene is placed underneath the 12.7 mm (0.5-in.) thick Neoprene outer layer. The sensor array was also scanned in the opposite direction compared to Figure 38. The presence of the inner layer is visible in the lift-off images between approximate axial positions of 3.5 and 14.5 inches. Since

the Neoprene is relatively stiff, the outer layer does not conform to edges of the inner layer. Consequently, the edge of the inner layer is not very sharp in the images and there appear to be air gaps between the outer layer and steel wall that extend substantially away from the inner layer. Similar results were obtained for the 25% material loss regions with coating thickness variations. The material loss regions are clearly visible in the property images. This confirms that the spring and tensioning portions of the scanner are adequately accommodating the coating thickness changes.

Figure 40 shows the result of increasing the spacing between the drive and sense elements to 19.1 mm (0.75-in.). This figure shows images from axial scans over the (a) 25% and (b) 50% material loss regions through a 25.4 (1.0-in.) thick Neoprene coating. In this case a two-point reference part calibration was used. Both the 50.8 mm (2.0-in.) and the 25.4 mm (1.0-in.) diameter flaws are visible in both the lift-off images for the two regions of material loss. The reference calibration improves the accuracy with respect to the measurement of the absolute coating thickness and reduces element-to-element noise in the images. However, increasing the spacing does not appreciably affect the local signal change associated with the material loss, which is consistent with earlier work that showed a reduction in effective lift-off associated with flaw regions having a diameter (size) that is small or comparable to the coating layer thickness. Comparisons of axial scans over the 50% material loss regions for both drive-sense spacings are shown in Figure 41 for a 25.4 mm (1.0-in.) coating. The images of the flaw regions tend to have a higher spatial resolution for the smaller spacing of 12.7 mm (0.5-in.). **This shows that the MWM-Arrays can image through typical coating and liner thicknesses for pipelines.**

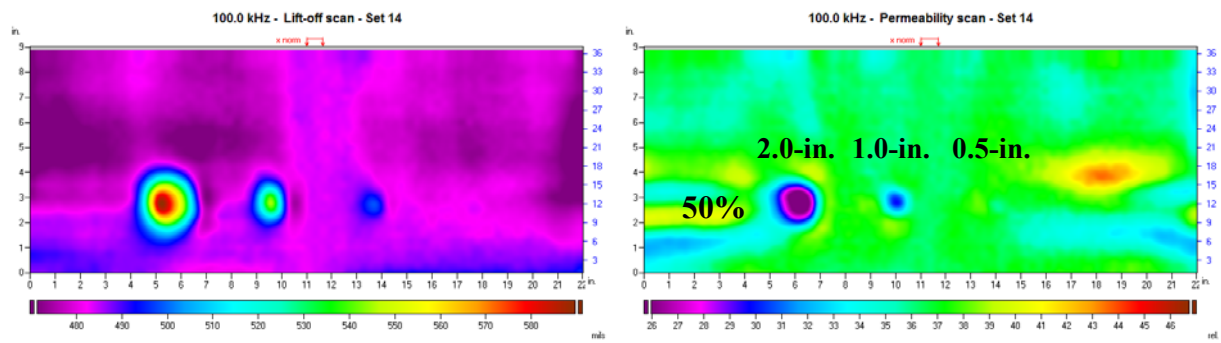

*Figure 38. Axial scans over the 50% loss regions and a 12.7 mm (0.5-in.) coating using a VWA001 with the sense element array placed **inside** the drive and with a spacing of 12.7 mm (0.5-in.).*

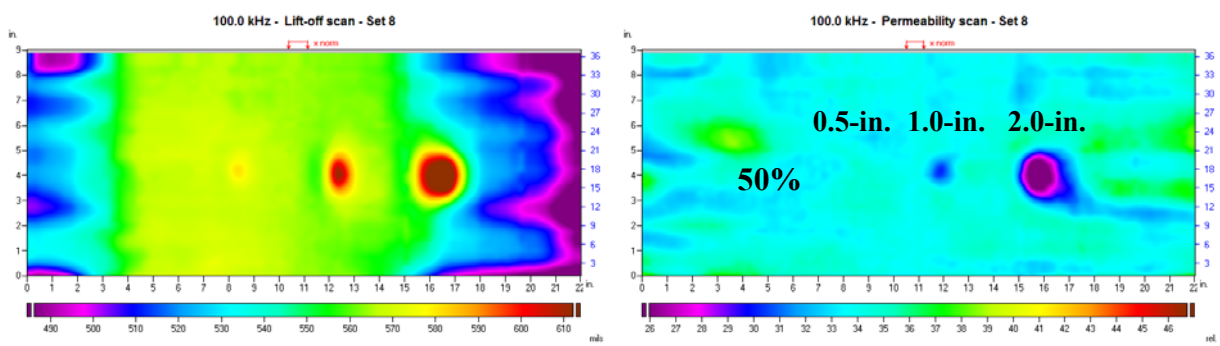

*Figure 39. Axial scans over the 50% loss regions and a 12.7 mm (0.5-in.) coating using a VWA001 with the sense element array placed **inside** the drive and with a spacing of 12.7 mm (0.5-in.). An extra layer of 3.18 mm (0.125-in.) thick insulation was placed under the coating*

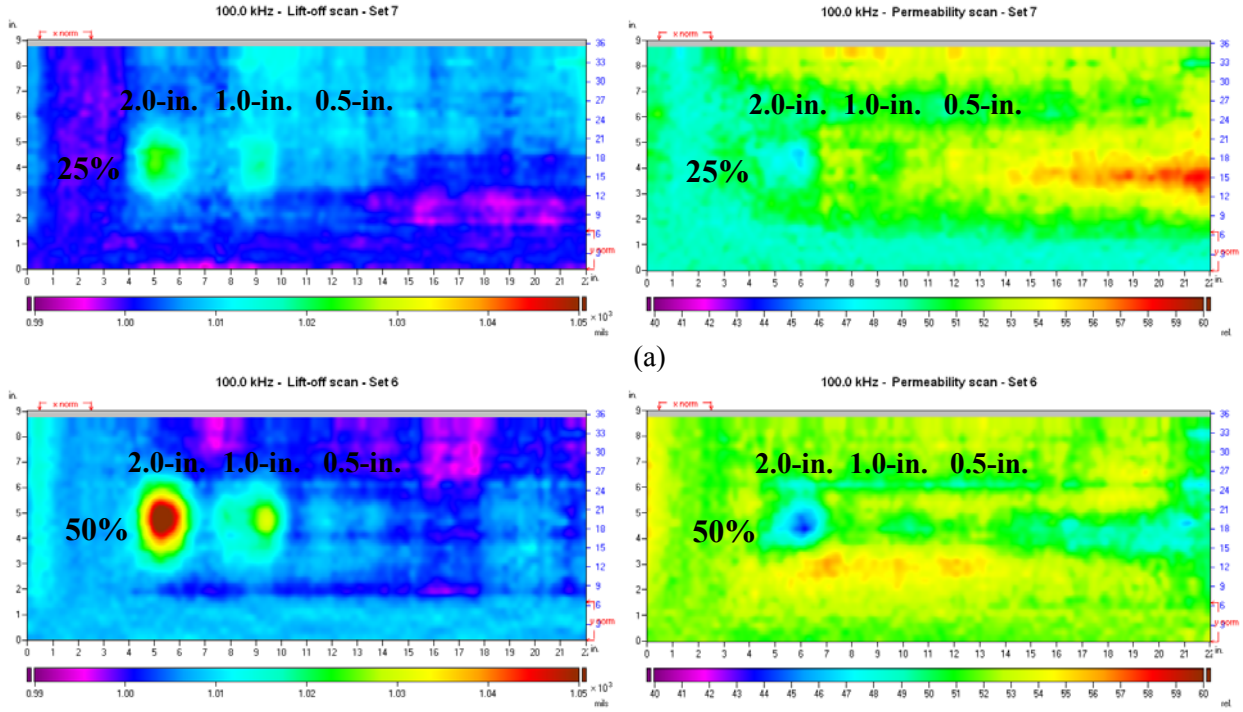

*Figure 40. Axial scans over the (a) 25% and (b) 50% material loss regions and through a 25.4 mm (1.0-in.) Neoprene outer layer using a VWA001 with the sense element array placed **inside** the drive and with a spacing of 19.1 mm (0.75-in.) A two-point reference part calibration was performed.*

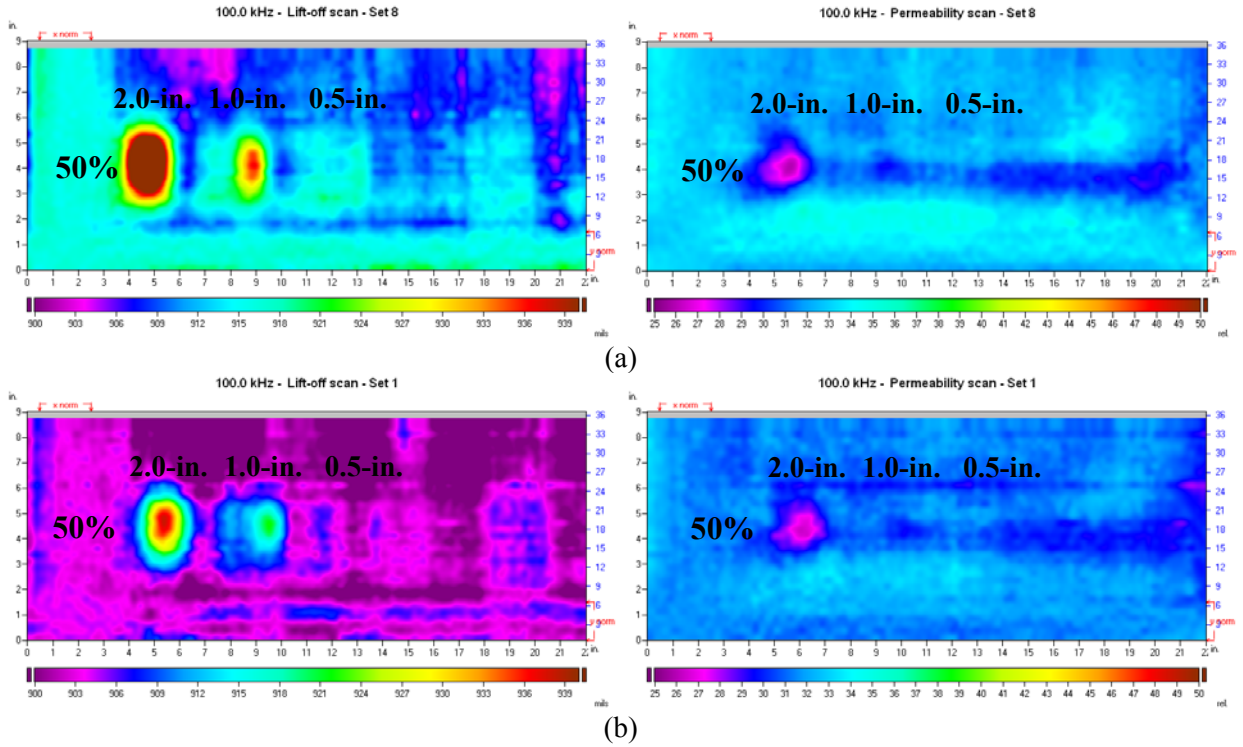

*Figure 41. Axial scans over the 50% material loss regions and a 25.4 mm (1.0-in.) Neoprene outer layer using a VWA001 with the sense element array placed **inside** the drive and with a (a) spacing of 12.7 mm (0.5-in.) and (b) 19.1 mm (0.75-in.). An air calibration was performed.*

Similar measurements were performed with the VWA003 and the hand-held scanning fixture (Figure 15). Figure 42 shows a representative set of property images obtained for the 50% material loss regions and high frequency probe electronics. Three material loss regions are visible in both the lift-off and the permeability images at 10 kHz and in the lift-off image at 100 kHz. These measurements demonstrate the capability for using the smaller scanner to image damage, albeit with a narrower scan width as compared to the VWA001.

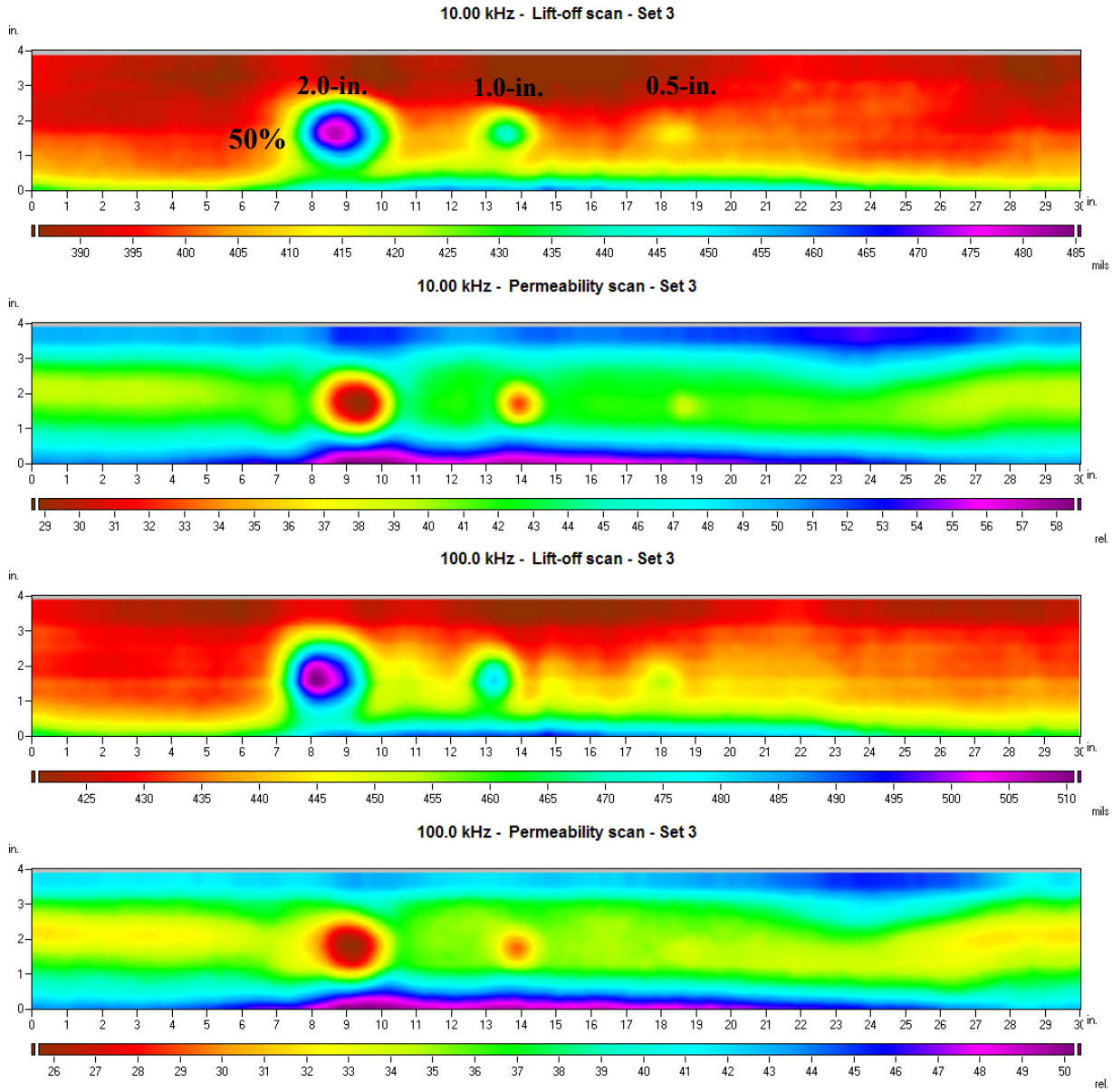

*Figure 42. Axial scans over the 50% loss regions and a 12.7 mm (0.5-in.) coating using a VWA003 with the sense element array placed **inside** the drive and with a spacing of 12.7 mm (0.5-in.).*

Figure 43 shows the lift-off images from high frequency (631 kHz) axial scans at different positions around the circumference of the pipe section using the VWA003. Through this moderate thickness coating of 6.35 mm (0.25-in.), all of the flaws that are 12.7 mm (0.5-in.) in diameter and larger are clearly visible, even for a 5% material loss. The 6.35 mm (0.25-in.) diameter flaw is visible for 25% and 50% material loss. **This shows that the larger MWM-Arrays can also be used to inspect through**

relatively thin layers of insulation and to provide a reasonable spatial resolution of the damage. This supports the external inspection project as well as the project for inspection from the inside as this type of array may be used to provide complete circumferential coverage of the internal surface while accommodating realistic stand-off distances.

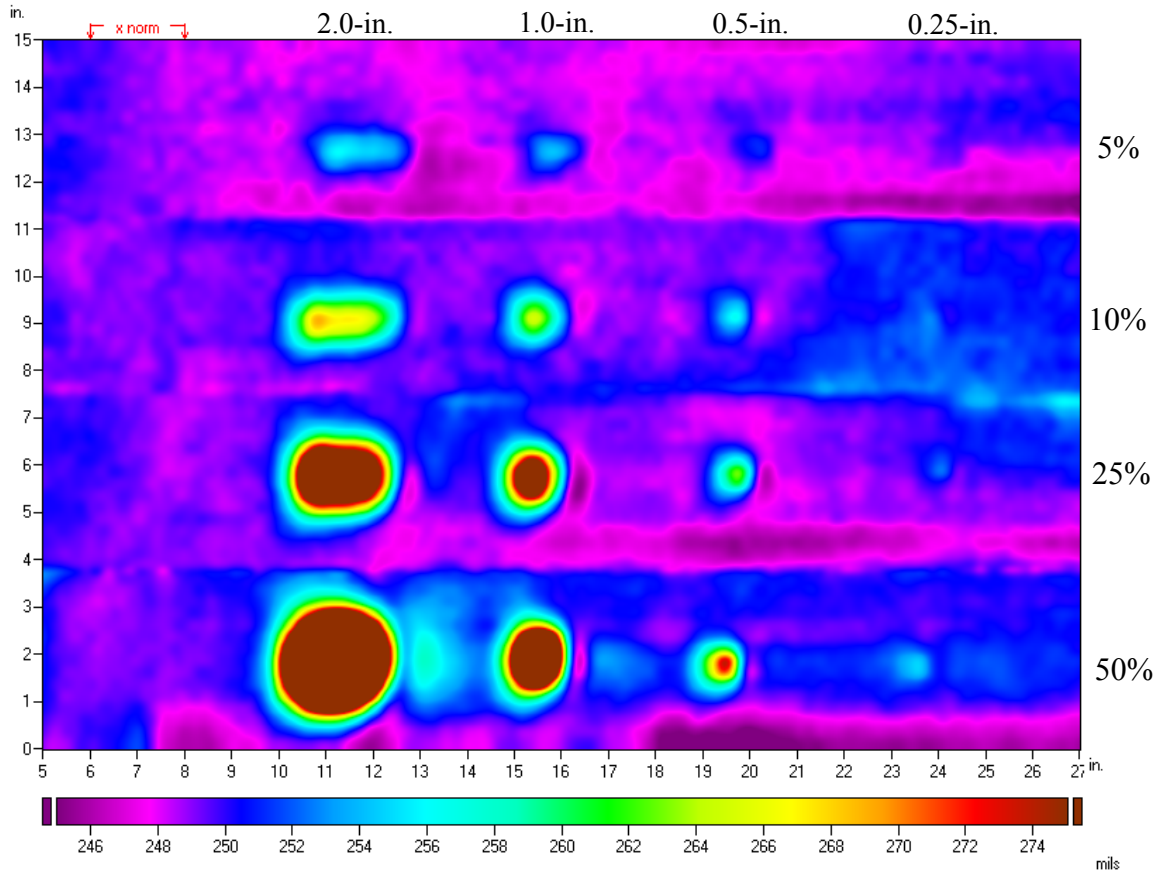

Figure 43. Axial scans over the 5%, 10%, 25% and 50% material loss regions through a 6.35 mm (0.25-in.) Neoprene outer layer using a VWA003 with the sense element array placed inside the drive and with a spacing of 12.7 mm (0.5-in.) A two-point reference part calibration was performed.

6.4.1.3 Measurements on a pipe section removed from service

Several FA24 scans were performed over a region on the inside surface of a 16-in. diameter pipeline section that exhibited actual corrosion damage within a steel pipeline. The surface was relatively rough and includes several regions of significant material loss. In these measurements, an air-shunt calibration was performed and a position encoder was attached to the probe electronics to allow spatial mapping to be performed. Two 0.010-in Mylar shim were attached on to the sensor with double-sided tape (each 0.003-in) and two pieces of 0.010-in plastic were placed on the surface of the pipeline section. Figure 44 and Figure 45 show that the material loss and pitting from the corrosion generally appear as a change in both the lift-off and permeability. These results are consistent with the measurements on the laboratory pipe section that has machined areas of material loss.

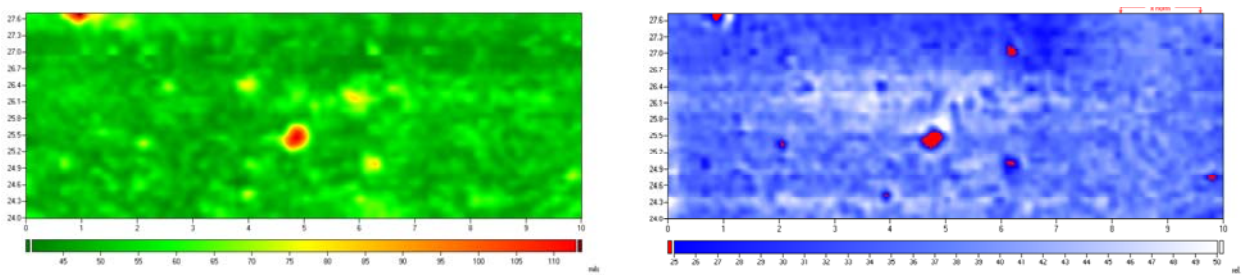

Figure 44. Lift-off (left) and permeability (right) scan images of material loss on the inside surface of the pipeline section through a 0.046-in. coating using an FA24 MWM-Array.

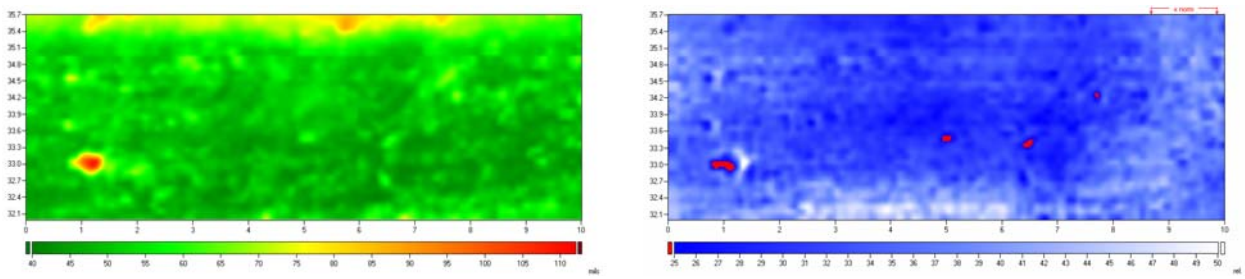

Figure 45. Lift-off (left) and permeability (right) scan images of material loss on the inside surface of the pipeline section through a 0.046-in. coating using an FA24 MWM-Array.

6.4.1.4 Measurements on risers

Measurements were also performed on 40 ft long, 6.-in. diameter riser sections made available by Chevron and PRCI (Pipeline Research Council International). Figure 46(left) shows five sections containing embedded defects. The schedule 80 steel pipe are coated over approximately 30 ft with 0.5-in. thick "Splashtron" neoprene coating. This coating includes a cloth wrap and is relatively hard since it was vulcanized at elevated temperatures. Each of these pipeline sections contains a mixture of girth welds and embedded flaws of various sizes and orientations. After creating the damage area, the corrosion products were embedded in the flaw region prior to coating. This should have made these samples representative of actual corrosion under coatings.

Figure 46. (Left) Simulated pipeline riser sections with embedded corrosion defects. (Center) Photograph of a prototype external scanner. (Right) Photograph of one of the defects.

For these measurements, the prototype external scanner fixture of Figure 46(center) was used along with the VWA001 MWM-Array. The drive-to-sense element gap of the array was set to 1-in. Teflon tape was applied to the portion of the sensor array in contact the Splashtron during the scans to protect the sensor array. The surface of the insulation was uneven; the cloth tape was spiral-wrapped around the insulation creating a surface roughness periodicity of roughly 0.25-in. and the nominal thickness of the

coated pipe sections could change, with a circumference change of 0.5-in. common over the span of several feet. Although the foam backing between the sensor array and the support plastic layer wrapped around the pipe provides some compliance, it was not enough to accommodate such large circumferential changes. Consequently, shorter scans were generally required where the coated pipe diameter did not change dramatically over the scan. In follow-on efforts, we plan to develop other methods for maintaining a constant gap between the sensor and the outer pipeline steel surface (or the pipeline centerline).

For these measurements an air-shunt calibration was performed. Scans were performed at several positions around the circumference to construct a scan image. Each pass of the array imaged approximately ¼ of the pipe surface so four passes spaced approximately 90 degrees apart were used to image the pipe circumference. A chalk line was used to maintain the circumferential position during each scan. The measurement data for each channel was converted into an effective lift-off and permeability using measurement grid methods. Excitation frequencies of 10, 100, and 630.9 kHz were used along with a high-frequency probe; the best results were generally observed with the 100 kHz data.

Figure 47 through Figure 49 show preliminary results over several detected flaws in the pipe underneath the coating. The *x* and *y* axes in the images have dimensions of inches. These are absolute images, without intelligent filtering, where the impedance measurement data has been processed with measurement grids to determine the lift-off (proximity of each sense element to the steel pipe surface (which provides an image of the surface topology, i.e., geometric variations) and the relative permeability for the outer surface steel pipe wall (which is related to material property and residual stress in the outer surface of the steel wall). Flaw responses are evident in each of these images and appear as a local increase in lift-off and variation in magnetic permeability; variations in lift-off that are not associated with a change in the magnetic permeability are caused by coating thickness variations (thus, with intelligent filtering, we anticipate a low false indication rate). Note that no attempt was made to filter these images to reduce channel-to-channel variability (or striping) of the images at this time. It is anticipated that further enhancements in the fixturing and data processing will yield much better images.

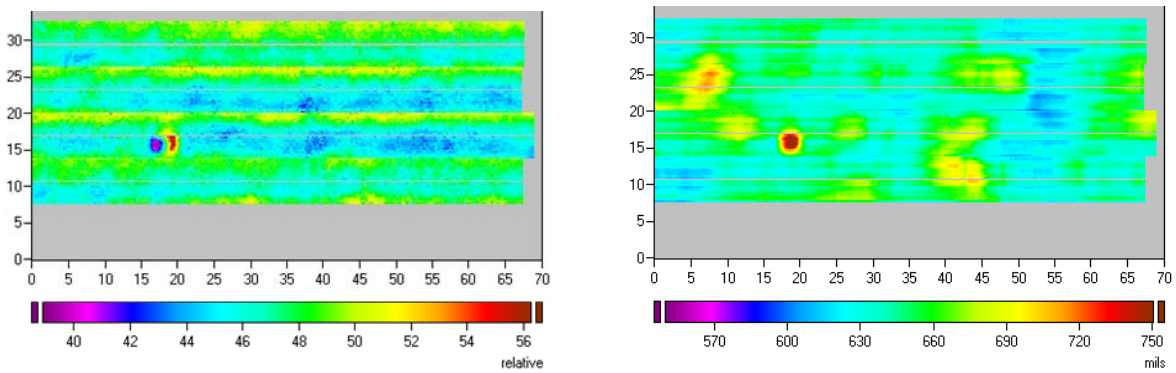

Figure 47. Scan images over an elongated flaw. (Left) Relative permeability. (Right) Lift-off.

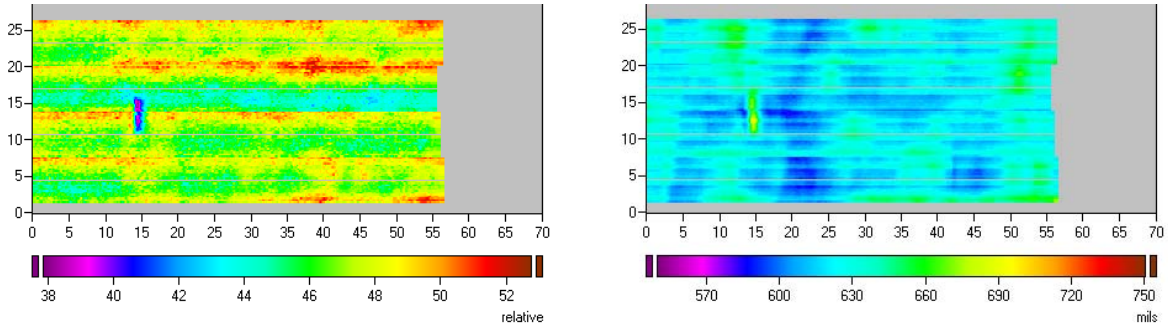

Figure 48. Scan images over a circumferential flaw. (Left) Relative permeability. (Right) Lift-off.

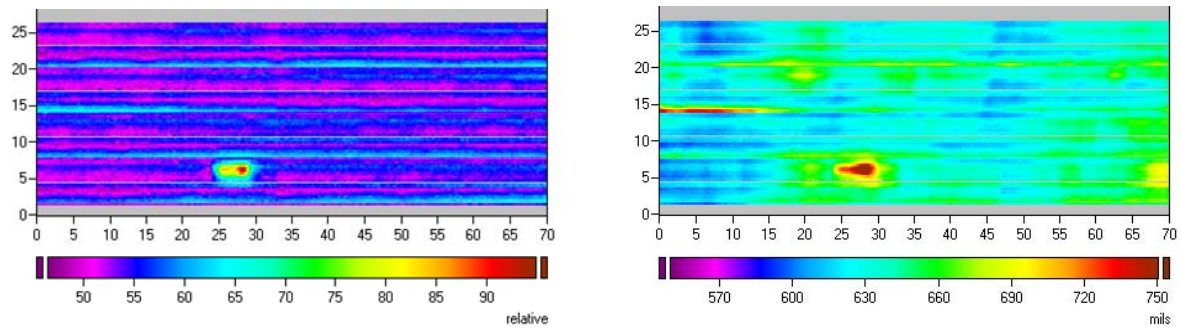

Figure 49. Scan images over an axial flaw. (Left) Relative permeability. (Right) Lift-off.

Scans were performed over four of the five pipe sections. For three of the pipe sections, scans were performed over both the end and middle sections which are separated by the ground support. The sensor fixture was not able to scan the pipe sections over the ground supports and these regions are considered uninspectable with this fixture. Figure 50 shows a representative composite image showing several scan images and a schematic of the pipe section. An axial flaw is visible in the leftmost images. The center region appears to contain two welds (circumferential indications) with a material change between the two pipe sections at the left weld and a defect near the right weld. The rightmost images do not show any flaws.

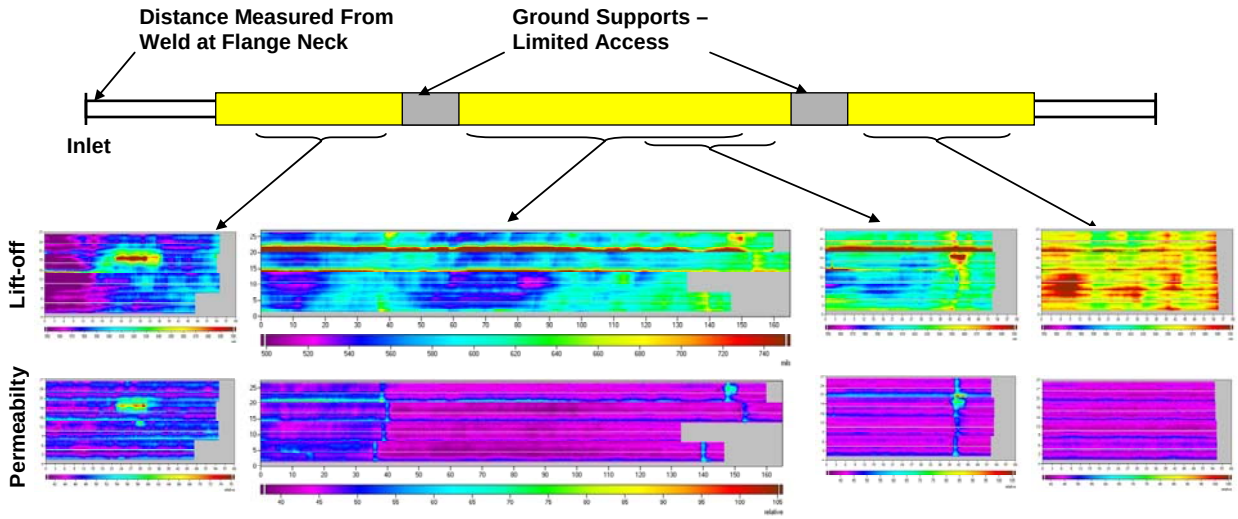

Figure 50. Composite image for one of the pipe sections.

The initial results obtained with the prototype scanning fixture are encouraging, but addressing some of the fixture limitations will result in equipment that can more readily be transitioned to field use for scanning through coatings. The limitations in the prototype fixture include: 1) the foam backing behind the sensor array not being compliant enough to accommodate the coating thickness variations; 2) the endmost sense elements not being reliably held near the pipe section surface; 3) the position encoder wheel not reliably providing scan position; and 4) the fixture weight needing to be reduced to more readily allow scans with the fixture upside down. Several of these limitations are addressed with the 2nd generation wrap-around fixture of Figure 14 and the hand-held fixture of Figure 15.

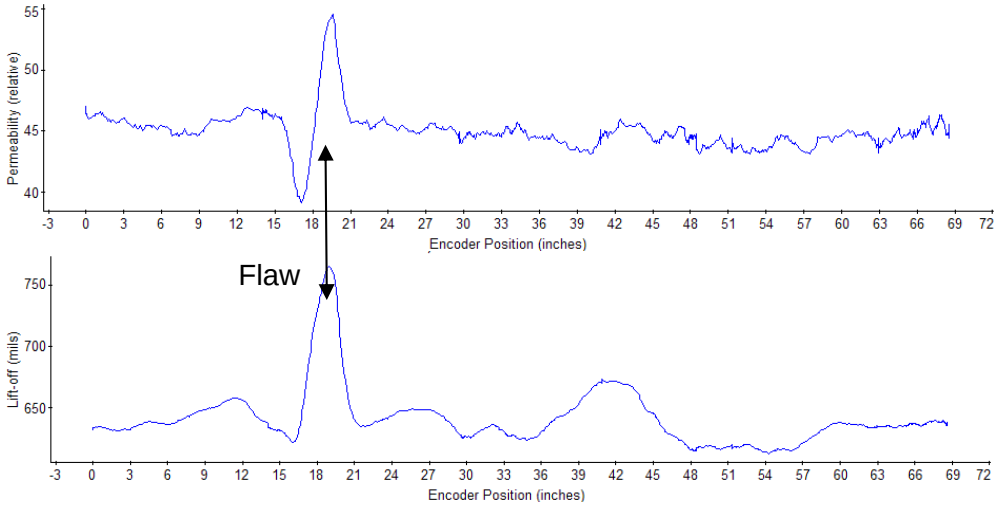

Figure 51. VWA001 response with a 1.0-in. drive gap at 100 kHz for the Chevron pipe samples having a 0.5-in. Splashtron coating for an oblong-shaped indication.

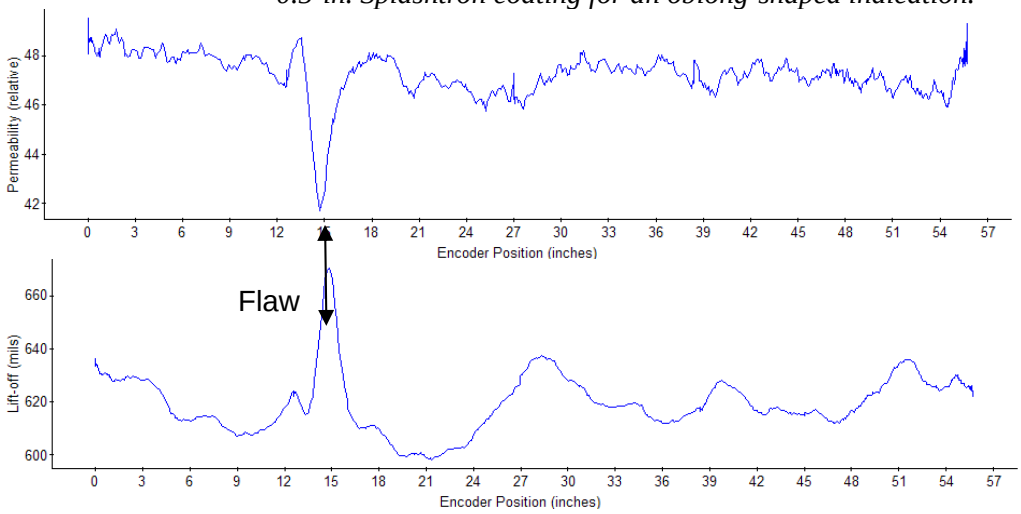

Figure 52. VWA001 response with a 1.0-in. drive gap at 100 kHz for the Chevron pipe samples having a 0.5-in. Splashtron coating for a circumferentially-oriented indication.

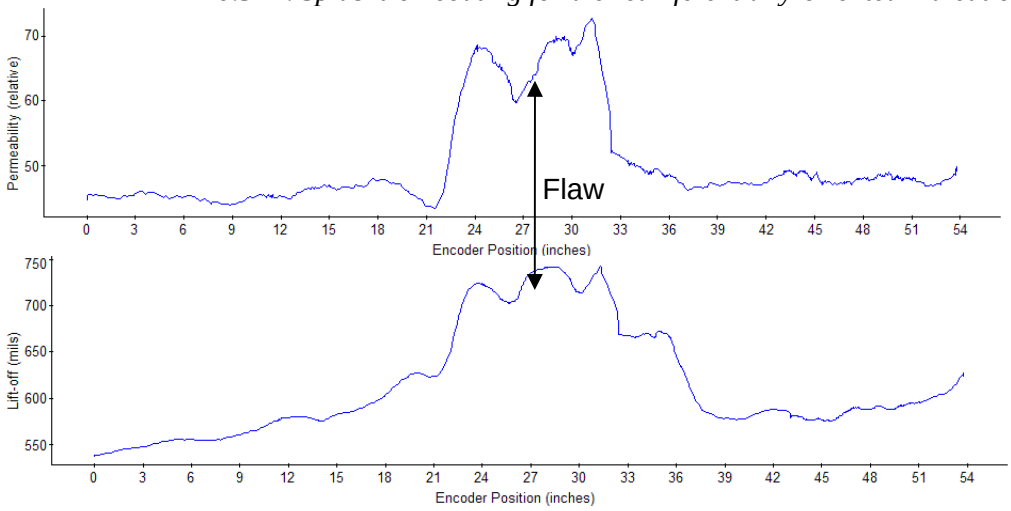

Figure 53. VWA001 response with a 1.0-in. drive gap at 100 kHz for the Chevron pipe samples having a 0.5-in. Splashtron coating for an axially-oriented indication.

A series of simulations were also performed to determine how the effective property values represent the near-surface material loss conditions. These simulations used a two-dimensional finite element model and calculated the effective permeability and lift-off as the flaw width and position relative to a VWA001 sensor array are varied. A drive width of 101.6 mm (4.0-in.), as in the VWA001, and a drive-sense gap of 25.4 mm (1.0-in.) were assumed. Figure 54 shows the results for a coating thickness of 12.7 mm (0.5-in.) and a flaw depth of 2.54 mm. For a 12.7 mm (0.5-in.) steel wall thickness, this corresponds to 20% material loss. For wide flaws with a width greater than about 50.8 mm (2.0-in.) the effective lift-off has plateau and peak that approach the lift-off change associated with the actual flaw depth and the effective permeability has a central peak with local minima on either side of the peak that occur when the drive winding closest to the sense element passes over the edge of the flaw. For narrow flaws, the peak in the effective lift-off becomes much smaller than the lift-off change associated with the presence of the flaw, which is consistent with previous work that showed that flaw geometry must be accounted for in the material loss depth estimates when the extent of the flaw becomes small compared to the sensor dimensions. Note that the extent of the material loss is approximately equal to the full-width-at-half-maximum for the effective lift-off response. The effective permeability has a relatively complicated dependence on the flaw width and scan position; however, it is worth noting that these plots are consistent with the measurement results obtained for oblong, axial, and circumferential flaws in the 6-in. diameter pipe sections shown in Figure 51 through Figure 53. Similar results are obtained when the coating thickness is increased to 25.4 mm (1.0-in.), as shown in Figure 55, or when the material loss is increased to 7.62 mm (60% material loss for a 12.7 mm wall), as shown in Figure 56. This indicates that the effective lift-off change needs a flaw-width correction factor to provide an accurate depth estimate, at least for the narrower flaws.

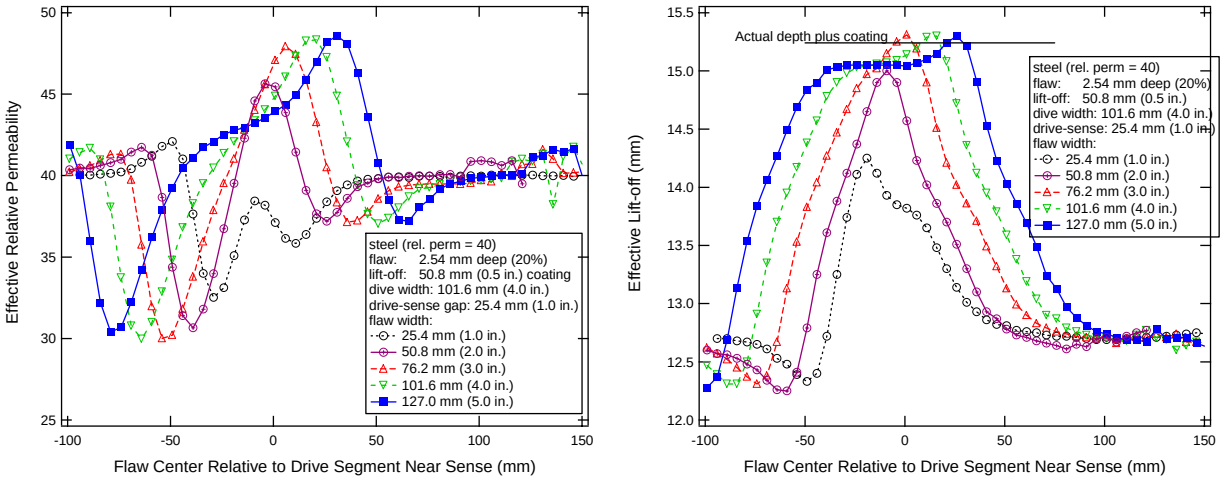

Figure 54. Effective property response as the flaw center and width are varied for the VWA001 with a drive-sense gap of 25.4 mm (1.0-in.). The coating thickness was 12.7 mm (0.5-in.).

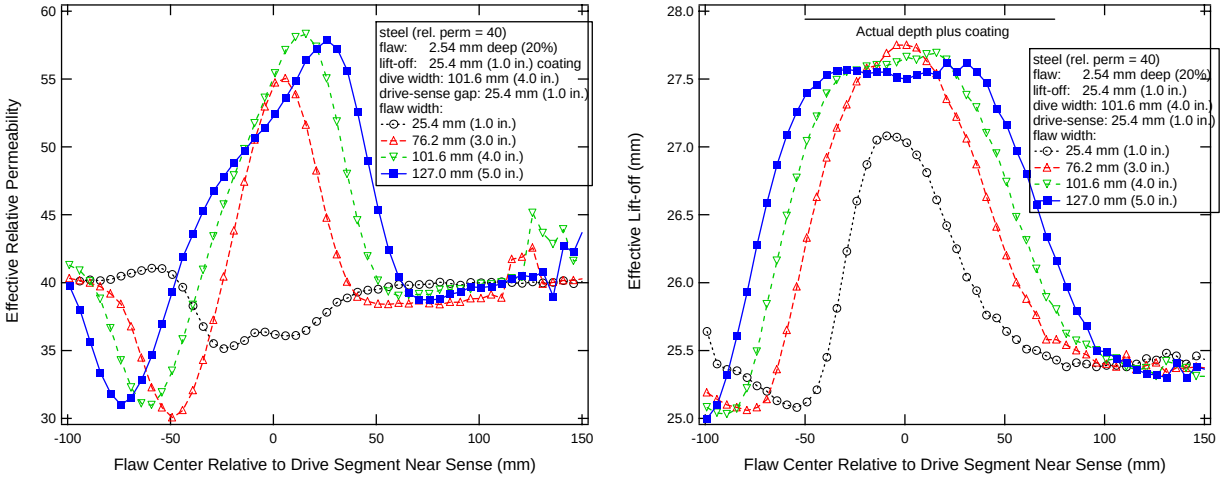

Figure 55. Effective property responses as the flaw center and width are varied for the VWA001 with a drive-sense gap of 25.4 mm (1.0-in.). The coating thickness was 25.4 mm (1.0-in.).

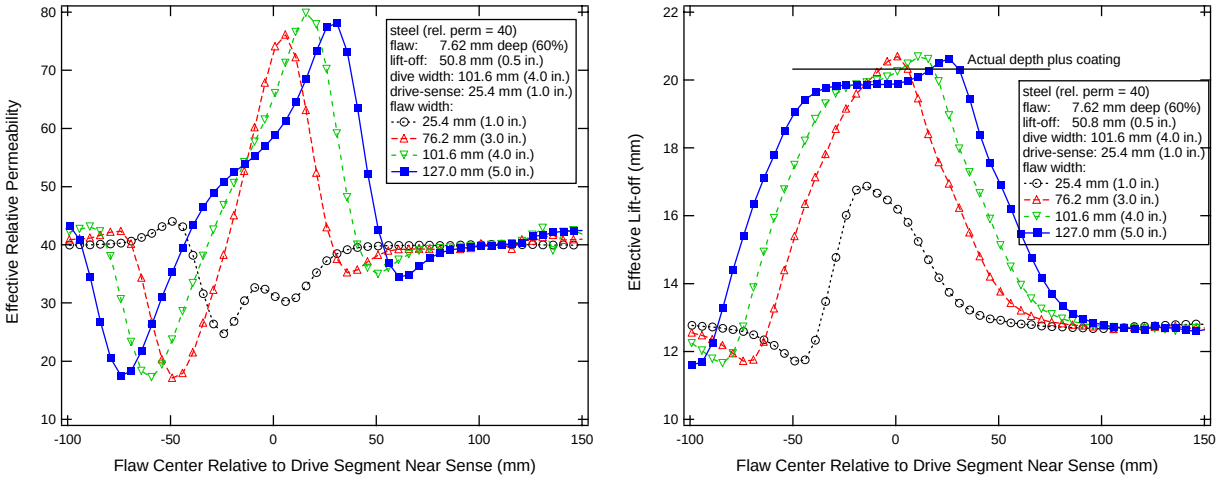

Figure 56. Effective property response as the flaw center and width are varied for the VWA001 with a drive-sense gap of 25.4 mm (1.0-in.). The coating thickness was 12.7 mm (0.5-in.). The depth of the flaw was 7.62 mm (0.3-in.).

6.4.2 In-line inspection imaging (Near-surface material loss from inside the pipeline)

Building upon the results of external scans for external material loss, the MWM-Arrays were adapted for scanning fixture to monitor near-surface internal material loss from the inside. Again, high frequency measurements were performed on a variety of samples. In all of the measurements, an insulating layer was placed between the MWM-Array and the pipeline surface. This was primarily for protection of the MWM-Array but it also simulates the presence of insulating liners. Several configurations were tested and led to two sets of pull tests on pipeline sections with simulated flaws; these pull tests were critical development milestones as they helped to establish the imaging capability of the MWM-Arrays and the capability to integrate the MWM instrumentation into an ILI-tool format.

6.4.2.1 Initial measurements on laboratory pipe sections

For performing initial internal scans of the pipe sections, the ILI tool of Figure 16 was used. A standard FA28 MWM-Array sensor was installed in the ILI tool. The FA28, shown in Figure 3, has two rectangular drive windings placed adjacent to each other and a linear array of thirty-seven sense elements that are 1 mm (0.040-in.) square. This provides a net scan width of the sense element array as 37 mm (1.48-in.). The linear array of sense elements is centered inside one of the drive windings so that the gap between the sense elements and the drive winding is only 0.25 mm (0.010-in.). Since this MWM-Array has small dimensions, it is suitable for creating high spatial resolution images and detection of areas of damage but it is less useful for discriminating between higher levels of material loss, such as between 25%, 50%, and 75%. The scanner incorporates a linear position encoder to provide the array position during the scan. For all of these tests, the sensor was calibrated in air before the tool was inserted into the pipe sections.

For the inspection program from inside the pipeline, two pipe sections were acquired, with one 10 ft long and the other 4 ft long. Both pipe sections had an outer diameter of 6.625-in. and a wall thickness of 0.4-in. The longer section was used for testing longer cables and longer scan distances while the shorter section was acquired since it is easier to machine flaws into the inner surface and more suitable for demonstration measurements. Figure 57 shows a schematic diagram of the flaws machined into the 4 ft pipe section. Two rows of flaws were machined into the inside surface to represent internal material loss. This was accomplished by drilling holes through the pipe on the opposite sides from the flaws. As indicated in the schematic, the flaws are located 90° apart and have nominal diameters of 0.5 and 1.0 inches. The flaws have depths corresponding to 25%, 50% and 75% material loss. These depths were chosen since they are appropriate for repair/replace maintenance decisions for pipelines.

Initial measurements were performed with scans along the longer (10 ft) pipe section. Although there were no flaws machined into this section, this allowed baseline measurements to be performed with a relatively long 40 ft cable. A foam layer behind the sensor array held the MWM-Array against the steel surface during the scan. A 0.005-in. thick Teflon layer was placed over the sensor to protect the array during the scans. Figure 58 shows the front of the tool at several positions in the pipe section. Since the sensor was in contact with the surface it acted as a brush so that a significant amount of rust was pushed through the section with the scanner. This rust did not affect the measurement data, shown in Figure 59, as the images are essentially constant across the length of the scan, but it suggests that a non-contact measurement would be better. Also, the roughness of the surface could potentially erode the wear layer quickly and lead to sensor damage. The noise in the images is due to the color scales being narrow. This data was taken with a linear scan rate of 2 to 3 inches/second (1.4-2.0 mph). This is a little faster than typical tethered tool scan rates of roughly 0.5 mph, but this leaves room on the instrumentation side for introducing multiplexing to support more sense elements in the sensor array to provide complete coverage with a single scanner pass.

Additional measurements were performed with the scanner inside the 4 ft pipe section that had regions of material loss machined into the inner surface. One set of measurements involved stationary

measurements where the lift-off was intentionally varied but the sensor position within the pipe section was kept constant. The Teflon layer over the sensor array was removed and an air calibration was performed. Measurements were then taken as one, two, and then three layers of 0.005-in. thick Mylar were inserted between the FA28 MWM-Array and the inside surface of the steel section. Figure 60(left) shows that the measured lift-off for each channel of the array increases with the shim thickness. There is some channel-to-channel variability, but this can be removed with normalization of the data across channels. Figure 60(right) shows the data for a single channel on a measurement grid. The data varies in the lift-off direction toward the air point. These measurements and plots verify that the instrumentation and models are functioning properly.

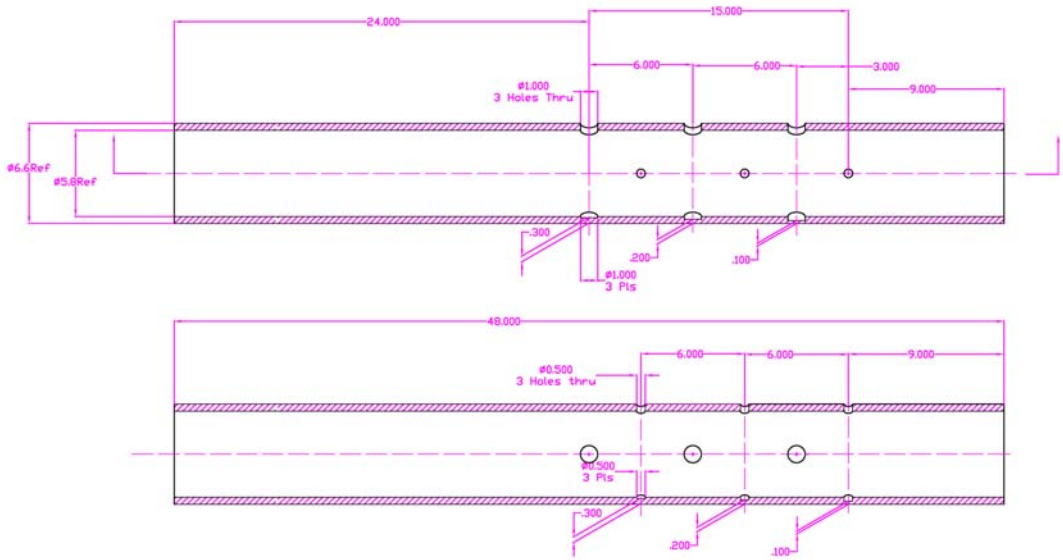

Figure 57. Schematic drawing of the flaws machined in the inside of a 4-ft steel pipe section to represent internal material loss.

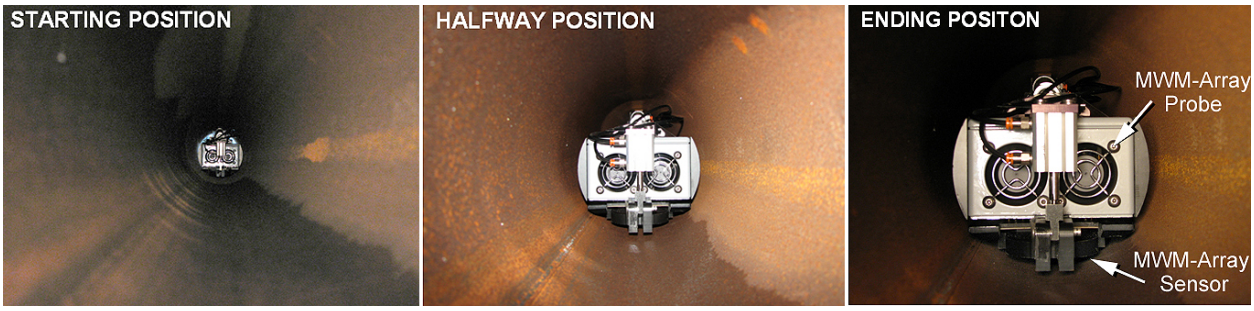

Figure 58. Three transition photographs of the ILI tool traveling down the length of a 10 ft steel pipe section at JENTEK test facilities.

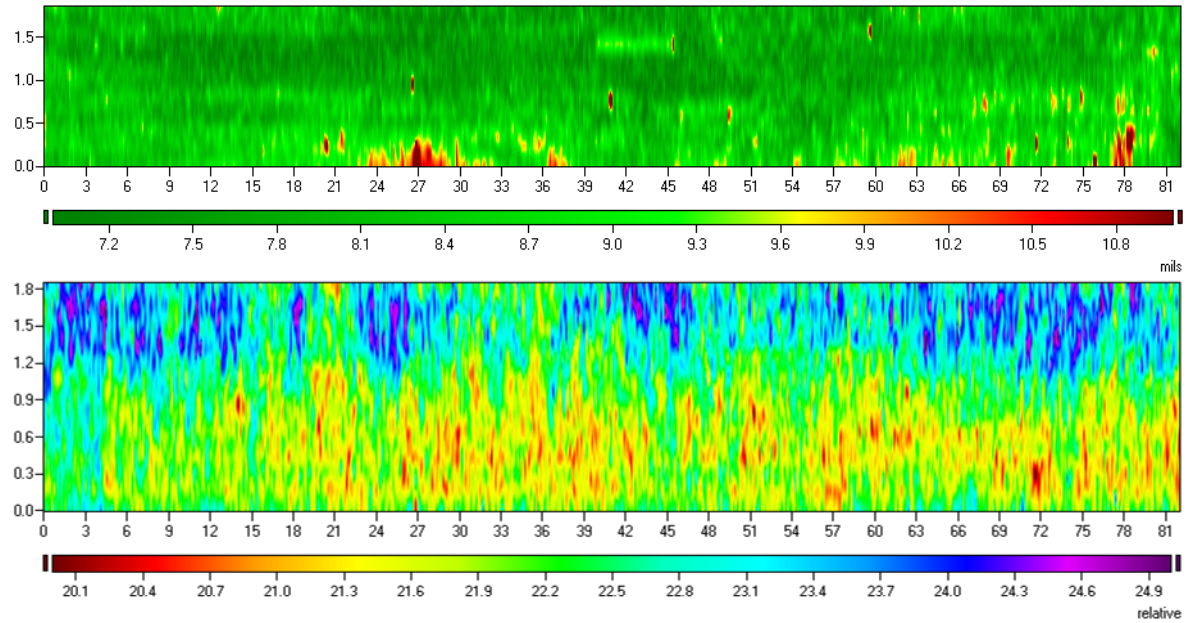

Figure 59. Example images from an FA28 MWM-Array scanned down a 10 ft pipe section. These measurements were taken at a frequency of 1 MHz. The upper plot shows the lift-off and the lower plot shows the relative permeability. The left and bottom axes of the images are in inches.

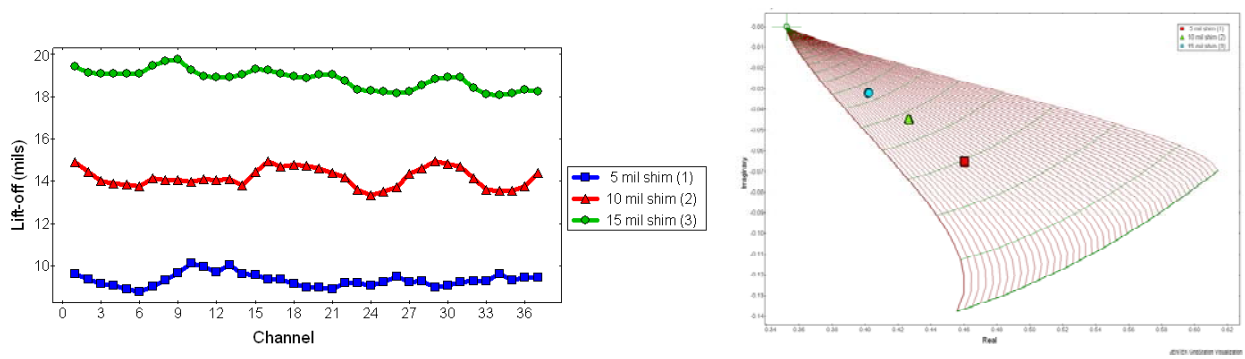

Figure 60. (Left) Lift-off response for each channel of an FA28 MWM-Array inside the 4 ft pipe section. (Right) Data for a single channel plotted on a measurement grid. The excitation frequency was 316 kHz.

The second set of measurements involved scanning over the material loss regions. A 0.005-in. sheet of Mylar was placed over the two rows of material loss regions machined into the inner surface to protect the sensor during the scan. This was necessary since the sensor currently has a foam backing. A rigid backing that approximates the curvature of the inside surface could also be used with slides placed at edges of this rigid backing that provide a reasonable sensor standoff from the surface and permit the scanner to travel through the pipe section. Figure 61 and Figure 62 show the lift-off and permeability images for the material loss regions for a scan rate of 1 inch/second (0.7 mph). The material loss regions were distinct and the high spatial resolution images with the FA28 capture the spare accurately. Figure 63 shows the B-scan plot of the lift-off for the 1.0-in. diameter material loss regions. In this case, the depth of the material loss regions was large (0.1, 0.2, and 0.3 in.) compared to the FA28 sense element-to-drive gap and the sensor did not distinguish between them. This suggests that a longer spatial wavelength sensor, such as an FA24, would be more appropriate for characterizing the near-surface material loss with an ILI tool.

The initial measurements with this scanner showed that the MWM-Array technology can be used to image in material loss regions inside the steel pipe sections, the data acquisition rate is reasonable for

limited areal coverage, and relatively long cables (40 ft) can be used between the sensor probe electronics and impedance measurement instrument.

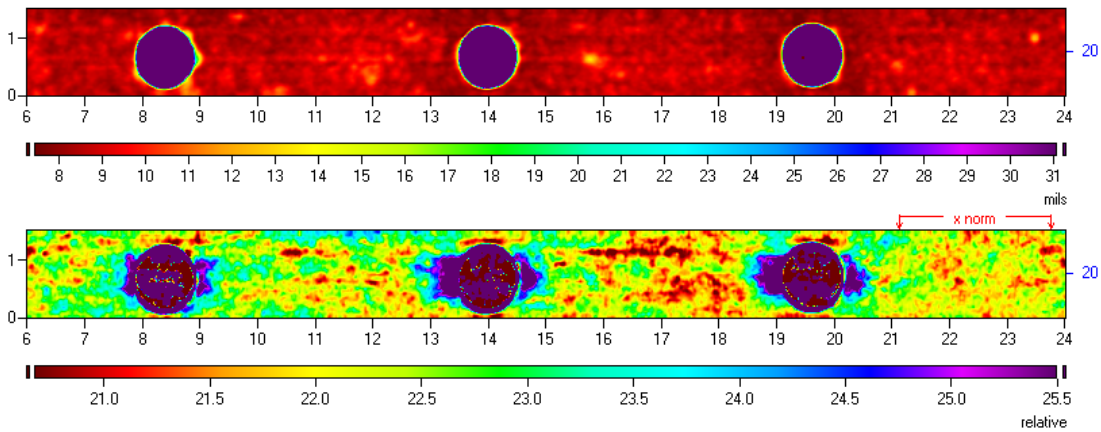

Figure 61. Example images from an FA28 MWM-Array at 316 kHz scanned over the 1.0-in. diameter material loss regions inside a 4 ft pipe section. The upper plot shows the lift-off and the lower plot shows the relative permeability. The left and bottom axes of the images are in inches.

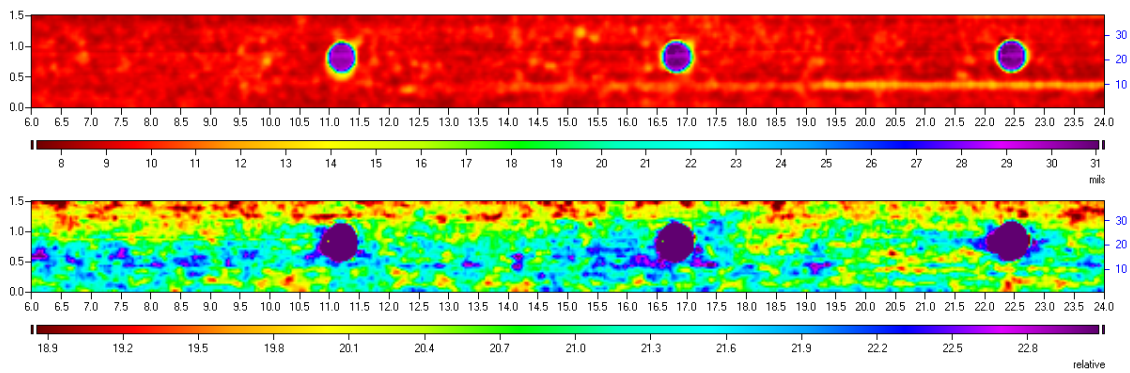

Figure 62. Example images from an FA28 MWM-Array at 316 kHz scanned over the 0.5-in. diameter material loss regions inside a 4 ft pipe section. The upper plot shows the lift-off and the lower plot shows the relative permeability. The left and bottom axes of the images are in inches.

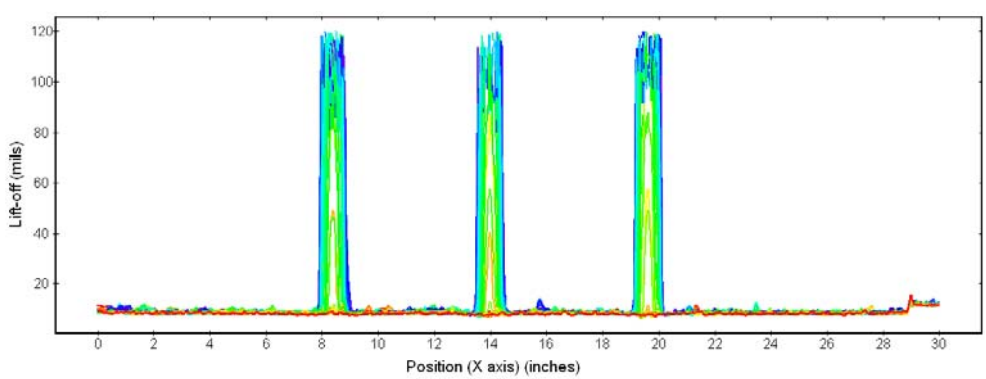

Figure 63. B-scan plot of the lift-off for an FA28 MWM-Array scanned over the 1.0-in. diameter material loss regions inside a 4 ft pipe section. These measurements were taken at a frequency of 316 kHz.

6.4.2.2 Pull Test 1 Results

In December, 2010, the first pull test was performed at the NDT Systems and Services (NDTSS) pipeline test facility in Houston. These measurements had an MWM-Array mounted on a prototype scanner frame and pulled through a straight pipeline test article. This demonstration focused on high frequency measurements for near-surface damage inspection with a goal of understanding issues associated with placing JENTEK MWM-Array sensors and instrumentation into an in-line inspection (ILI) tool. The pipeline test sections had a series of machined areas of material loss on the internal and external surfaces of the pipe wall. Measurements with an FA24 MWM-Array imaged each of the flaws.

Figure 64 shows a schematic of the pipeline test section. Three pipes were connected together in a straight line for testing at the NDTSS pull test facility. Each pipe section has an outside diameter of 18-in. and a series of flaws machined into the pipe walls, with the flaws ranging in size from 0.5 to 2.0-in. and depths ranging from 20% to 95% of the wall thickness. Pipe sections 1 and 3 were 20 ft long and contained a mixture of internal and external flaws. The flaws are generally located every 90º around the circumference. The internal flaws are located within 18 to 30-in. of the inlet end of each section. Pipe section 2 was 10 ft long and contained a single row of internal flaws at the 3:00 orientation and a single row of external flaws at the 6:00 orientation. The wall thickness for pipe section 1 was 0.5-in and 0.25-in for the other two sections. The pipe sections were connected so that the 12:00 orientations for pipe sections 1 and 3 and the 3:00 orientation for pipe section 2 were aligned. For these measurements the focus was on the internal flaws since a high frequency array was being used for the initial testing. Figure 46 shows photographs of the pipe sections, the prototype scanning fixture, and the position of the instrumentation during the measurements. Note that sections 1 and 3 were API 5L BX42 grade steel and the grade of section 2 is not known at this time.

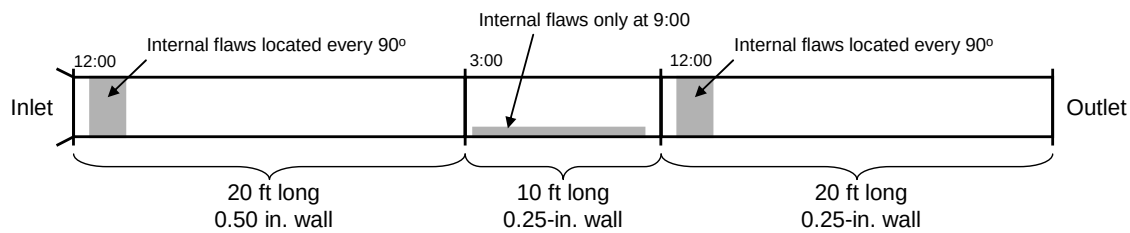

Figure 64. Schematic diagram of 18-in. outside diameter pipeline section at NDTSS pull facility.

Figure 65. Photographs of the pipeline section at the test facility.

For these measurements, the prototype tool of Figure 31 was used along with an FA24 MWM-Array. This MWM-Array has thirty-seven 0.1-in. sense elements and is suitable for a lift-off of up to about 0.125-in. An air-shunt calibration was performed, with the calibration parameters reloaded before each pull since the instrument had been powered off and the cable had been disconnected. Ranging was performed using measurements in air and on sample of steel pipe. Each pull had the sensor array at a single, fixed orientation. The measurement data for each channel was converted into an effective lift-off and permeability using measurement grid methods. An excitation frequency of 100 kHz was used. After each pull, the cable was disconnected from the instrument and pulled through the pipe section, and then reattached to the instrument when the prototype scanning fixture was returned to the inlet. Two slings were attached to the tool, one to interface with the winch which pulled the tool through the pipe and one to carry the cable that was used to pull the winch cable back through the pipe at the end of each run. Since the runs were relatively short, the rotation of the probe was minimal and not an issue for the measurements.

For the testing, seven pulls were performed on the first day of testing and 10 were performed on the second. The results from the 1st day of testing were encouraging as the flaws of interest were imaged. Several observations were made on the first day. First, several layers of Kapton tape were placed over the surface of the array as a wear layer. However the tape tended to tear along the edges and, when the array was placed at the bottom of the pipe (6:00 orientation), the array was torn upon exiting the pipe section. This suggested that a more durable, rigid, plastic layer should be used for the protective layer. Second, the tensioning bracket that held the sensor array and the position encoder, was binding and not supporting the array as hoped. This led to increasingly high average lift-offs from the wall surface and significant slippage of the position encoder. This binding was due to some clearances being too small and was remedied for the second day of testing. The position encoder also slipped primarily as the tool passed through the joints between pipe sections and the tool rocked back and forth. Substantially more reliable results were obtained on the second day of testing when the tensioning brackets were operating properly.

Figure 66 and Figure 67 show composite images obtained for a scan with the MWM-Array in the 12:00 orientation. The B-scan plots show the effective property (lift-off and permeability) variation for each sense element along the entire length of the scan. The data is plotted against the measurement number since the position encoder value was not reliable, primarily as the prototype tool passed between the pipe joints. Chatter in the response at the beginning and end of the scans when the tool was stationary are not plotted. The B-scan plots show the presence of two flaws in sections 1 and 3 that are near the inlet to each section. The flaws appear as a rapid local change in both the lift-off and permeability. Away from these flaws, the permeability is relatively constant in each section but a rocking motion with the sensor array fixture or prototype tool cause a periodic variation in the effective lift-off. It is anticipated that filters can be developed to remove this type of variation. The responses are normalized to help remove the channel-to-channel variations; however, the channel-to-channel variation is noticeable in section 3 near the end of the scan.

In section 2, the effective properties show a significantly greater spatial variation. The permeability is also generally higher; this observation is consistent with this pipe section being from a different lot of specimens. The unpainted portion on the outside of this section exhibited considerable generalized corrosion damage and similar generalized corrosion is expected on the inside. Although no internal flaws are expected for section 2 in this orientation, there is a local change in the lift-off and permeability that is consistent with the presence of a flaw. This indication was apparent in all orientations and may be associated with the motion of the prototype tool as it passes through the joint between the pipe with a 0.5-in. wall into the pipe with a 0.25-in. wall.

Figure 66 and Figure 67 also show C-scan images of the effective properties in the vicinity of the circular flaws. In this case, assuming a constant pull speed, then the measurement number can be used to obtain the scan distance using a scale factor of 0.0653-in./measurement. In each section the pairs of flaws start 24-in. from the inlet of the section. For section 1 the measured distance is slightly smaller probably

because the array was positioned slightly inside the pipe section at the start of the measurements. For section 3, the measured distance is about 25-in. from the joint. The flaws are approximately circular in shape, as expected. The similarity of the results in Figure 66 and Figure 67 indicate good measurement repeatability.

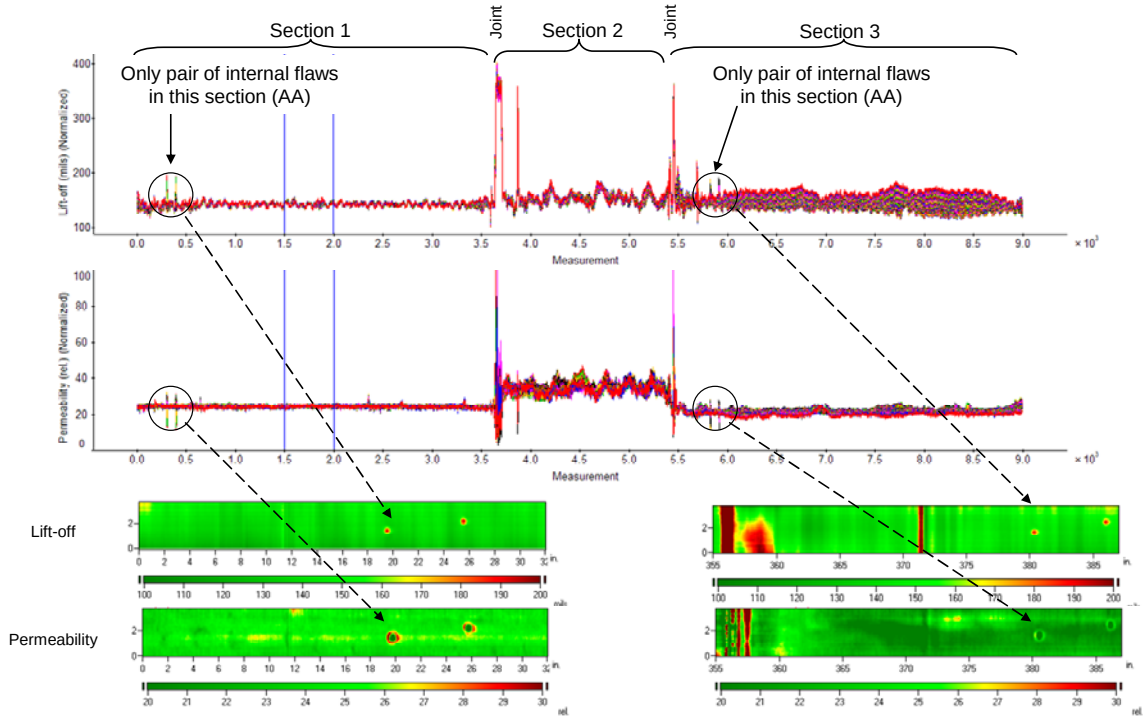

Figure 66. Composite image from 12:00 orientation (pull 8).

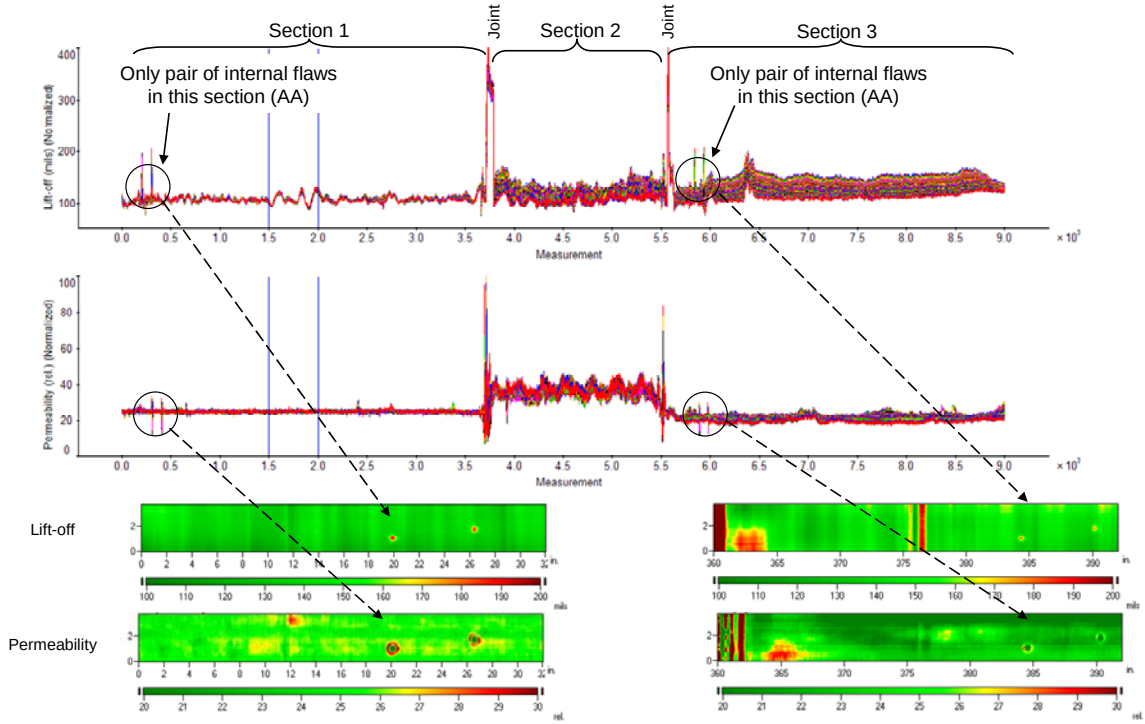

Figure 67. Composite image from 12:00 orientation (pull 9).

Figure 68 and Figure 69 show composite images obtained for a scan with the MWM-Array in the 3:00 orientation. Again, the flaws appear as a rapid local change in both the lift-off and permeability in the B-scan plots. In the C-scan images, the flaws appear as circular changes in the effective properties. The spacing between the flaws is approximately 6-in. and the orientation is not the same for each flaw within a pair; this is consistent with information that is known about the flaws.

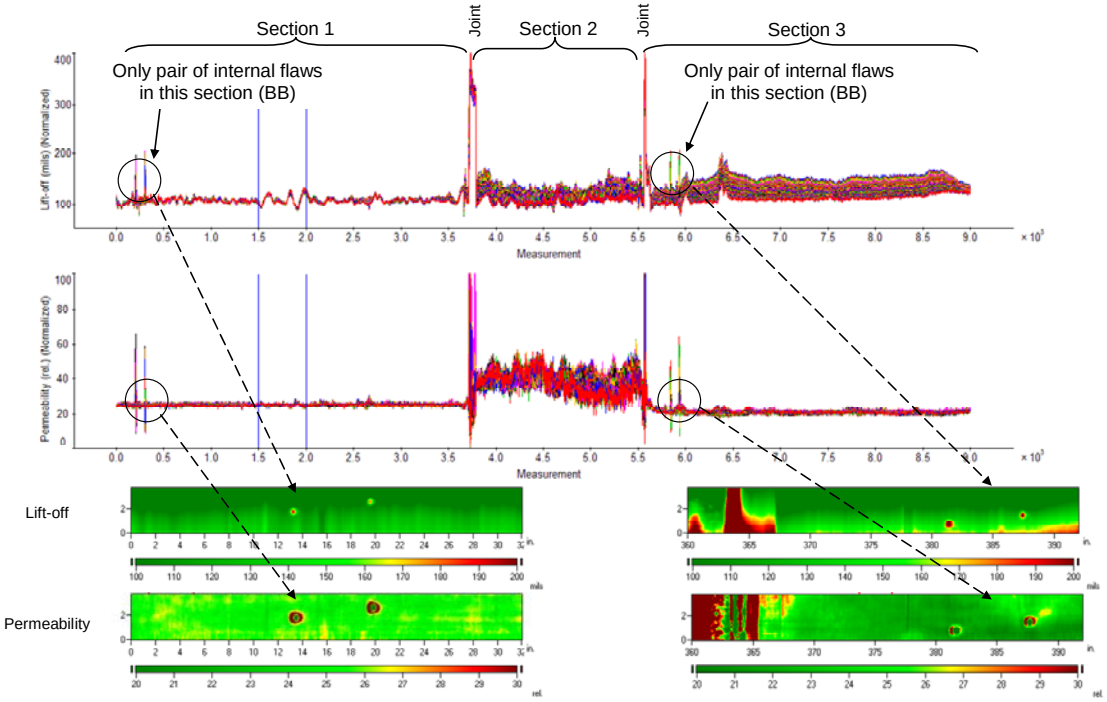

Figure 68. Composite image from 3:00 orientation (pull 10).

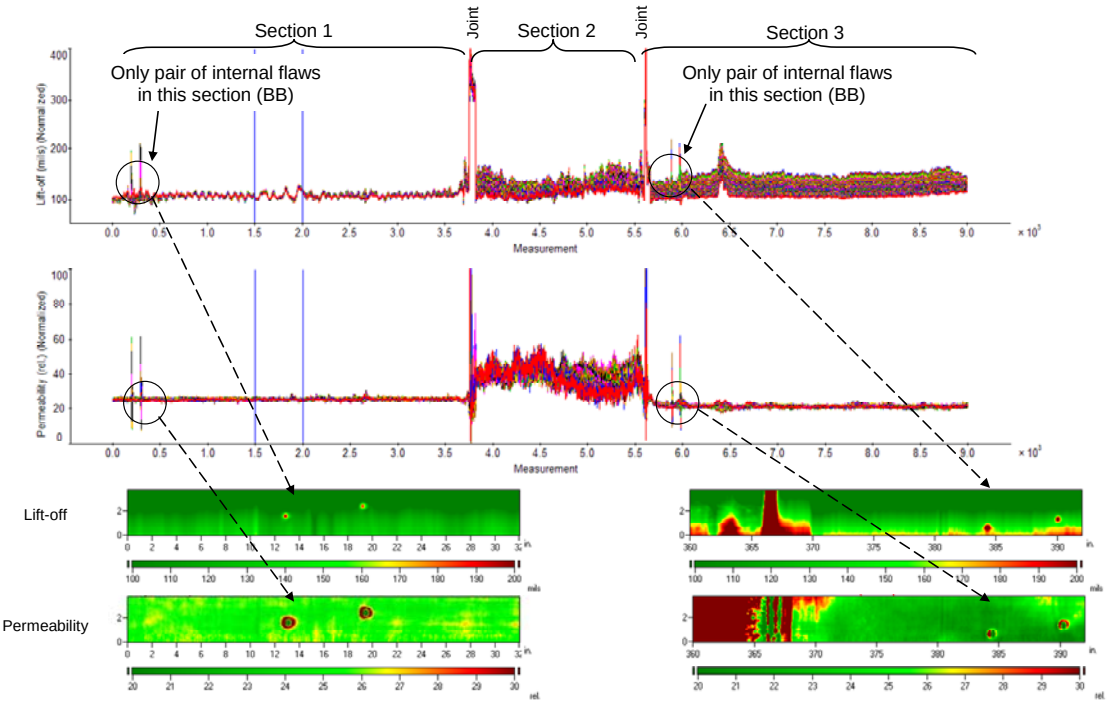

Figure 69. Composite image from 3:00 orientation (pull 11).

Figure 70 and Figure 71 show composite images obtained for a scan in the 9:00 orientation. In this case, the flaws appear as slot changes in the effective properties. The spacing between the slots is approximately 8-in. The slots are 0.75-in. wide and 2-in. long; since the sense elements only span 3.7-in. for this MWM-Array, the entire shape is only captured when the array is centered over the flaw, as in the bottom left images of Figure 71. This indicates that the MWM-Array is able to provide high spatial resolution images that capture the flaw geometry.

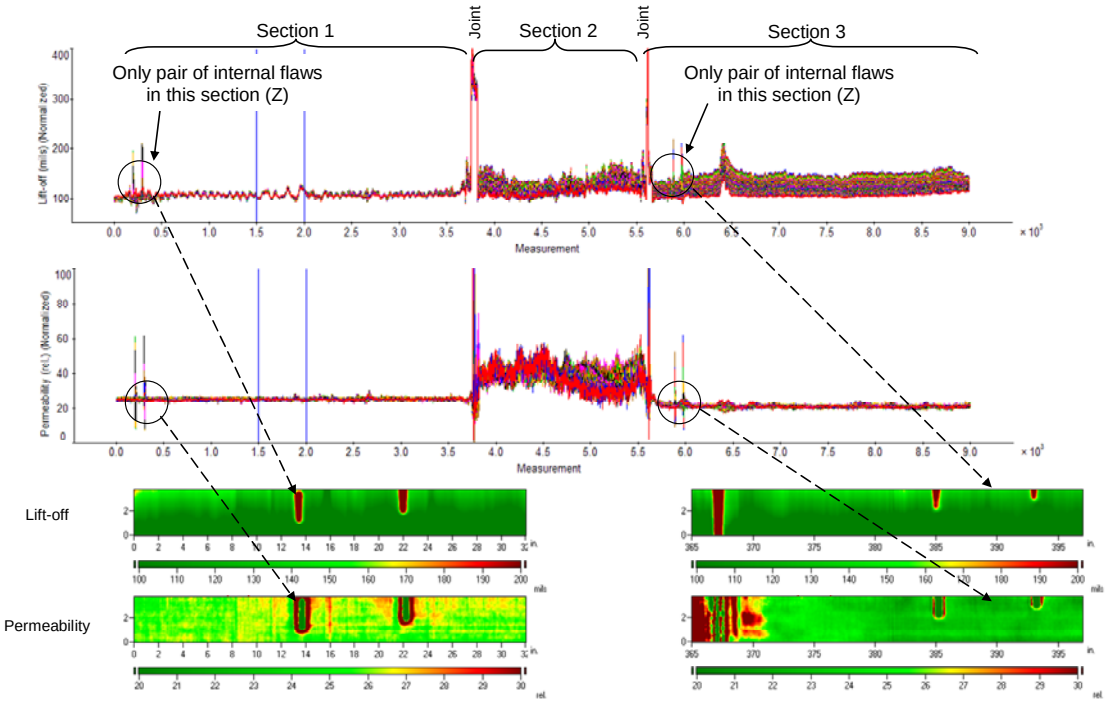

Figure 70. Composite image from 9:00 orientation (pull 12).

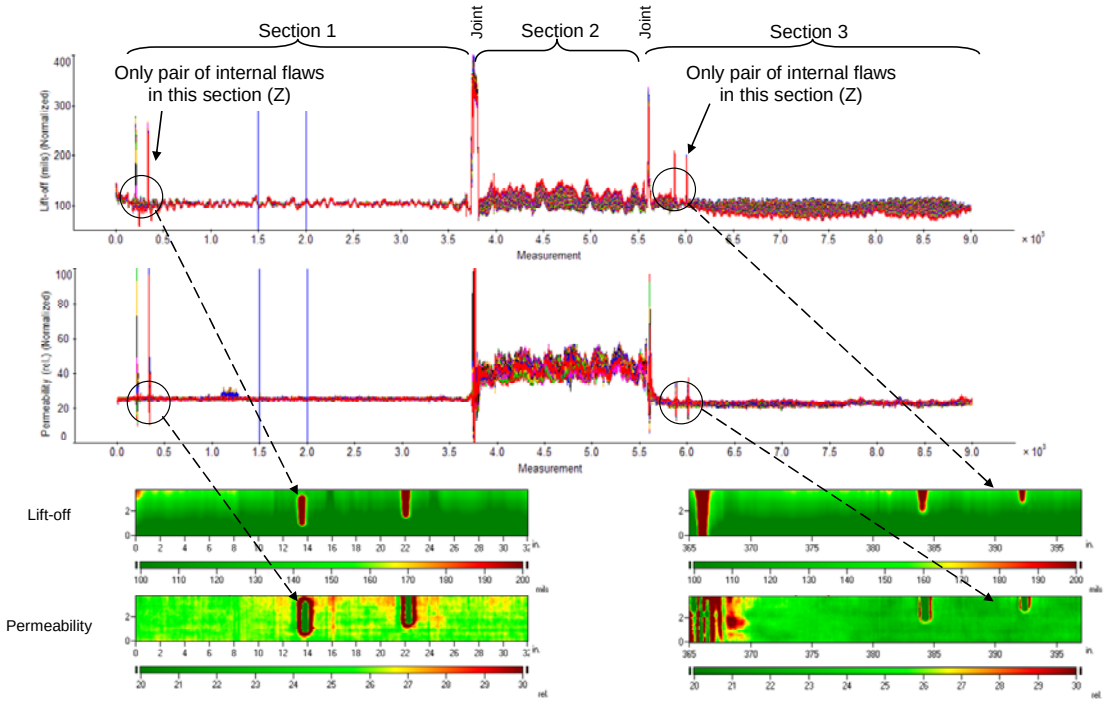

Figure 71. Composite image from 9:00 orientation (pull 13).

Figure 72 shows composite images obtained for a scan in the 6:00 orientation. In this case, the pipes were rotated so that the MWM-Array was facing upwards (in the 12:00 location) on the prototype tool. This permitted the 6:00 orientation to be scanned without damaging the MWM-Array, which occurred on the first day of testing when then tool was extracted on the outlet side of the pipe test article. In this orientation, two circular flaws are visible near the inlet region of sections 1 and 3, similar to the other orientations.

However, as indicated in Figure 72 and Figure 73, there is also a series of internal flaws of increasing size and depth in section 2 as well. Four circular flaws are visible in section 2. The baseline permeability is larger than in the other sections, consistent with this pipe section being from a different lot of material or possibly a different grade. There is also a substantial spatial variation in the permeability along the pipe surface. This appears to be due to generalized corrosion of this pipe section; it is our understanding that this pipe section had been exposed to the elements for a significant amount of time.

A fifth flaw close to the inlet region of section 2 is not visible. This is probably due to the MWM-Array not being held in proximity to the pipe surface as the prototype tool passes through the joint between sections 1 and 2. Sections 1 and 2 have different wall thicknesses and the rubber cups on the prototype tool did not hold the central body of the tool precisely in the center of the pipe. It appears that there was considerable motion of the MWM-Array as the tool passed through this joint, as evidenced by the relatively high lift-off obtained for all channels in the approximate location of this fifth flaw.

Figure 74 through Figure 77 show the results of two additional repeat scans at the 6:00 orientation. The flaw responses are very consistent, as is the background material property variations. This suggests that the background variations are not due to instrumentation noise and is probably due to actual material property variations or limitations of the scanning fixture.

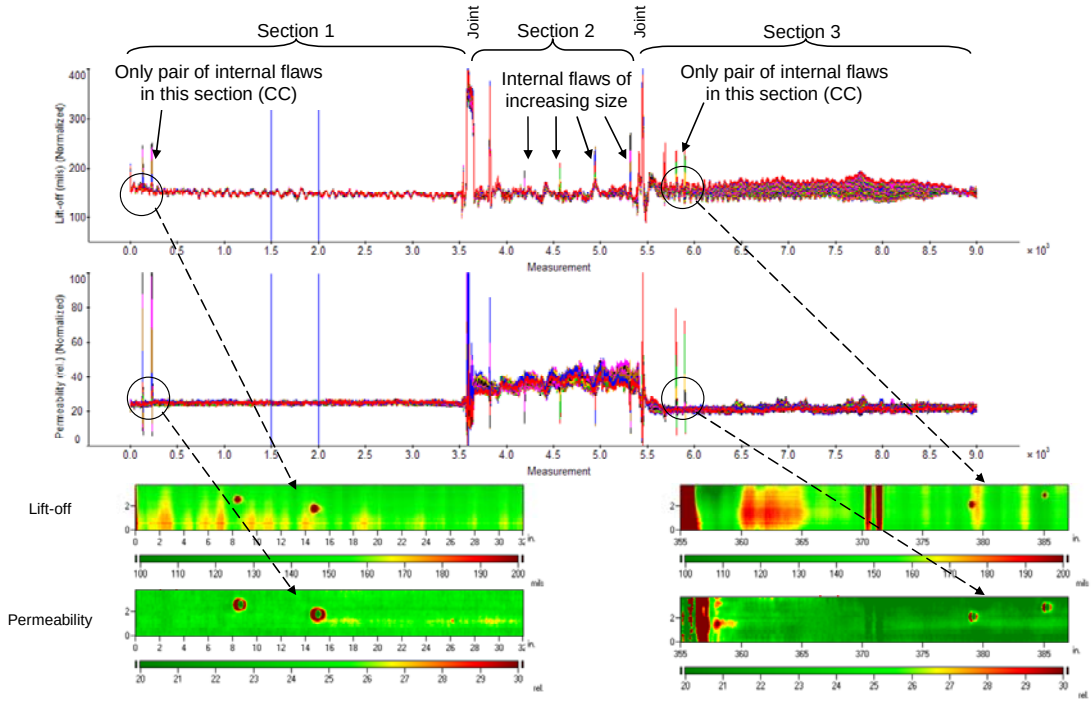

Figure 72. Composite image from 6:00 orientation (pull 14) for flaws in sections 1 and 3.

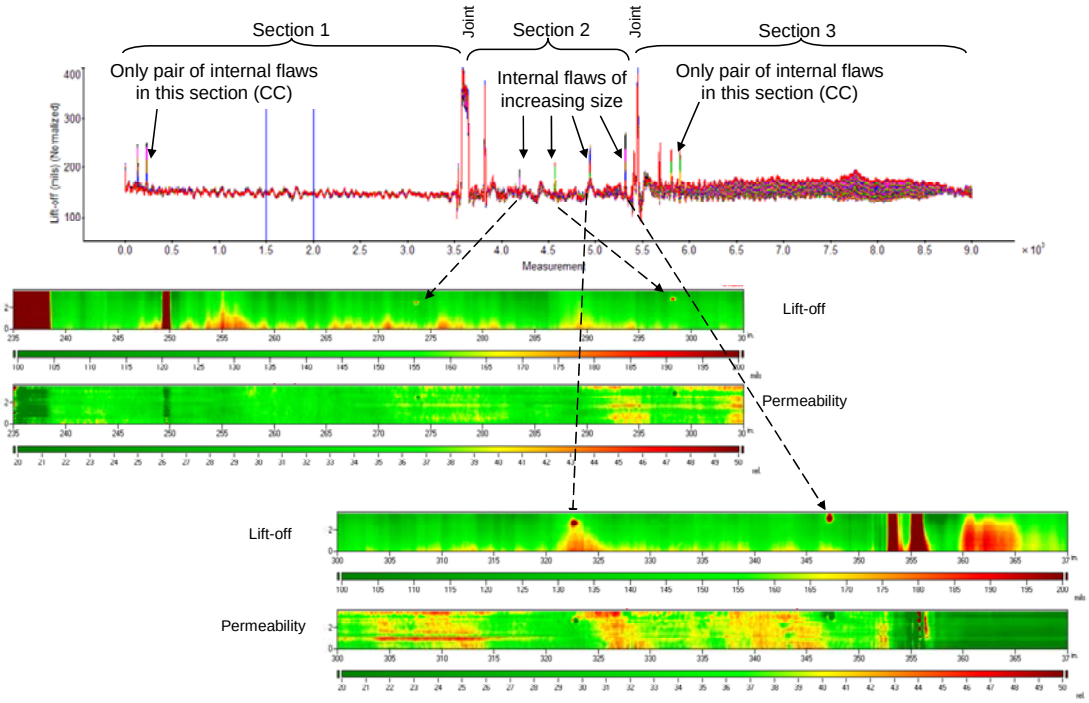

Figure 73. Composite image from 6:00 orientation (pull 14) for flaws in sections 2.

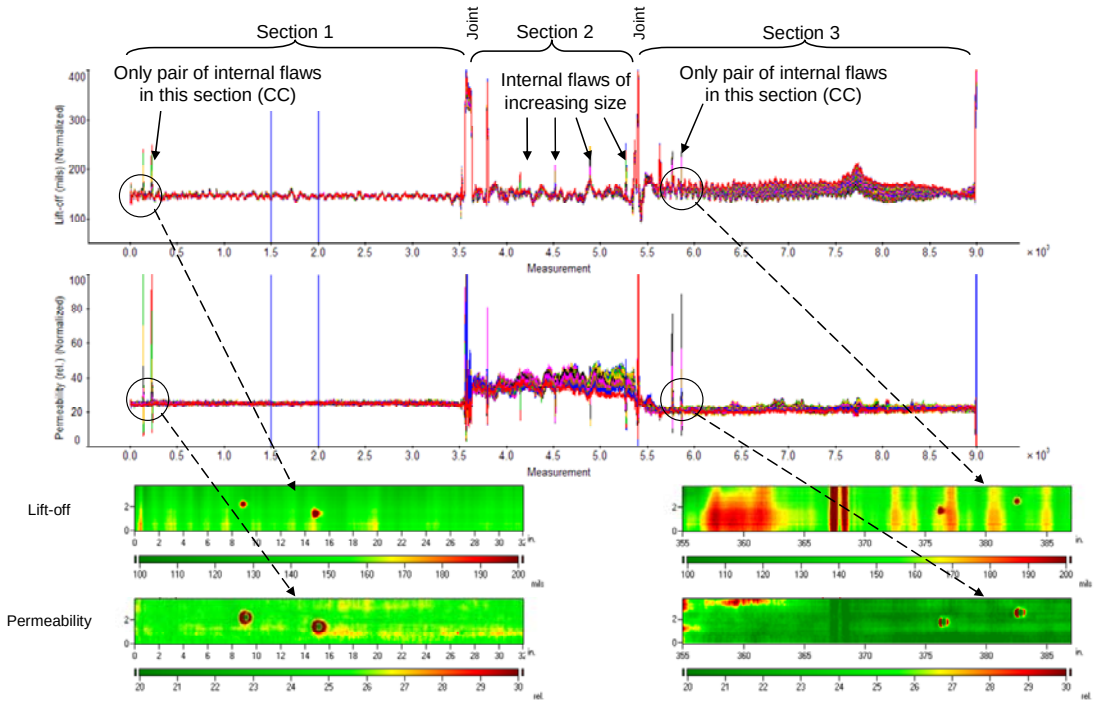

Figure 74. Composite image from 6:00 orientation (pull 16) for flaws in sections 1 and 3.

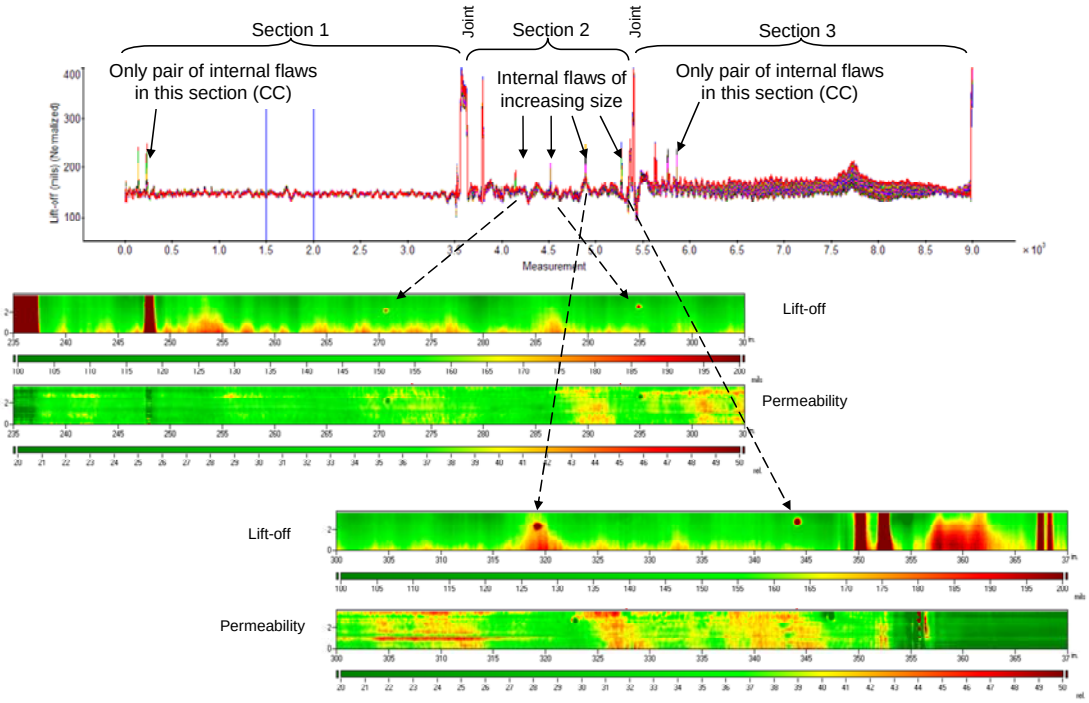

Figure 75. Composite image from 6:00 orientation (pull 16) for flaws in sections 2.

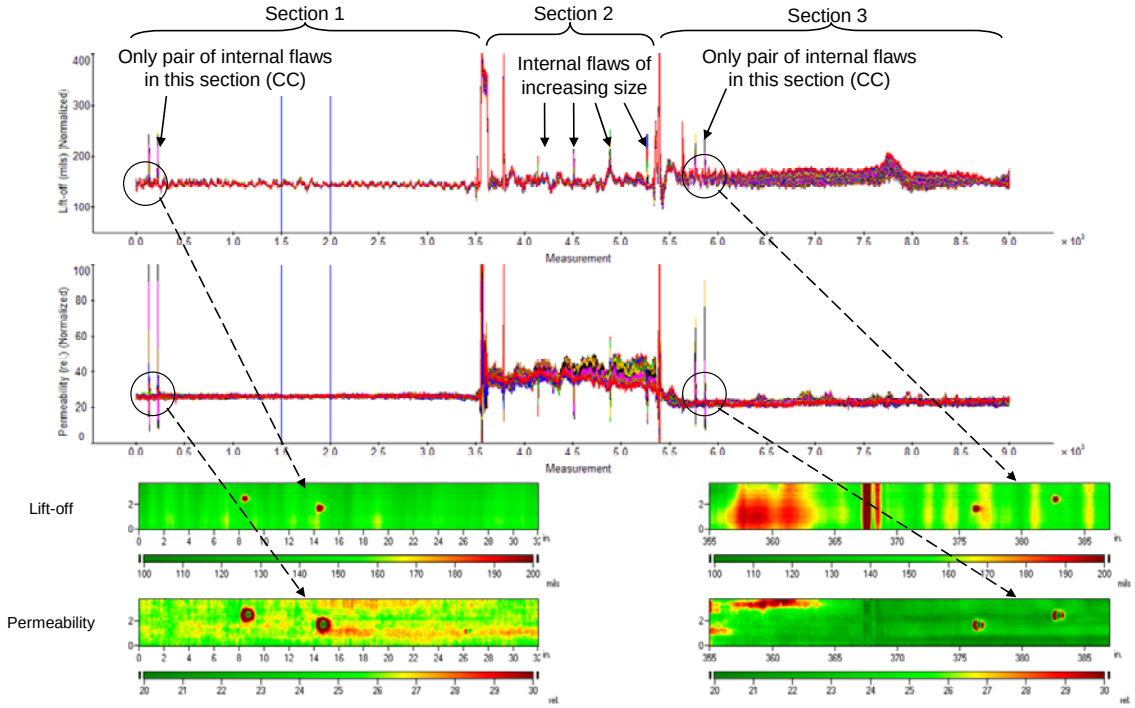

Figure 76. Composite image from 6:00 orientation (pull 17) for flaws in sections 1 and 3.

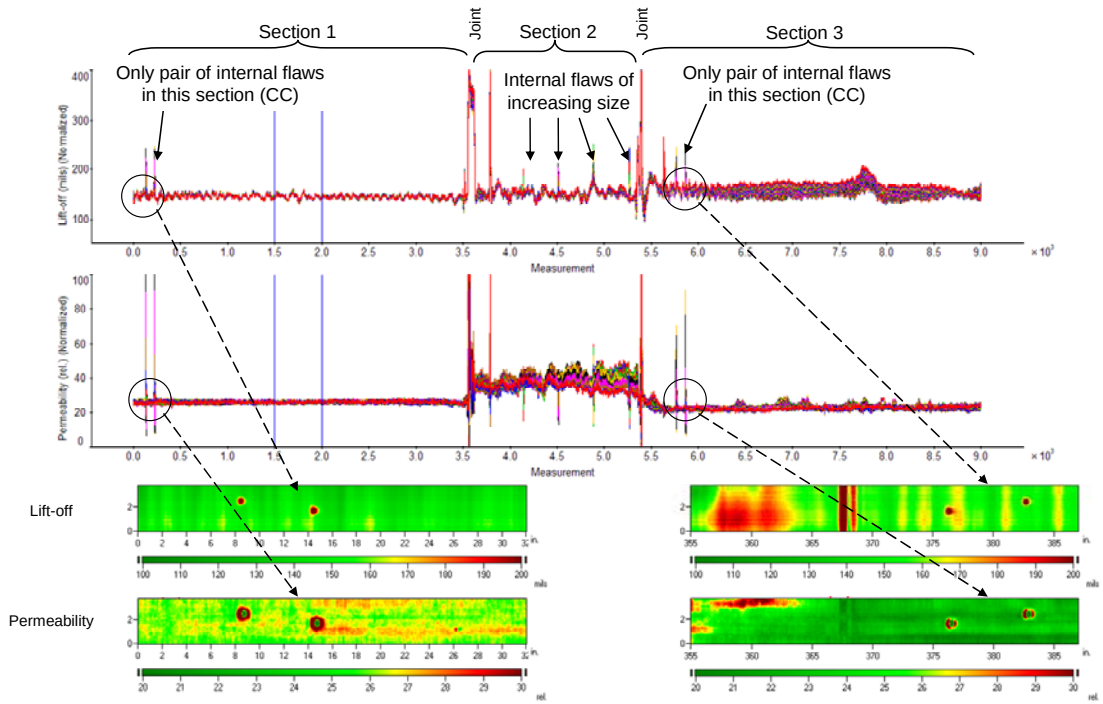

Figure 77. Composite image from 6:00 orientation (pull 17) for flaws in sections 2.

It was also observed that faint changes in the permeability images appear in regions where deep slots were machined on the external surface. For example, Figure 78 shows a composite image near the end of a scan in the 12:00 orientation. A pair of axial oriented slots, 6-in. apart, is visible in the effective permeability image and slightly in the effective lift-off image. These slots have 0.063-in. of remaining steel wall. Since the penetration depth at 100 kHz of the sensing magnetic field is less than this thickness, it is likely that observed responses is due to the machining process for making the flaws.

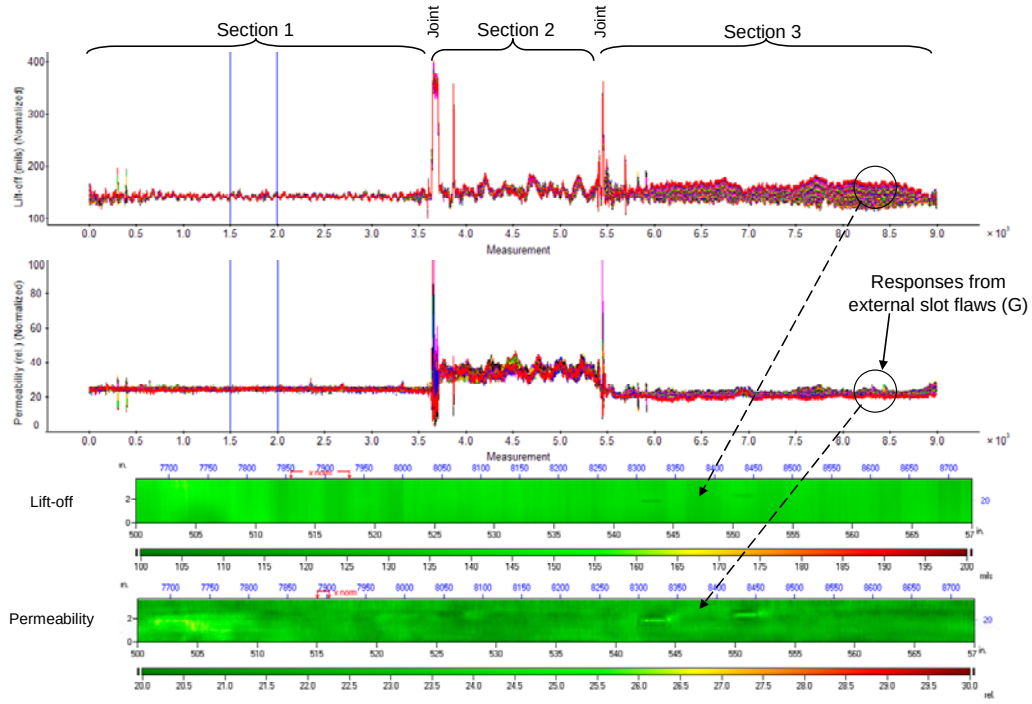

Figure 78. Another composite image from 12:00 orientation (pull 8).

Table 3 provides a list of the internal flaws on each of the pipe sections, along with the measured flaw dimensions. The measured diameter is obtained from the C-scan images as the average length and width of the color change from green to yellow; future work should redo this calculation by calculating the full width at half maximum value as this provides a better measure of the flaw dimensions. The measured depth is the change in the lift-off response and is taken as the difference between the peak value and an average value near the flaw; future work should correct this value to account for the flaw shape on the response as in Figure 26. This should bring the measured and actual depths into better agreement.

Table 3. List of internal flaws and properties on the pipe sections.

Section	ID	No.	Measured		Pull No.
			Dia. (in.)	Depth (mils)	
1	AA	1	0.5	65.5	8
		2	0.5	57.9	8
	BB	1	0.4	89.7	10
		2	0.3	83.0	10
	CC	1	0.7	83.0	14
		2	0.9	101.4	14
	Z	1	-	182.1	12
		2	-	186.0	12
2	a	-	-	-	14
	b	-	0.4	50.2	14
	c	-	0.5	57.6	14
	d	-	0.7	69.8	14
	e	-	0.9	115.6	14
3	AA	1	0.5	48.5	8
		2	0.5	44.5	8
	BB	1	0.5	93.1	10
		2	0.7	85.2	10
	CC	1	0.7	75.0	14
		2	0.5	83.7	14
	Z	1	-	112.8	12
		2	-	92.9	12

6.4.2.3 Pull Test 2 Results

In September, 2011, a second pull test was performed at NDTSS pipeline test facility in Houston. These measurements used the second generation prototype ILI tool of Figure 18, which was pulled through a straight pipeline test article. Figure 64 shows a schematic of the pipeline test section. This demonstration focused on high frequency measurements for near-surface damage inspection with a goal of understanding issues associated with placing multiple JENTEK MWM-Arrays and instrumentation into an in-line inspection (ILI) tool. The pipeline test sections had a series of machined areas of material loss on the internal and external surfaces of the pipe wall.

For this demonstration, two VWA005 sensors were used. As shown in Figure 3(e), these MWM-Arrays have eighteen 0.25-in. sense elements each, and are suitable for lift-offs up to about 0.25-in. An air-shunt calibration was performed. Ranging was performed using measurements in air and on a sample of steel pipe. The measurement data for each channel was converted into an effective lift-off and permeability using measurement grid methods. An excitation frequency of 100 kHz was used. Each pull had the two sensor arrays at two fixed orientation, 180° apart. With the linear position encoder located at the 12:00 position, channels 1 to 18 of one MWM-Array approximately span the 8:00 to 10:00 positions, respectively, while channels 19 to 35 of the second MWM-Array approximately span the 2:00 to 4:00 positions, respectively. With the linear position encoder located at the 9:00 position, channels 1 to 18 of one MWM-Array approximately span the 5:00 to 7:00 positions, respectively, while channels 19 to 35 of the second MWM-Array approximately span the 11:00 to 1:00 positions, respectively. Note that one of the sense elements of the second MWM-Array was not activated. The use of two MWM-Arrays meant that two sides of the pipe were being scanned with each pull and only two VWA005 MWM-Arrays were required to image the flaws that were nominally located at the 12:00, 3:00, 6:00, and 9:00 positions. As noted below, the tool was rotated slightly at the start for some of the pulls in order to increase the likelihood that the MWM-Arrays would pass over the flaws. Figure 79 shows the orientation of the encoder wheel at the 12:00 position and the two VWA005 sensor arrays at 9:00 and 3:00 orientations respectively. The view is from the inlet end of the pipeline sections.

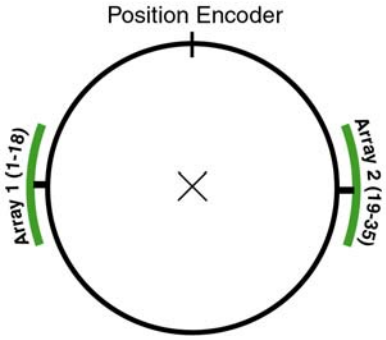

Figure 79. Schematic diagram showing the orientation of the encoder wheel and the two VWA005 MWM-Arrays, looking toward the pipe inlet.

Figure 80 and Figure 81 show composite images obtained for a scan with Array 1 and Array 2, with the position encoder at the 12:00 orientation. MWM-Array 1 (Channels 1 – 18) was at the 9:00 orientation. MWM-Array 2 (Channels 19 – 35) was at the 3:00 orientation. The speed at which the ILI tool was being pulled was approximately 0.36 mph. The B-Scan plots show the effective property (lift-off and permeability) variation for each sense element along the entire length of the scan. The data is plotted against the position encoder value. Chatter in the response at the beginning and end of the scans when the tool was stationary are not plotted. The B-scan plots show the presence of two flaws in Sections 1 and 3 that are near the inlet to each section. The flaws appear as a rapid local change in both the lift-off

and permeability. Away from these flaws, the permeability is relatively constant in each of the sections. The periodic variation in the effective lift-off was caused by a rocking motion associated with the prototype tool or the sensor array fixtures. Ongoing work is aimed at developing filters that remove this type of variation that is the same for all of the elements in the array. Note also that this rocking motion was less noticeable for other tool orientations, which suggests that the rocking motion will be less significant when sensor arrays are mounted around the entire circumference of the tool.

As shown in Figure 80, two flaws were detected by Array 1 in Section 1 and Section 3 of the pipe section. These flaws have a slot geometry and appear as changes in both effective properties. The spacing between the slots is approximately 8-in. The slots are 0.75-in. wide and 2-in. long; since the sense elements only span 4.0-in. for either of the MWM-Arrays, the entire shape can only be captured when the arrays are centered over the flaw. As shown in Figure 81, two flaws were detected by Array 2 in Section 1 and Section 3 of the pipe section. In this case, the flaws appear as circular changes in the effective properties. The spacing between the flaws is approximately 6-in. and the orientation is not the same for each flaw within a pair; **this is consistent with information that is known about the flaws**. In both sections the pairs of flaws are located 24-in. from the inlet of each section. For section 1 the measured distance is slightly smaller probably because the array was positioned slightly inside the pipe section at the start of the measurements. For section 3, the measured distance is about 25-in. from the joint.

Figure 82 and Figure 83 show composite images obtained for a scan with the exact same orientation for Array 1, Array 2 and the position encoder as in Figure 80 and Figure 81. However, these scans were performed with faster pull speeds (approximately 0.72 mph). These results are encouraging because the faster pull speed did not diminish the image resolution. Again, due to the limited span of the MWM-Arrays, the entire image of the flaws were only obtained when the MWM-Arrays were centered over the flaws; this limitation would be removed by using multiple MWM-Arrays that span the entire circumference of the pipe.

Figure 84 and Figure 85 show composite images obtained for a scan with slightly different orientation for Array 1, Array 2 and the position encoder as previously illustrated in Figure 80 – Figure 83, but at a faster scan speed. The position encoder was at the 12:30 orientation so that Array 1 (Channels 1 – 18) was at the 9:30 orientation and Array 2 (Channels 19 – 35) was at the 3:30 orientation. The tool pull speed was approximately 1.08 mph. The effect of the increased speed (three times that of Pull 2) is evident in the B-Scan plots and the C-Scan images – the tool experienced increased rocking motion during the pull. This rocking motion can be observed clearly in the responses of Section 1 and Section 3. For this slightly shifted orientation, better images of the entire flaw were obtained with Array 1 for the flaws in Sections 1 and Section 3. For this array the slot geometry is clearly visible. However, for Array 2, the two circular flaws appear near the bottom of the image and there is only a partial indication from one of the flaws. Again, it is encouraging that the flaw regions were detected at the higher pull speeds that are more typical of ILI tool operation. This indicates that the instrument data acquisition rates were reasonable for these tests, but to accommodate the greater number of channels required for complete circumferential coverage, higher data acquisition rates will be required. It is also anticipated that the rocking motion will be reduced when more MWM-Arrays are placed around the entire circumference.

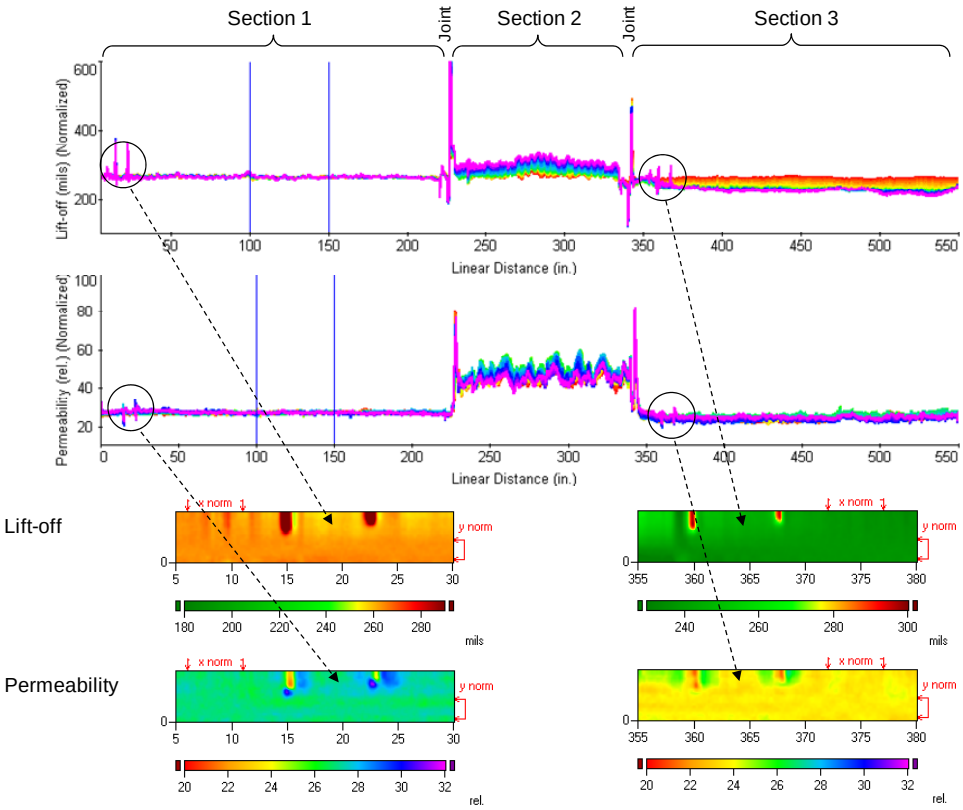

Figure 80. Composite image for Array 1 (Channels 1 – 18) at 9:00 orientation (Pull 2).

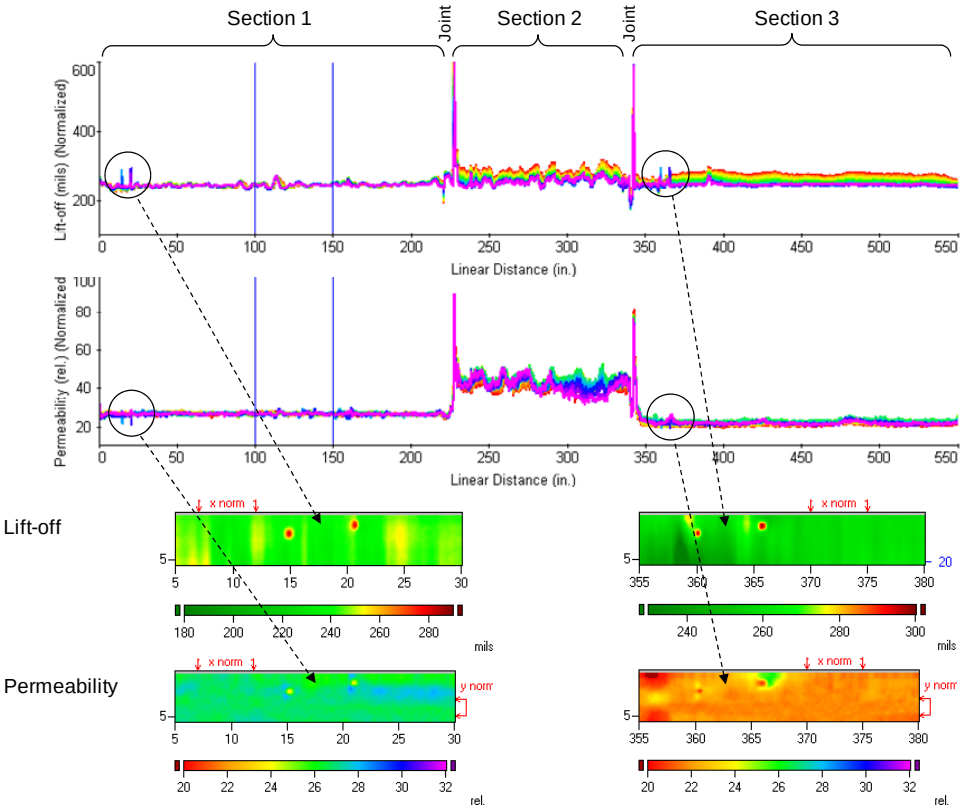

Figure 81. Composite image for Array 2 (Channels 19 – 35) at 3:00 orientation (Pull 2).

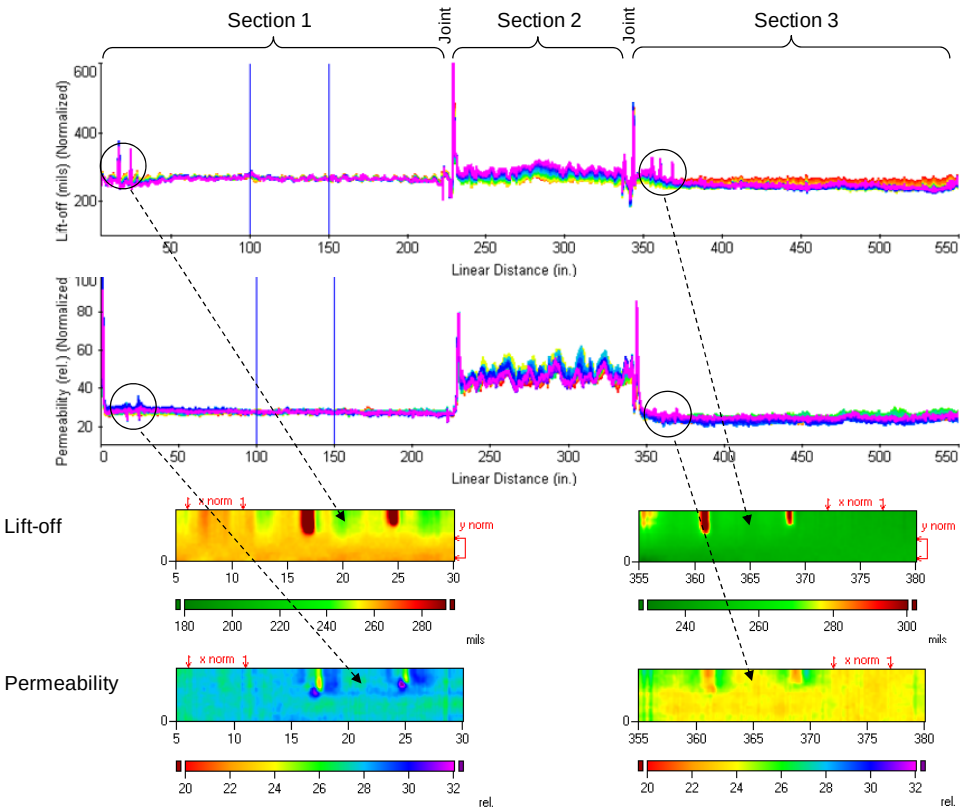

Figure 82. Composite image for Array 1 (Channels 1 – 18) at 9:00 orientation (Pull 11).

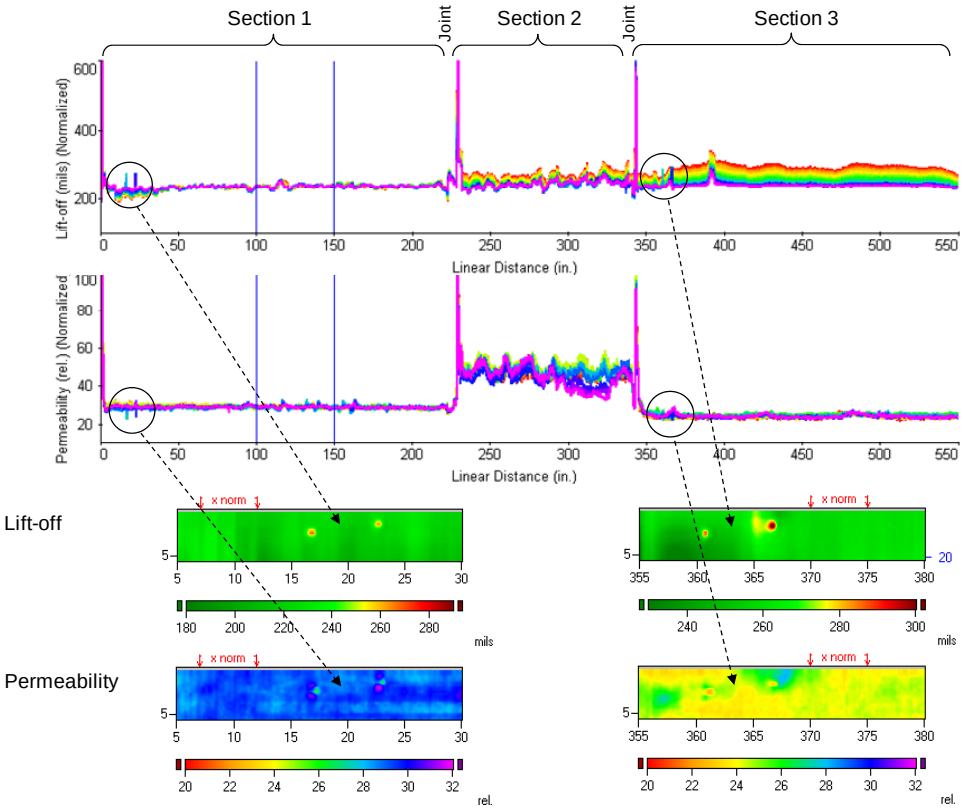

Figure 83. Composite image for Array 2 (Channels 19 – 35) at 3:00 orientation (Pull 11).

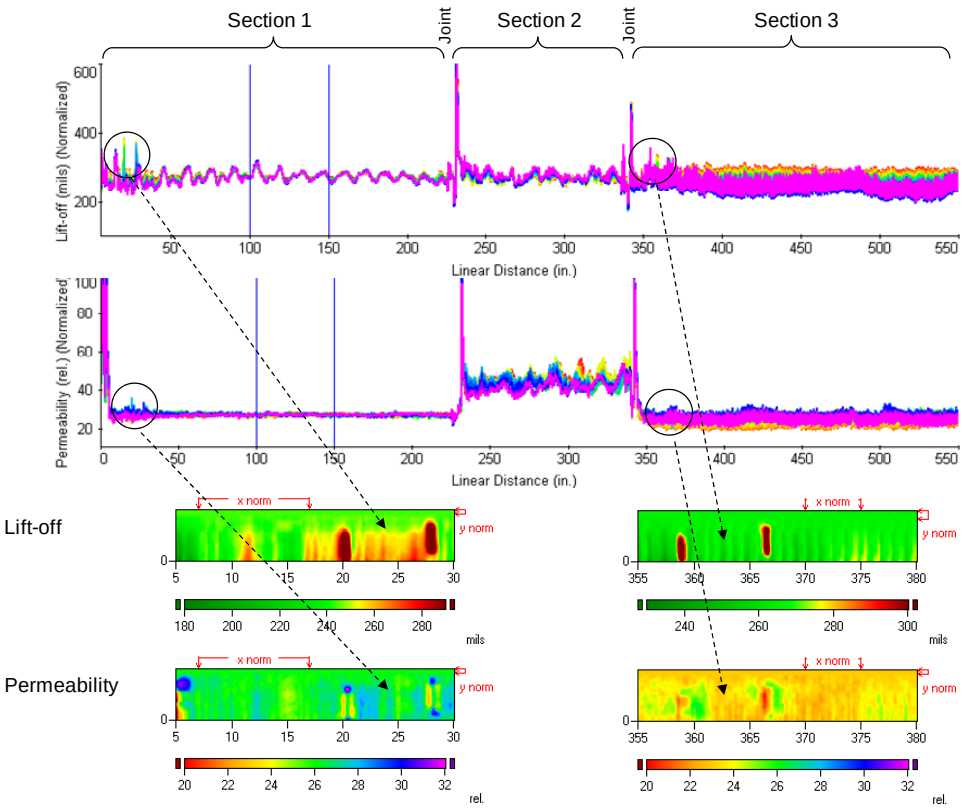

Figure 84. Composite image for Array 1 (Channels 1 – 18) at 9:30 orientation (Pull 12).

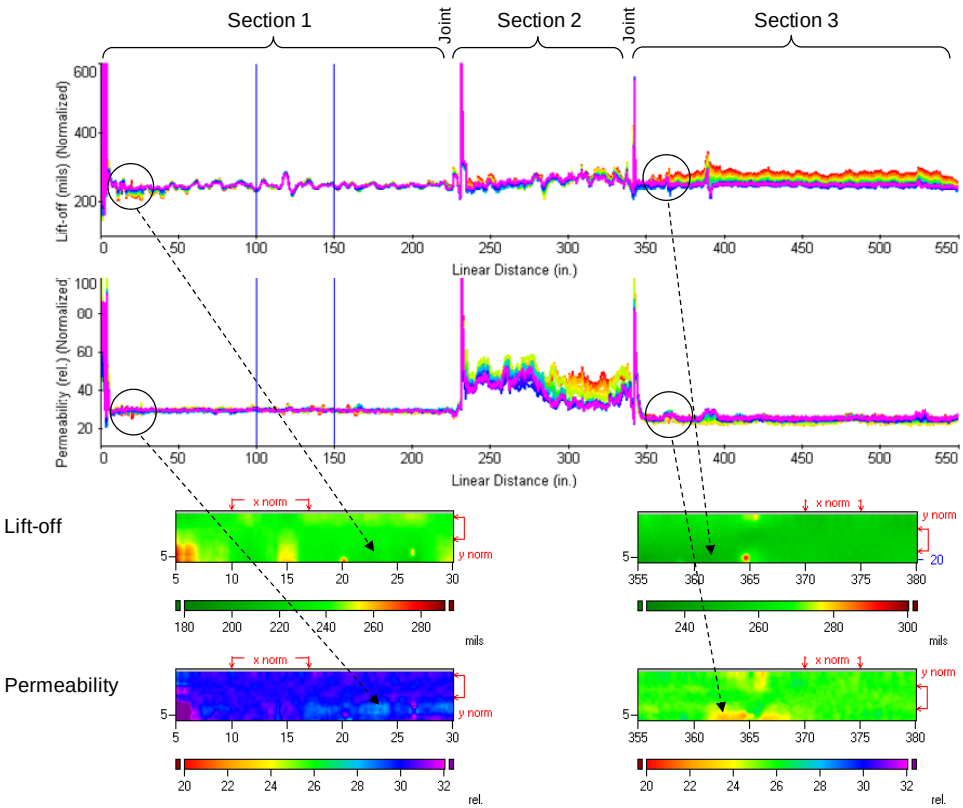

Figure 85. Composite image for Array 2 (Channels 19 – 35) at 3:30 orientation (Pull 12).

Figure 86, Figure 87 and Figure 88 show composite images obtained for a scan with the position encoder at the 10:30 orientation. Array 1 (Channels 1 – 18) was at the 7:30 orientation and Array 2 (Channels 19 – 35) was at the 1:30 orientation. The prototype tool was rotated to this orientation to image the flaws along all three pipe sections, especially in Section 2 which contains a series of internal flaws of increasing size and depth. As shown in Figure 86, Array 1 imaged two circular flaws in both Section 1 and Section 3. As shown in Figure 87, Array 1 also imaged five circular flaws in Section 2. In Section 2, the baseline permeability is larger than in the other sections, consistent with this pipe section being from a different lot of material or possibly a different grade. There is also a substantial spatial variation in the permeability along the pipe surface. This appears to be due to generalized corrosion of this pipe section; it is our understanding that this pipe section had been exposed to the elements for a significant amount of time. The improved stabilization of the tool with the second MWM-Array is also apparent through a comparison to the first pull test results of Figure 75. The B-scans and C-scan images show less lift-off variation after passing through the joint into Section 2; this allows the smallest flaw in section 2 to appear in the second pull test. As shown in Figure 88, Array 2 imaged two circular flaws in both Section 1 and Section 3. The speed at which the tool was being pulled was approximately 0.36 mph.

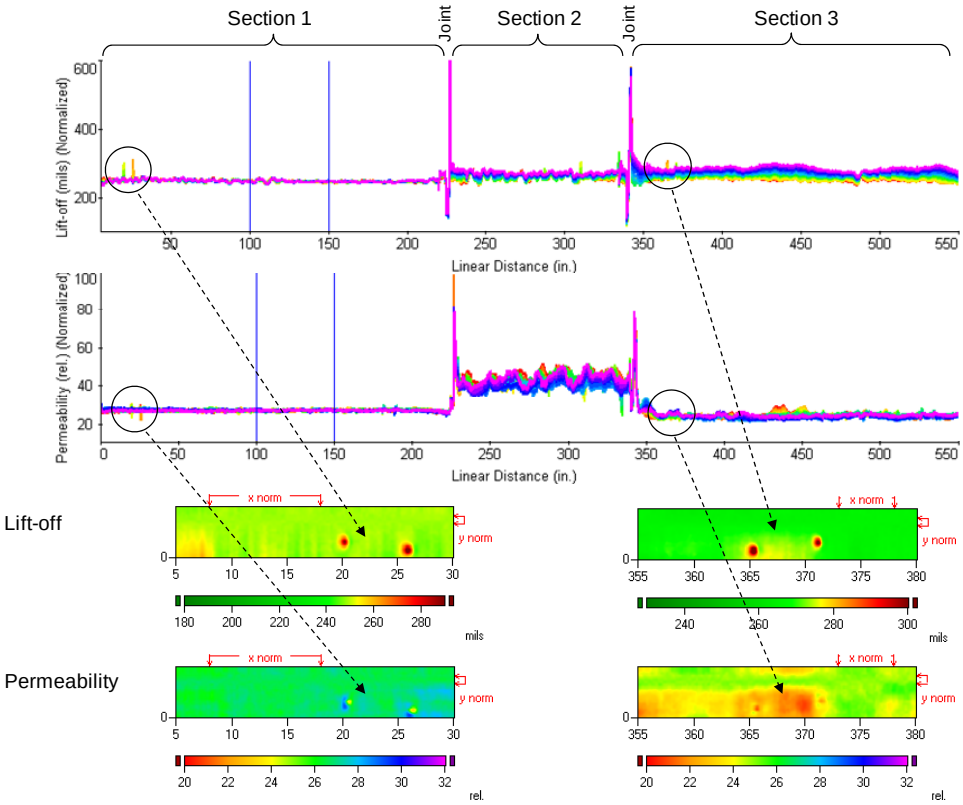

Figure 86. Composite image for Array 1 (Channels 1 – 18) at 7:30 orientation (Pull 4).

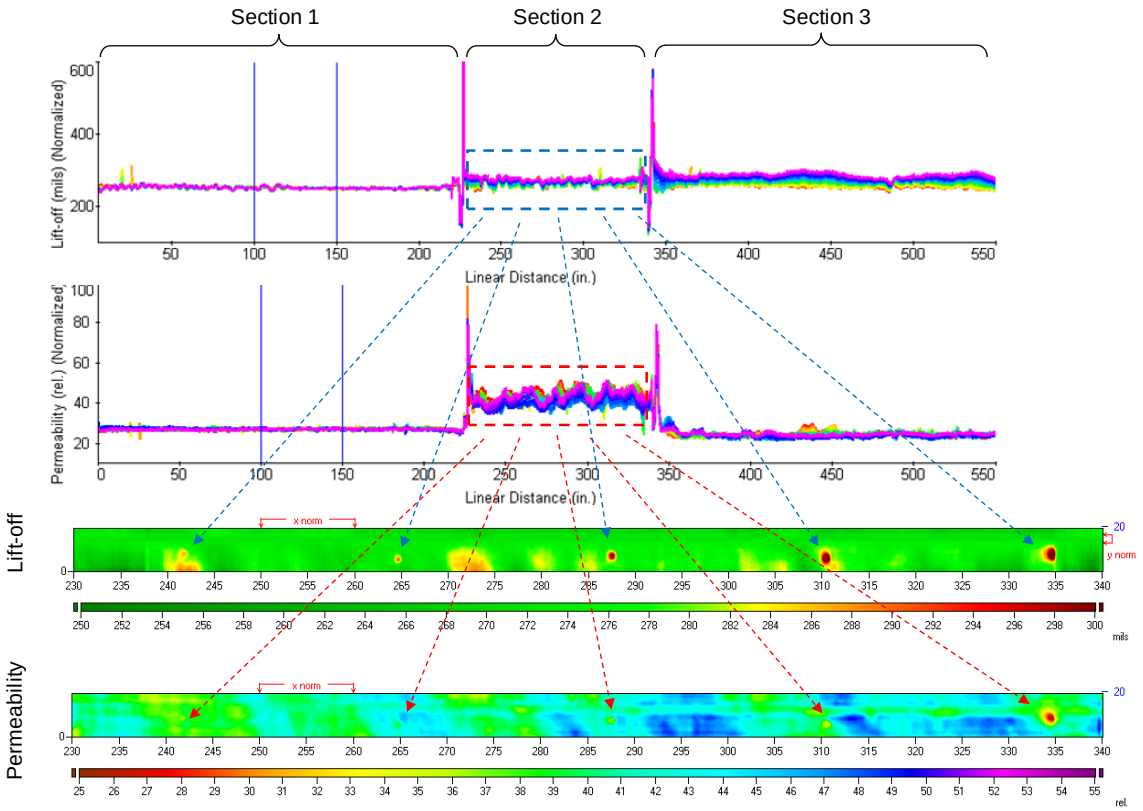

Figure 87. Composite image for Array 1 (Channels 1 – 18) at 7:30 orientation (Pull 4).

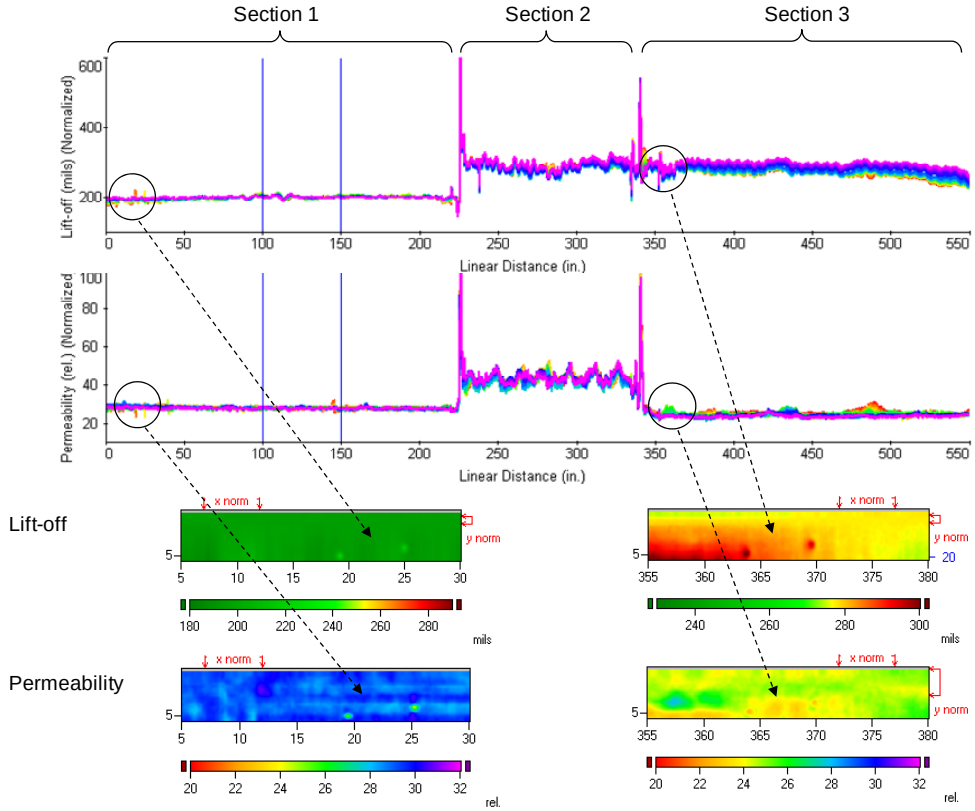

Figure 88. Composite image for Array 2 (Channels 19 – 35) at 1:30 orientation (Pull 4).

Figure 89, Figure 90, and Figure 91 show composite images obtained for a scan with the exact same orientation for Array 1, Array 2 and the position encoder as in Figure 86 through Figure 88. However, these scans were performed with faster pull speeds at approximately 0.72 mph. The measurement data was relatively clean, but the relatively low flaws in Section 1 and Section 3 (which are apparent in Figure 86 and Figure 88) were very low or did not appear in this scan (Figure 89 and Figure 91). This difference was attributed to a slight rotation of the tool during the insertion of the tool into the pipe and during the scan; although the tool was initially placed at a 10:30 orientation, the encoder was observed at the 9:30 orientation at the completion of this pull. Although the arrays were slightly misaligned, the images show that several of the flaws were detected even at the higher scan speeds.

The orientation issue was resolved by slightly rotating the tool so that the encoder position was at 9:30, with Array 1 at the 6:30 orientation and Array 2 at the 12:30 orientation. Another pull, albeit at an even higher scan speed of approximately 1.08 mph, yielded better flaw images. As can be seen in Figure 92, Array 1 was able to obtain a complete scan of the two flaws in Section 1 and Section 3. Array 1 was also able to image the five circular flaws in Section 2, as shown in Figure 93. Figure 94 shows the two flaws imaged by Array 2 in Section 1 and Section 3. Although the increased speed of the pull created a rocking motion of the ILI tool, the flaws are still evident. The rocking motion was most evident for Array 2 when passing through Section 2 and Section 3, as shown in the lift-off B-Scan plot of Figure 94.

An instrumentation parameter than can be varied to affect the data acquisition rate is the integration time. This is the time over which the acquired data is averaged for each measurement. A longer integration time leads to less measurement noise at the expense of a slower data acquisition rate. Here, the same orientation and pull speed of Figure 92 through Figure 94 were used, except the integration time was reduced by a factor of 3. The measurement results are shown in the composite images of Figure 95, Figure 96, and Figure 97. When compared to Figure 92 through Figure 94 there is no degradation in image resolution, which indicates that reducing the integration time is an option to increase the data rate.

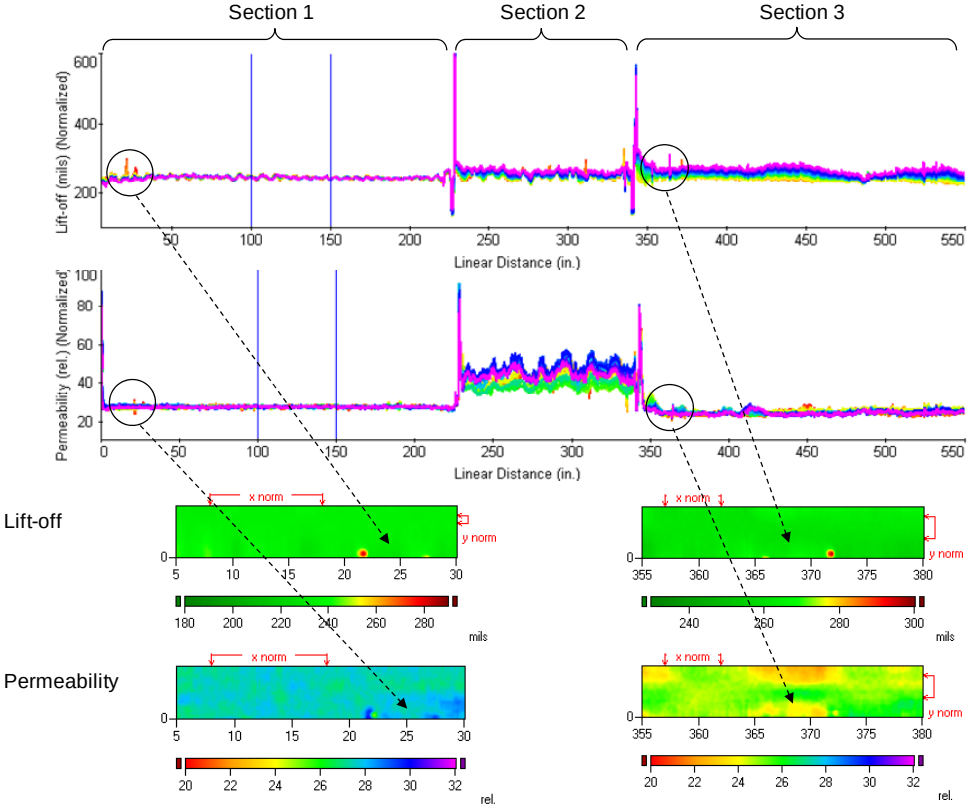

Figure 89. Composite image for Array 1 (Channels 1 – 18) at 7:30 orientation (Pull 10).

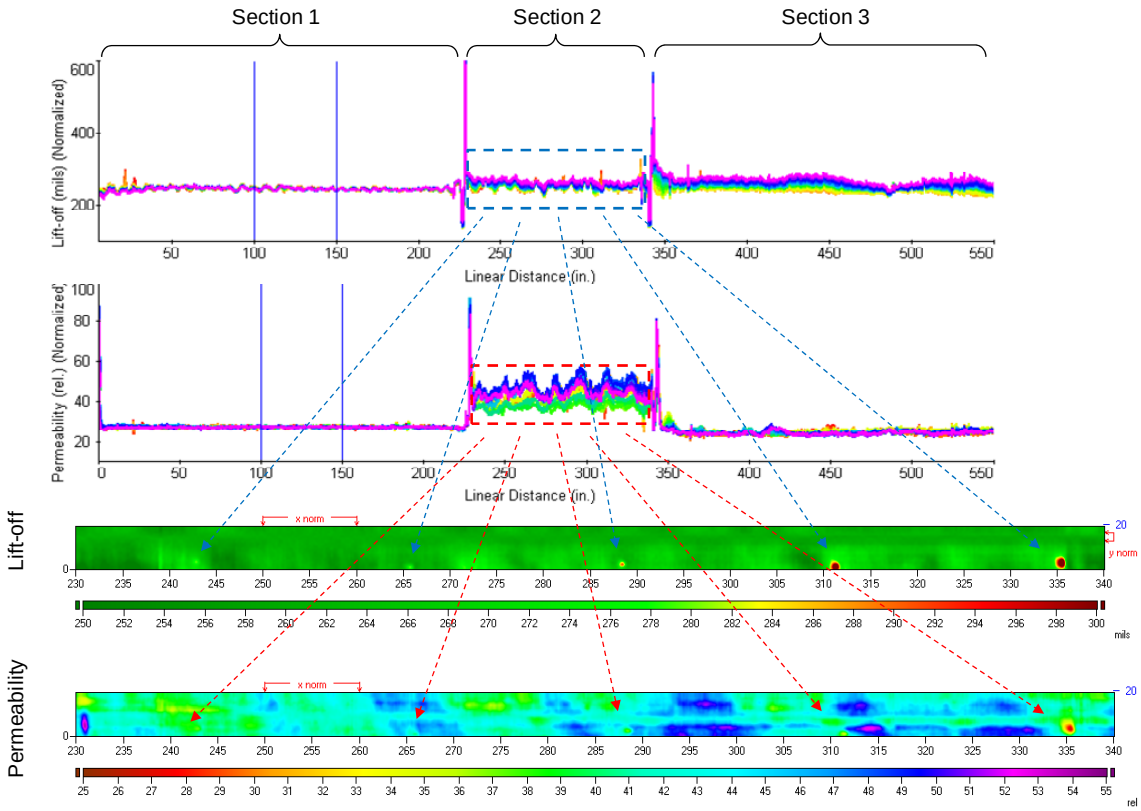

Figure 90. Composite image for Array 1 (Channels 1 – 18) at 7:30 orientation (Pull 10).

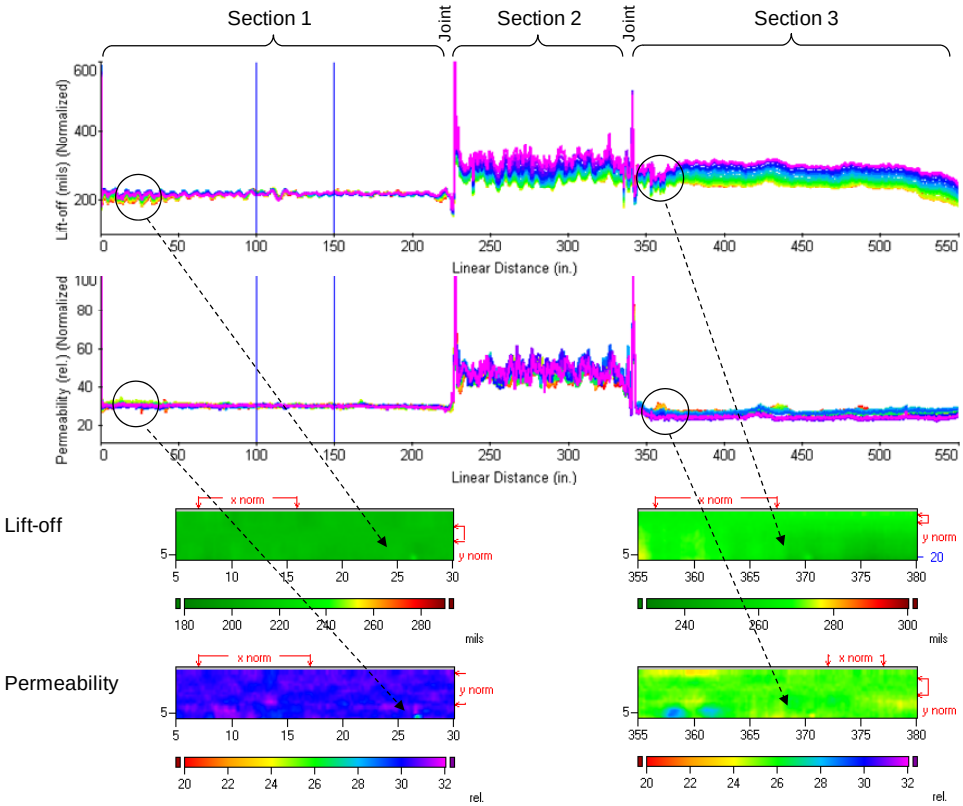

Figure 91. Composite image for Array 2 (Channels 19 – 35) at 1:30 orientation (Pull 10).

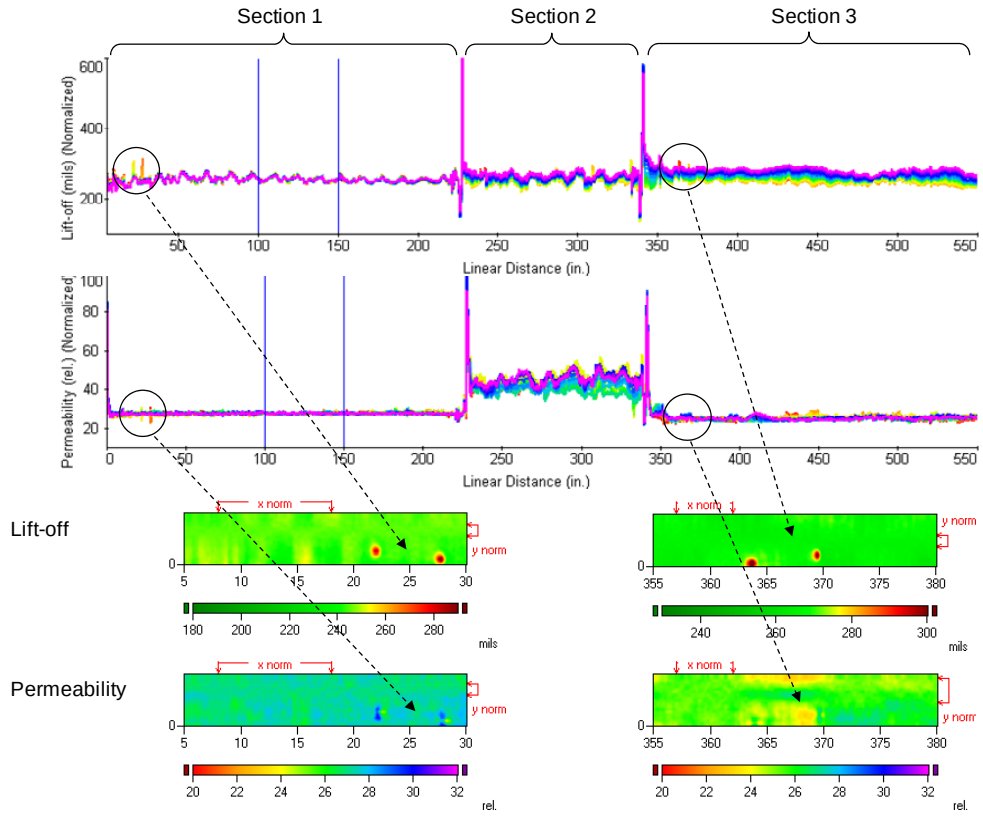

Figure 92. Composite image for Array 1 (Channels 1 – 18) at 6:30 orientation (Pull 13).

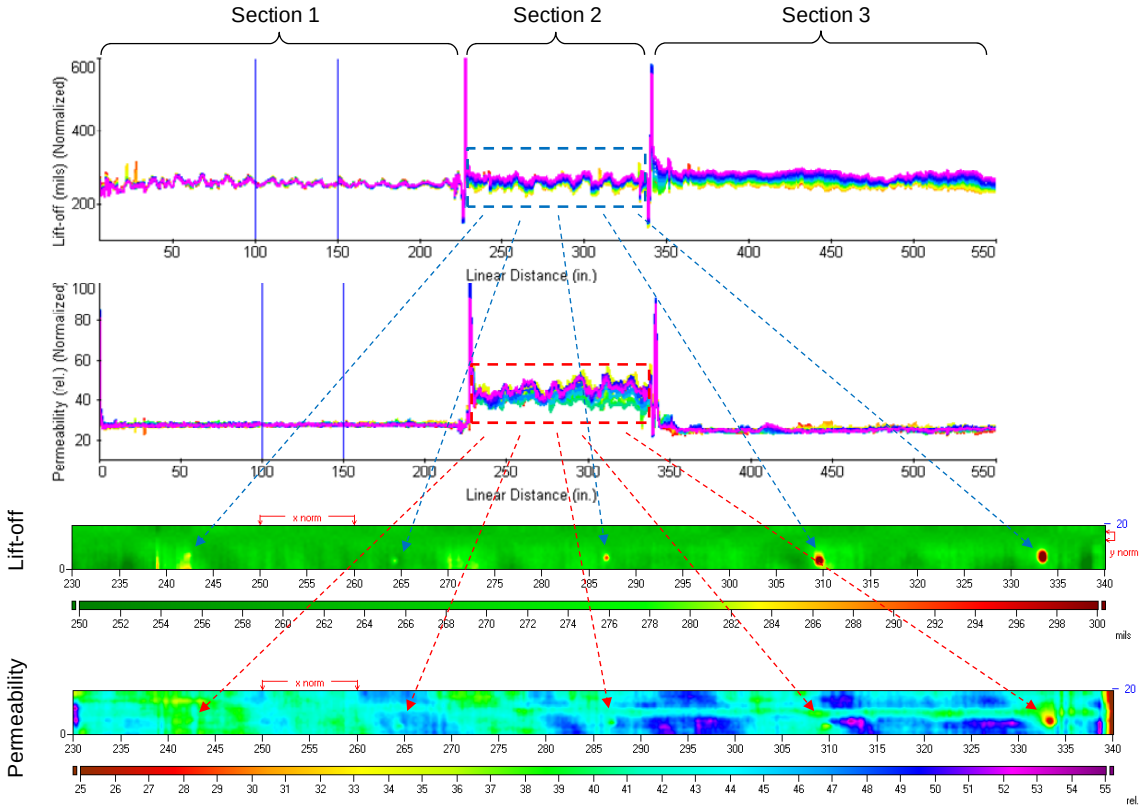

Figure 93. Composite image for Array 1 (Channels 1 – 18) at 6:30 orientation (Pull 13).

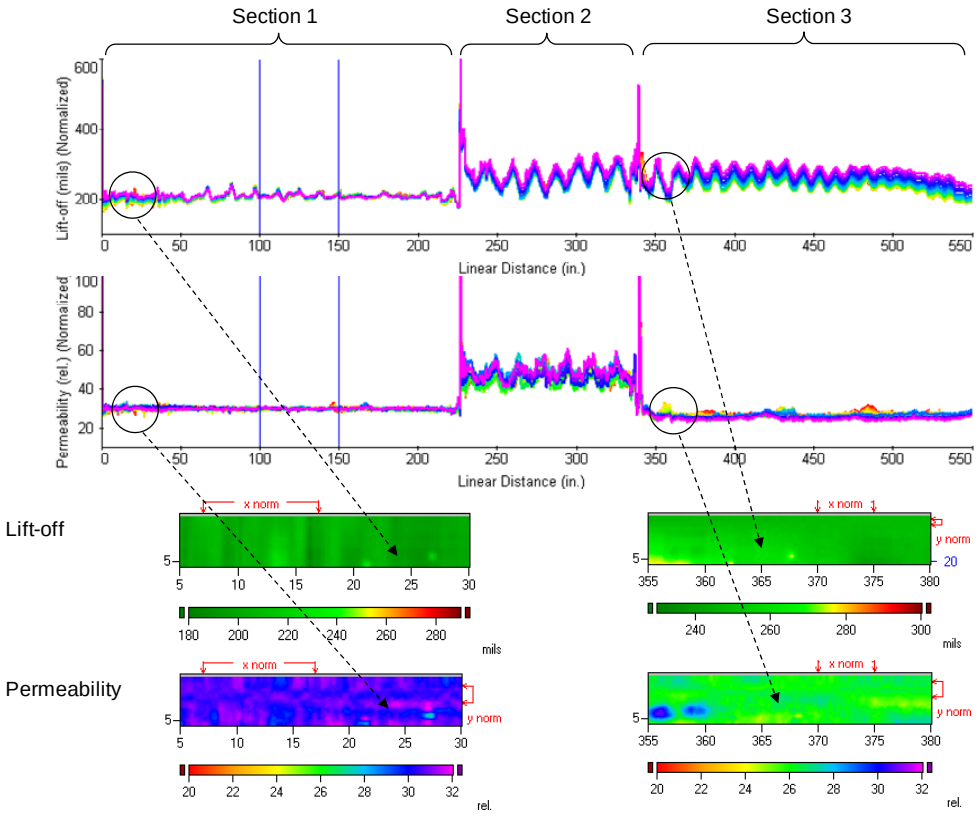

Figure 94. Composite image for Array 2 (Channels 19 – 35) at 12:30 orientation (Pull 13).

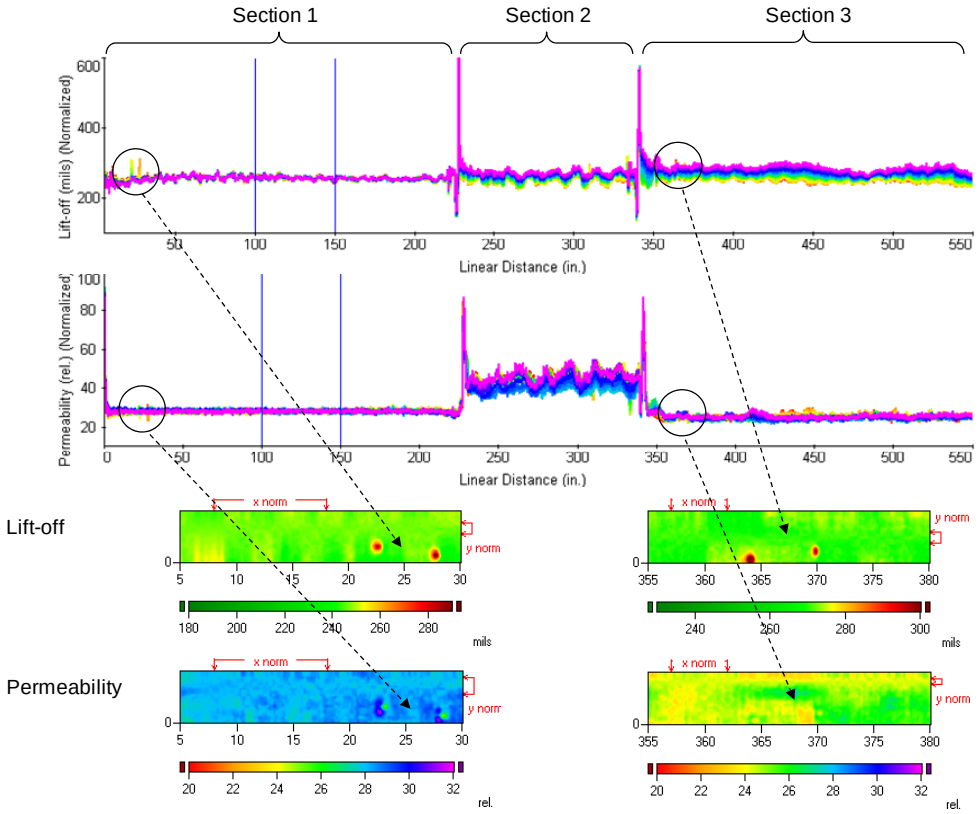

Figure 95. Composite image for Array 1 (Channels 1 – 18) at 6:30 orientation (Pull 14).

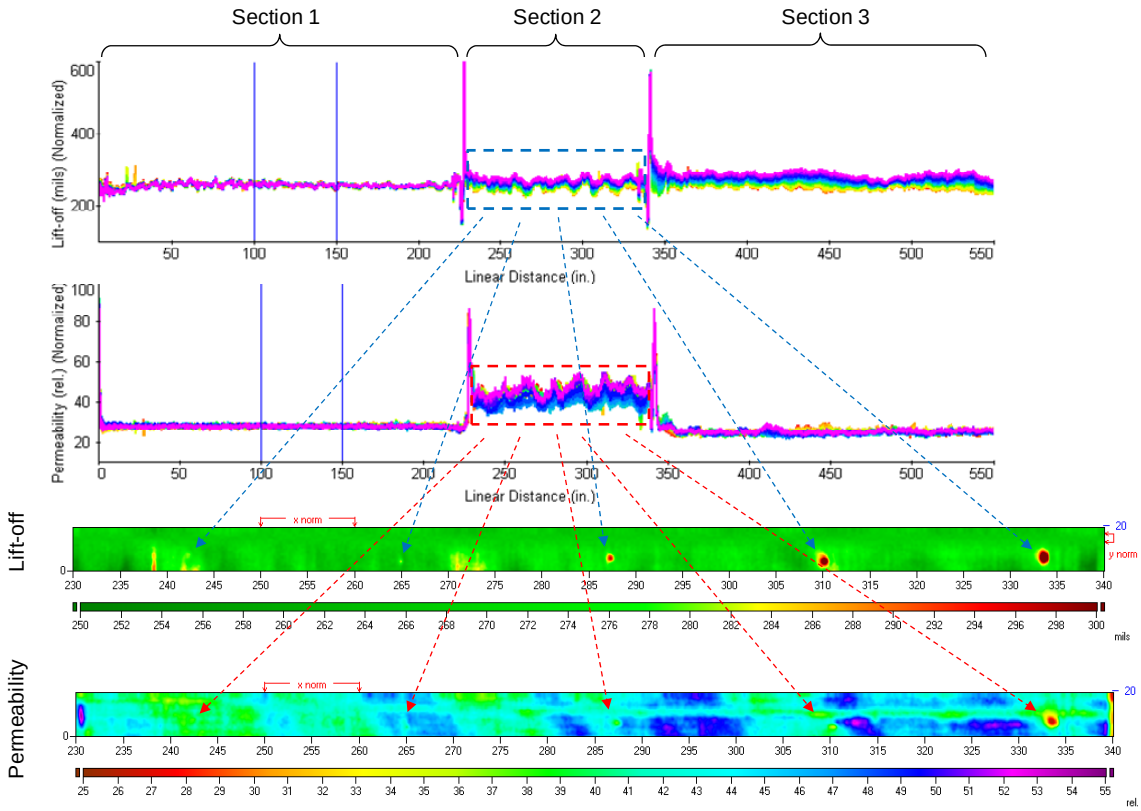

Figure 96. Composite image for Array 1 (Channels 1 – 18) at 6:30 orientation (Pull 14).

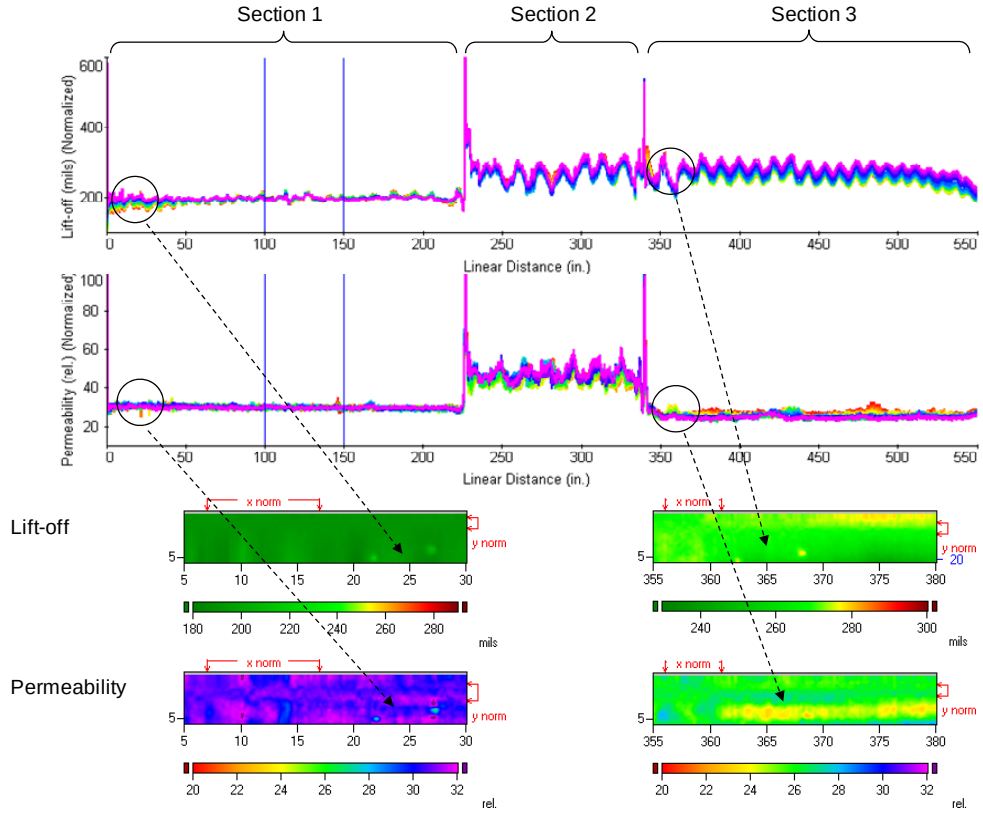

Figure 97. Composite image for Array 2 (Channels 19 – 35) at 12:30 orientation (Pull 14).

Table 4 provides a list of the internal flaws on each of the pipe sections, along with the actual and measured flaw dimensions. The flaws were fabricated with ball mills of different dimensions to create the specified flaw size and depth. The measured diameter is obtained from the C-scan images as the average length and width of the color change from green to yellow; future work should redo this calculation by calculating the full width at half maximum value as this provides a better measure of the flaw dimensions. The measured depth is the change in the lift-off response and is taken as the difference between the peak value and an average value near the flaw; future work should correct this value to account for the flaw shape on the response. This should bring the measured and actual flaw dimensions into better agreement.

Table 4. List of internal flaws and properties on the pipe sections from pull test 2.

Section	**ID**	**No.**	**Measured –Array 1**		**Measured – Array 2**		**Pull No.**
			Dia. (in.)	Depth (mils)	Dia. (in.)	Depth (mils)	
1	AA	1	-	-	0.4	31.3	4
		2	-	-	0.5	27.1	4
	BB	1	-	-	0.5	47.9	2
		2	-	-	0.3	52.9	2
	CC	1	0.6	50.1	-	-	4
		2	0.5	59.8	-	-	4
	Z	1	Slot	111.7	-	-	2
		2	Slot	91.4	-	-	2
2	A	-	0.5	13.6	-	-	4
	B	-	0.5	14.3	-	-	4
	C	-	0.7	25.3	-	-	4
	D	-	0.9	41.3	-	-	4
	E	-	1.0	70.5	-	-	4
3	AA	1	-	-	0.5	41.6	4
		2	-	-	0.7	13.8	4
	BB	1	-	-	0.3	42.2	2
		2	-	-	0.4	44.6	2
	CC	1	0.5	44.8	-	-	4
		2	0.7	57.2	-	-	4
	Z	1	Slot	56.3	-	-	2
		2	Slot	57.1	-	-	2

6.4.3 Hybrid MFL and MWM-Array methods

Part of this program was devoted to investigating adapting our experience with segmented field MWM-Arrays to MFL sensing technology. The goal was to determine if the techniques could be applied to, or used in conjunction with, MFL methods. This began with a review comparing typical features of MFL and MWM techniques. This then led to detailed investigation of applications where MWM approaches could enhance MFL operation. The results of this investigation are described here.

6.4.3.1 MFL and MWM Feature Comparison

As part of the effort to better understand the capabilities of the MWM-Arrays with respect to existing technologies, a comparison between MFL and MWM capabilities was developed. A useful reference for this review was a DOT Final Report on Mechanical Damage [10].

MFL is a widely used tool in ILI applications for detection and identification of metal loss with a developing application for mechanical damage. The MFL signal depends primarily upon metal loss, but also upon the steel magnetic properties, including stress and strain, tool speed, sensor orientation, and lift-off. The tools typically have multiple sensors and, at least in the context of geometry tools, such as ultrasonic tools, high spatial resolution tools have sense elements spaced less than one inch apart around the circumference. The most common MFL tools use axial fields, with the applied magnetic field oriented along the length of the pipe; this makes the tools most sensitive to circumferential metal loss compared to axial metal loss and provides some sensitivity to circumferential cracks. Some tools use circumferential fields and others incorporate tri-axial sense elements that allow measurements in three field orientations simultaneously. Each tool configuration may detect dents from mechanical damage and also the anomalies or metallurgical differences at welds.

Performance specifications for detection and identification of damage varies with the type of MFL tool. For axial MFL, a typical specification is +/-10% of the wall thickness with 80% certainty and the sizing accuracy decreases for some types of damage, such as pitting. For circumferential MFL, the ability to characterize metal loss is less accurate than with axial MFL and a typical specification is +/-20% of the wall thickness with 80% certainty.

A common configuration for an MFL tool uses a strong permanent magnet to magnetically saturate the steel and a Hall Effect device to sense the magnetic field. This configuration allows the tool to be sensitive to local flaw regions but relatively insensitive to widespread, gradual property changes. In addition, close contact is required between the magnet and steel wall, which makes them unsuitable for inspection through coatings and liners. It is our understanding that, in practice, the tools are typically calibrated by using information from areas of likely high damage after scans are performed.

In comparison, the model-based MWM-Arrays use a time-varying magnetic field to inspect the steel wall and can accommodate coatings and insulation. Multiple sense elements are used to create high spatial resolution images, with an example sense element spacing of 0.25-in. for the VWA001. The use of models allows simplified calibration requirements, using, for example, reference measurements in air or on a component, with and without a shim and also provides local and general material loss information. However, since the excitation is a drive coil, the MWM-Arrays have higher power requirements and the low excitation frequencies required for penetration through thick steel walls can limit the data acquisition rate.

Given these tradeoffs between the two types of tools, three hybrid MFL/MWM configurations have been identified. The first is to modify the MFL design to have two or more sense elements to sense different components or segments of the magnetic field. This segmented field design would take advantage of JENTEK's model-based multivariate inverse methods and provide a means for measuring the lift-off along with the steel wall properties such as permeability and thickness. The second is to integrate an MWM-Array and MFL sensor together and use the capabilities of each. For example, high

frequency information from the MWM-Array could be used to measure lift-off, permeability, and near-surface material loss while the MFL sensor would provide total wall thickness (and hence far surface material loss). The third is to use a permanent magnet to saturate the steel in the vicinity of the MWM-Array so that the high frequency inspection field from the MWM-Array to penetrate further into the steel. Since all of these require the use of a bias magnetic field, the ability to inspect through thick coatings and/or insulation is limited. However, there is the potential for improving the performance compared to the use of MFL alone for situations where the lift-off from the steel wall surface is not too large.

6.4.3.2 Hybrid MFL/MWM Investigation

Several simulations were performed to investigate application of the MWM technology to enhance MFL operation. As a starting point, one set of simulations used a two-dimensional model geometry for an MFL sensor, as shown in Figure 98, to determine magnetic flux variations with material loss location and size. In these simulations, a permanent magnet is placed between two steel core sections and placed near a 12.7 mm (0.5-in.) thick steel test material. The permanent magnet is 100 mm long and 20 mm thick while the core sections (constant relative permeability of 40) are 50 mm long and 50 mm thick. The horizontal (H_x) and vertical (H_y) components of the magnetic field were obtained at the center of the device 3 mm below the surface of the test material.

Figure 99 shows the field variation with flaw position and depth for several near-surface flaws. The horizontal component of the magnetic field shows a primary peak when the flaw is over the sense element; for the wider flaws there are secondary peaks as the edge passes over the sense element. The vertical component of the magnetic field begins to change when the flaw is present within the magnetic circuit between the core legs of the sensor, but the largest signals occur when the edges of the flaw pass over the sense element. For both orientations, the width of the main response (e.g., the primary peak for the horizontal component and the distance between the maximum and minimum responses for the vertical component) correspond to the width of the flaws. Similar behavior is observed for a far-surface flaw. Figure 100 shows the simulation geometry and Figure 101 shows the corresponding plots of the sense element magnetic field responses for several flaw conditions.

One approach for adapting the MWM techniques to MFL methodologies is to use measurement grid methods to assess the flaw condition. To illustrate this approach, key parameters from the simulation scans of Figure 99 and Figure 101 were plotted against the flaw conditions. For the vertical component of the magnetic field, the peak-peak difference was used while for the horizontal component of the magnetic field, the field intensity at the center of the flaw (which is also the location of the vertical component crossing through zero) was used. As shown in Figure 102, the grids are relatively open, which indicates greater sensitivity, for localized and deeper material loss; for shallow material loss and, to a lesser extent for material loss that is spread over a larger area, there is a reduction in sensitivity. However, using the responses from both measurement orientations should be able to readily provide information about the nominal extent and depth of the material loss. Of course other information from the scans could also be used to help determine the extent of damage, such as the distance between maximum and minimum for the vertical component. Note also the strong similarity in the measurement grids for near and far-surface material loss. This suggests that using MFL measurements from a single location would have difficulty assessing the damage side. This is where the combination of an MWM-Array and MFL sensor would have advantages; using high frequency information from the MWM-Array could provide lift-off, permeability, and near-surface material loss while the MFL sensor would provide total wall thickness (and hence far surface material loss).

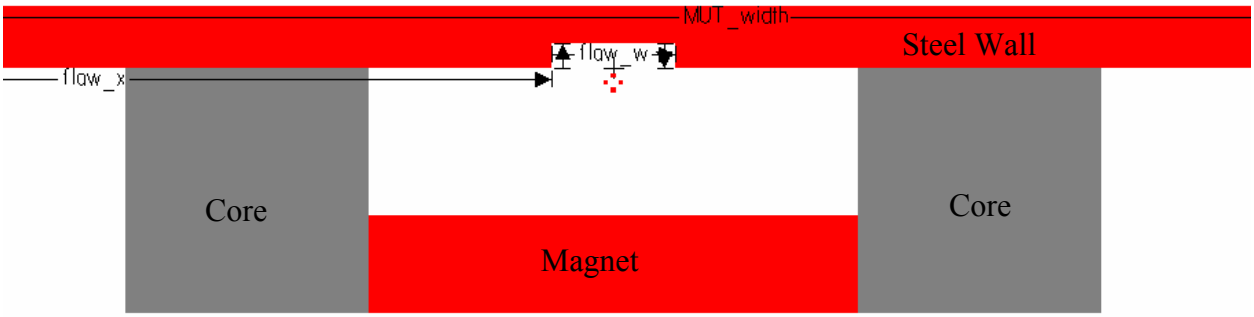

Figure 98. Two-dimensional simulation geometry for a basic MFL sensor with permanent magnet and magnetic flux sensor elements for near-surface material loss.

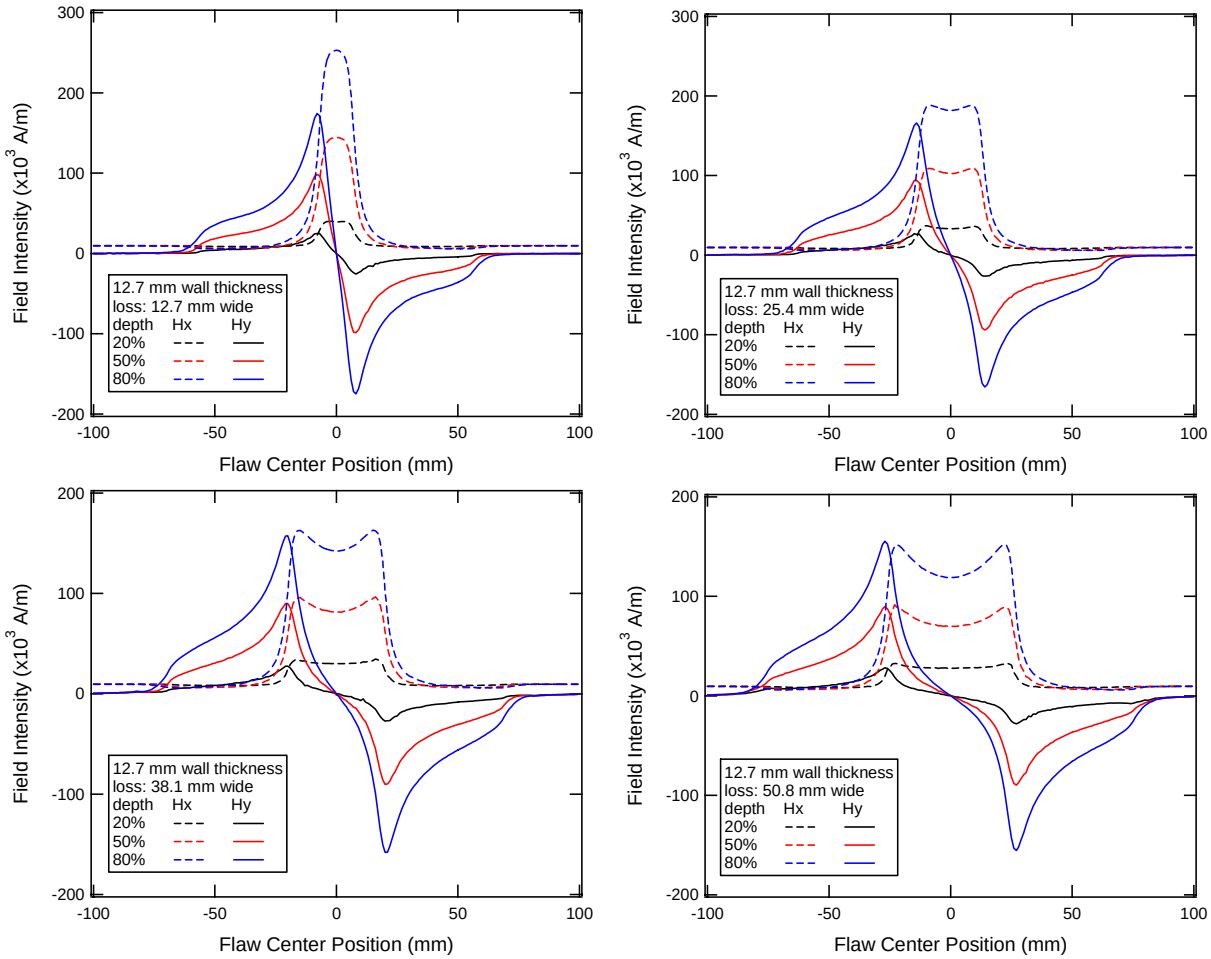

Figure 99. Center field variation with near-surface flaw position and depth for a magnetizable steel test material. The flaws widths are: (Upper Left) 12.7 mm (0.5-in.); (Upper Right) 25.4 mm (1.0-in.); (Lower Left) 38.1 mm (1.5-in.); (Lower Right) 50.8 mm (2.0-in.).

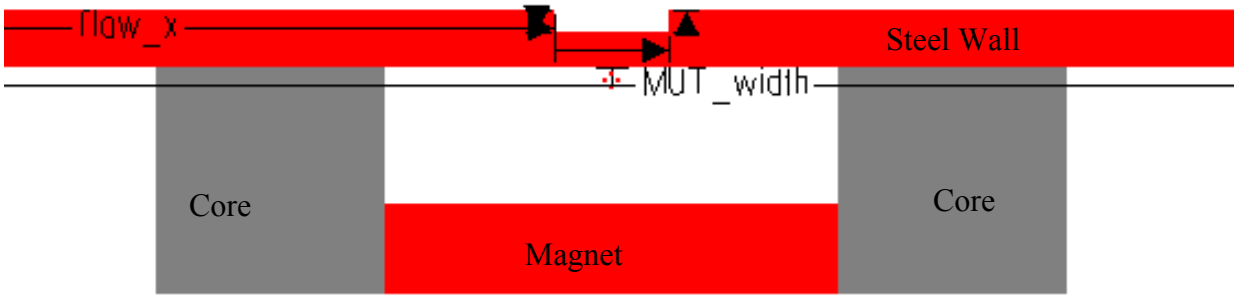

Figure 100. Two-dimensional simulation geometry for a basic MFL sensor with permanent magnet and magnetic flux sensor elements for far-surface material loss.

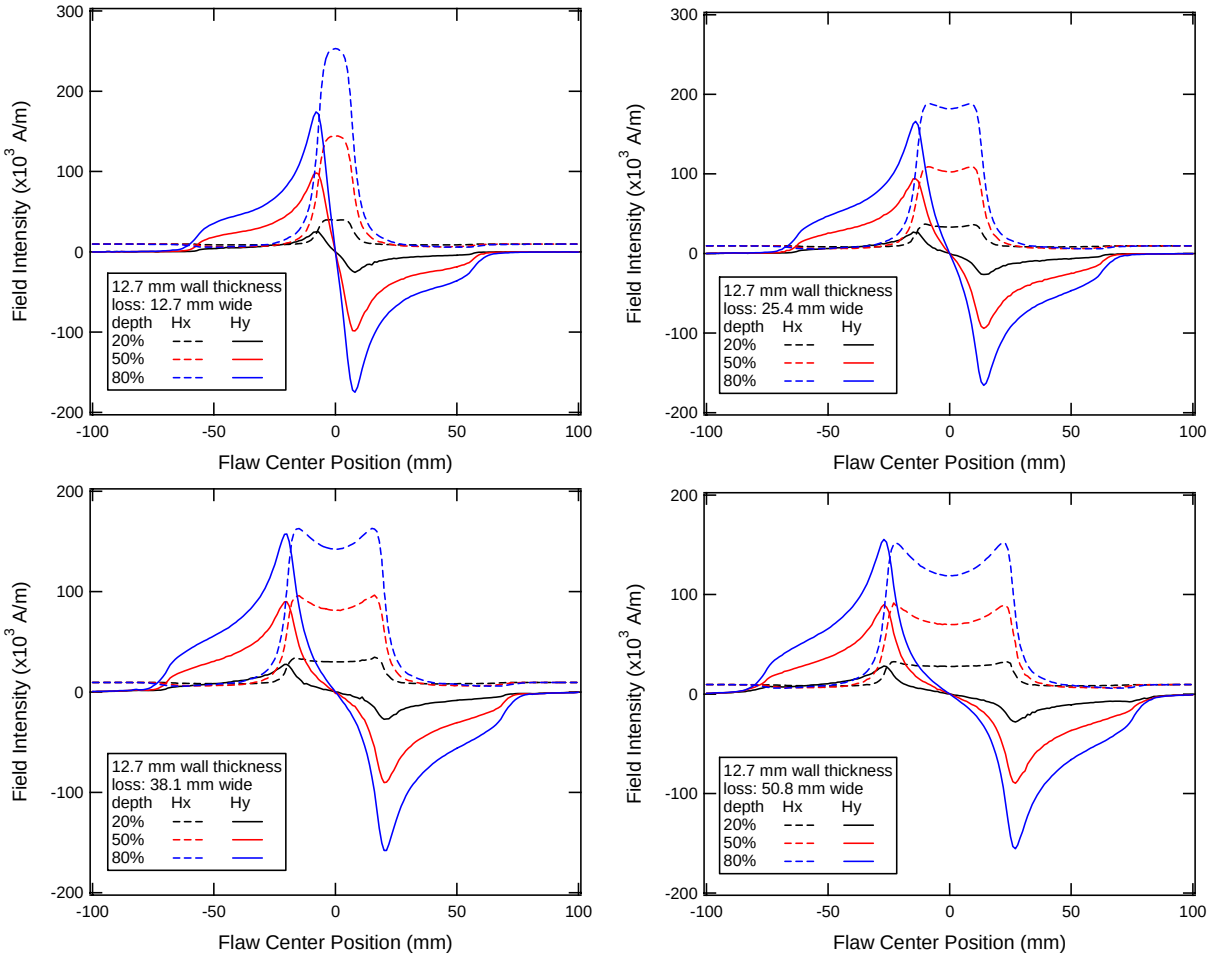

Figure 101. Center field variation with far-surface flaw position and depth for a magnetizable steel test material. The flaws widths are: (Upper Left) 12.7 mm (0.5-in.); (Upper Right) 25.4 mm (1.0-in.); (Lower Left) 38.1 mm (1.5-in.); (Lower Right) 50.8 mm (2.0-in.).

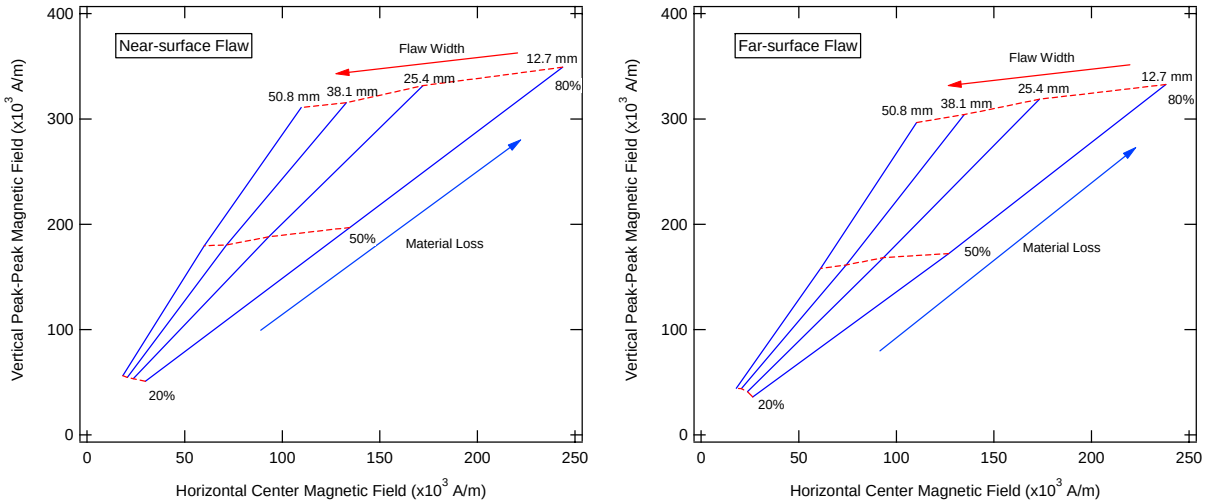

Figure 102. MFL measurement grids with the peak-peak difference in the vertical component of the magnetic field plotted against the horizontal component of the magnetic when the flaw is centered over the sense element for near-surface (left) and far-surface (right) material loss.

A second approach for adapting MWM techniques to MFL methods is to recognize that the sensor can be designed to respond to different components of the magnetic field that penetrate to different depths into the test material. For the MWM-Arrays this segmented field approach permits measurements of material properties in different layers without varying the excitation frequency, which is especially important for dispersive materials that have frequency dependent effective material properties. This permits spatial profiling of materials and separation of near-surface and deeper flaw responses. Figure 103 shows an illustration of a concept for this design as extended to an MFL approach. The different sense elements (e.g., Hall effect detectors – H.D.) are located to provide sensitivity to different components of the sensing field. For MFL, the magnetic flux lines already pass through the thickness of the test material, but the sensor design can be adjusted to enhance discrimination between near-surface and far surface flaws. Measurement grid methods can be used with this type of design.

For these simulations, the simplified sensor design of Figure 104 was used. The same test material and permanent magnetic were used. However, the right core leg was split into a 5 mm wide section and a 15 mm wide section with a 35 mm gap between the core legs. An "extra" sense element was then placed midway between the core legs. The horizontal components of the magnetic field were obtained for both the "nominal" and "extra" sense elements 3 mm below the surface of the test material. Figure 105 shows a plot of the magnetic flux lines. In the vicinity of the "extra" sense element the magnetic field does not remain at a deeper distance in the test material, but it spreads to span the entire thickness; although this was not the aim of the segmented field approach, the weaker field should lead to less sensitivity to material loss on the far surface.

Plots of the field variation with flaw position and size are shown in Figure 106 for near-surface material loss and Figure 107 for far-surface material loss. As expected, the "nominal" field response is essentially the same as the horizontal field results of Figure 99 and Figure 101 since the geometries are similar. However, the "extra" sense element shows greater sensitivity to the near-surface flaw compared to the far-surface flaw, at least for lower material losses (20% and 50%). This appears to be consistent with the flux being weaker in the vicinity of the "extra" sense element. Figure 108 shows the corresponding measurement grids using the field information from both sense element positions. This highlights the separation of the near and far surface damage for the lower material losses. Note that only the 12.7 and 25.4 mm wide flaw conditions are plotted.

Thus, these measurement grids show that using a split core design, or possibly complementary MFL sensor structures, can provide additional information about the flaw properties, such as the wall side that has the damage. It is more effective at separating the flaw sides for shallow and medium depth material loss, but that was simply for this initial test case. Additional work is required to explore the sensitivity of this approach to the various design options, such as the dimensions of the split core legs, the gap between the split core legs, the different components of the magnetic flux being measured, and the thickness of the test material.

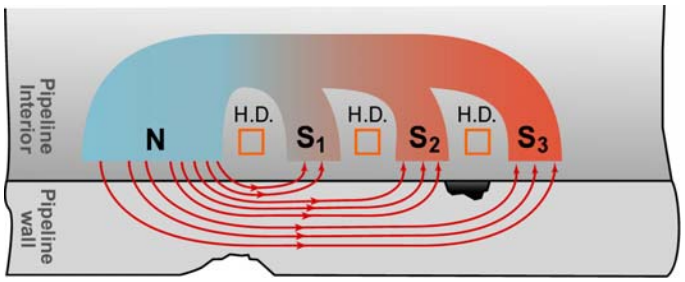

Figure 103. Illustration of the concept for segment field or modified MFL design.

Figure 104. Two-dimensional simulation geometry for a split-core MFL sensor with permanent magnet and magnetic flux sensor elements placed near the surface at the center of each core section.

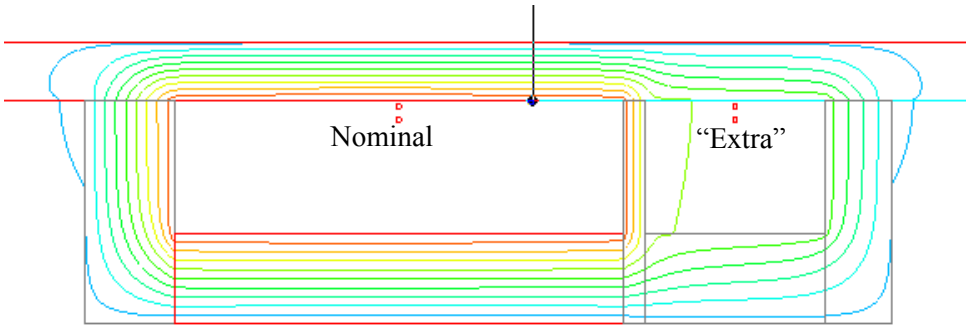

Figure 105. Magnetic flux lines corresponding to the sensor geometry of Figure 104. Both sense elements are indicated as well

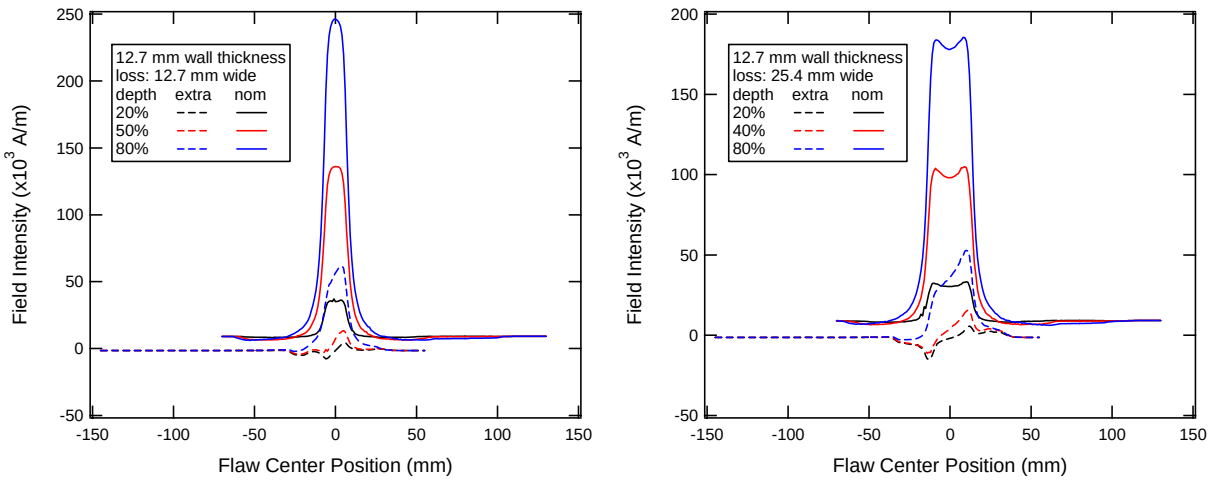

*Figure 106. Horizontal field variation with **near**-surface flaw position and depth for a magnetizable steel test material. The flaws widths are: (Left) 12.7 mm (0.5-in.); (Right) 25.4 mm (1.0-in.).*

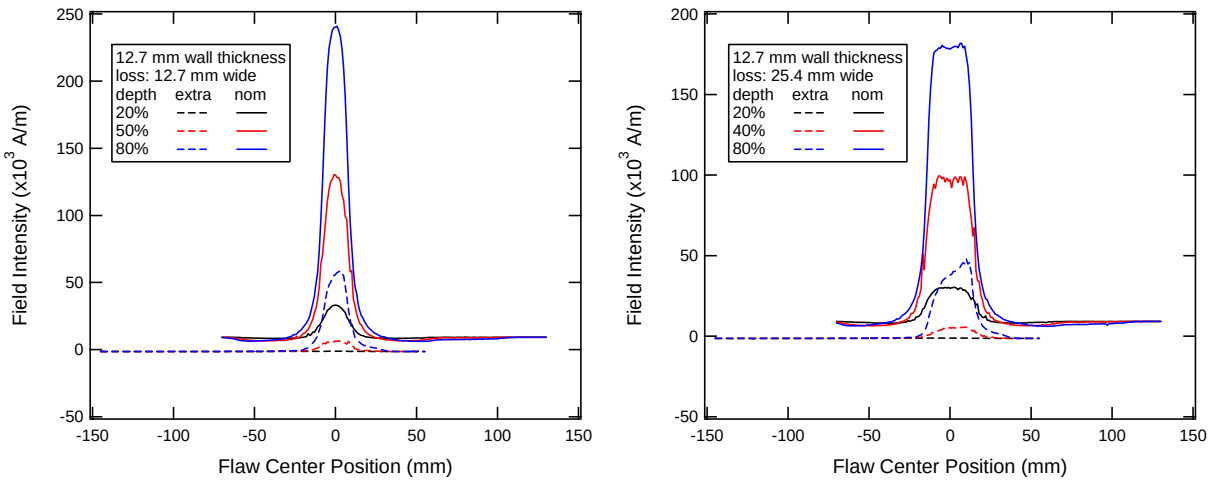

*Figure 107. Horizontal field variation with **far**-surface flaw position and depth for a magnetizable steel test material. The flaws widths are: (Left) 12.7 mm (0.5-in.); (Right) 25.4 mm (1.0-in.).*

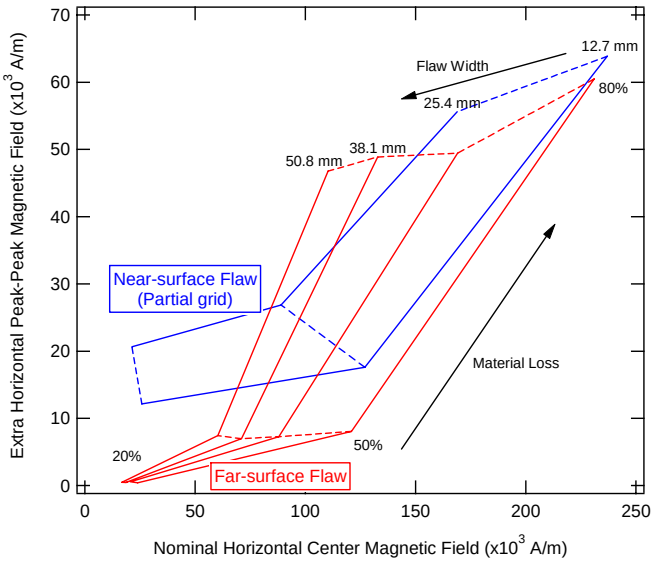

Figure 108. Measurement grids for near and far-surface flaws using a split core design.

A third approach for adapting MWM techniques to MFL methods is to replace the sensor with an MWM-Array and use the DC magnetic field to saturate the steel. Saturating the steel reduces the differential relative permeability that affects the induced eddy currents and the response to the relatively low intensity magnetic fields from the MWM-Array. This, in-turn, allows the MWM-Array to sense deeper into the steel. This is illustrated in Figure 109, which shows the depth of penetration variation with frequency, sensor geometry, and magnetic relative permeability assuming a steel electrical conductivity of 2 MS/m (3.4%IACS). The depth of penetration is limited at low frequencies by the geometry of the sensor, which is indicated here by the spatial wavelength λ. At high frequencies, the depth of penetration is limited by the standard skin depth, which varies inversely with the square root of the conductivity, permeability, and frequency. For insulating materials, such as typical polymeric coatings and air, the depth of penetration is the same as the low-frequency limit and is determined by the spatial wavelength. Reducing the relative permeability of the steel by saturating with a strong permanent magnet may allow the existing impedance measurement instrumentation to be used along with larger sensor arrays, such as the VWA001 or the FA24, to inspect through the still wall thickness. Note that saturation of the steel may be accomplished with an external yoke/core structure or possibly with a permanent magnet placed directly behind the MWM-Array. The models used to predict the MWM-Array response would need to be adapted to account for the presence of the magnet, but this may be easier to implement than the external core. This configuration is most similar to the standard operation of the MWM-Array and allowed measurements to be performed.

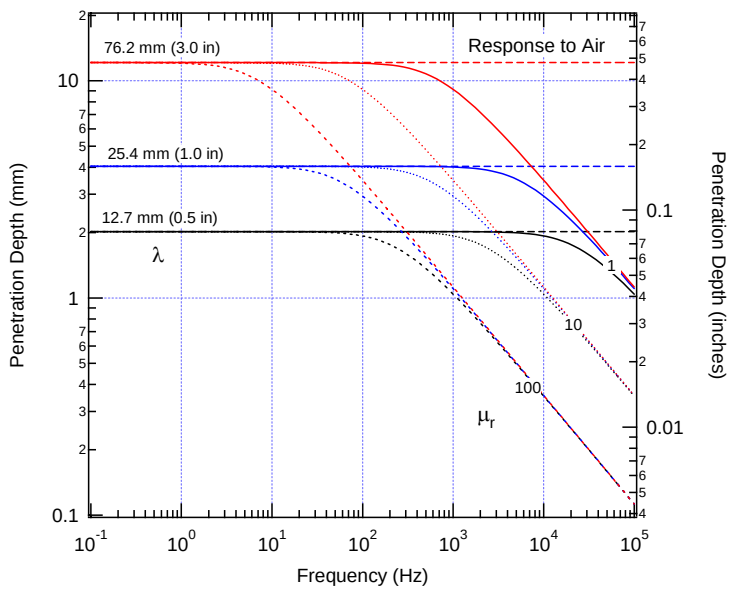

Figure 109. Depth of penetration chart for various sensor spatial wavelengths (λ) and relative magnetic permeabilities (μ_r).

Before the measurements were carried out, several simulations were performed to try to determine potential locations for placement of a permanent magnet around an MWM. The basic yoke geometry of Figure 100 was used. Two-dimensional finite element simulations were performed for a 6.35 mm thick steel plate which has a nonlinear magnetization curve. A standard material in the simulation package was used, which has a higher relative permeability of order 670 at low fields than typical pipeline steel that is of order 40-100, but this steel is still suitable for illustrating the effect of different permanent magnet locations. The differential relative magnetic permeability was calculated along the center line of the steel plate, at a depth of 3.125 mm; since the applied magnetic field from the MWM-Array is small compared to the magnetic field from the permanent magnet, this differential relative permeability gives the relevant relative permeability for the eddy current response.

Figure 110 shows the differential permeability for the yoke structure. This is a relatively large structure and is typical of MFL designs. It clearly shows the magnetic permeability in the vicinity of the sensor being substantially smaller than at the edges of the yoke. Based on the depth of penetration analysis, a material with a permeability of roughly 3 and an MWM-Array with a 12.7 mm spatial wavelength, which is the approximate spatial wavelength for an FA24, the penetration depth is limited by the sensor geometry to about 2 mm up to frequency of about 3 kHz. This suggests that this type of saturation approach could be used with an FA24 for examination of material loss on the far side of steel walls up to approximately 3.125 mm (1/8th-in.) thick. For a 25.4 mm spatial wavelength the penetration depth is limited to about 4 mm up to a frequency of about 1 kHz, which should be suitable for far side material loss inspections for thicker materials. However, this yoke structure is relatively large and prior to fabricating this type of structure some proof-of-concept demonstrations were desired for simple magnet placements.

Figure 111 shows the variation in the differential permeability associated with a permanent magnet simply placed behind an MWM-Array, which in this case was an FA24. Three commercially available rectangular magnets were considered, each of which is rectangular and 50.8 mm long. The width and thickness dimensions are 12.7 mm by 3.125 mm, 25.4 mm by 12.7 mm, and 50.8 mm by 12.7 mm. The strongest fields and the largest reduction in the differential permeability occur above the corners of the magnet. Since the magnets are magnetized in a vertical orientation for the geometry here, the beneficial aspects of a large tangential magnetic field through the bulk of the steel wall are absent. To generate the tangential magnetic field in the test material, either magnets with a different magnetization direction are required or a magnetic circuit or yoke is needed.

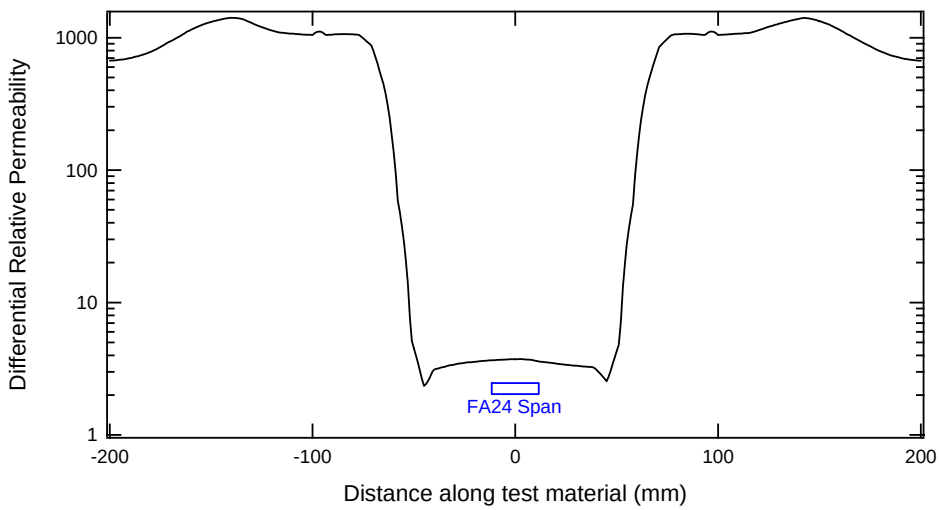

Figure 110. Differential relative permeability at a depth of 3.125 mm for the yoke geometry of an MFL design.

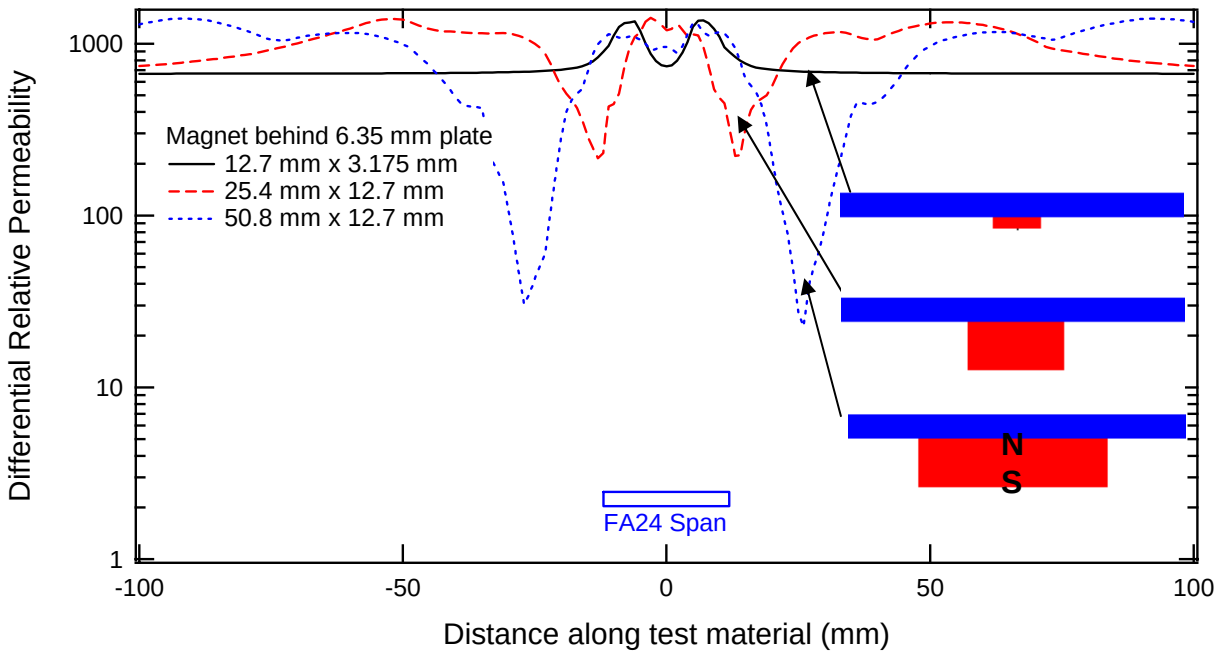

Figure 111. Differential relative permeability at a depth of 3.125 mm for a permanent magnet placed behind an MWM-Array on one side of a 6.35 mm steel plate.

To illustrate the benefits of a yoke with these magnets, consider placing a pair of either of the smaller magnets on each side of an MWM-Array. One of the magnets is flipped so that the poles are reversed and the yoke is completed with a 6.35 mm thick steel having the same properties as the pipe wall. A gap of 0.2 mm was assumed between the magnets and the steel wall under inspection. The inside edges of the magnets were located at 12.7 mm from the MWM-Array centerline, so that the magnets were relatively closed to the sensor drive windings. The differential permeability is shown in Figure 112. The use of a larger magnet leads to a greater reduction in the differential permeability; however, a reduction should still be observed with the smaller magnets. Note that the attractive force between the steel and the magnets is also larger for the larger magnets; representative maximum lift loads are 15 lbs for the 3.175 mm thick magnet and 86 lbs for the 12.7 mm thick magnet. Thus, for improving the ability to scan the sensor array, with magnets, over the material surface, there is a benefit to using the smaller magnets.

For demonstration purposes, the configuration shown in Figure 113 could be used. In this case, the magnets and yoke are placed on the back side of the test material, opposite the side with the MWM-Array. This alleviates fixture constraints associated with scanning an array with the magnets and should be able to demonstrate that the configuration leads to a reduction in permeability in the vicinity of the magnets. For the demonstration, an FA24 could be scanned over a 3.125 mm thick steel plate with an FA24 at a low frequency (e.g., 6.3 and 10 kHz or lower if possible) with and without a magnet structure placed on the back side of the steel plate. The same measurement could be performed with the magnets placed on each side of a region of far-side material loss as well.

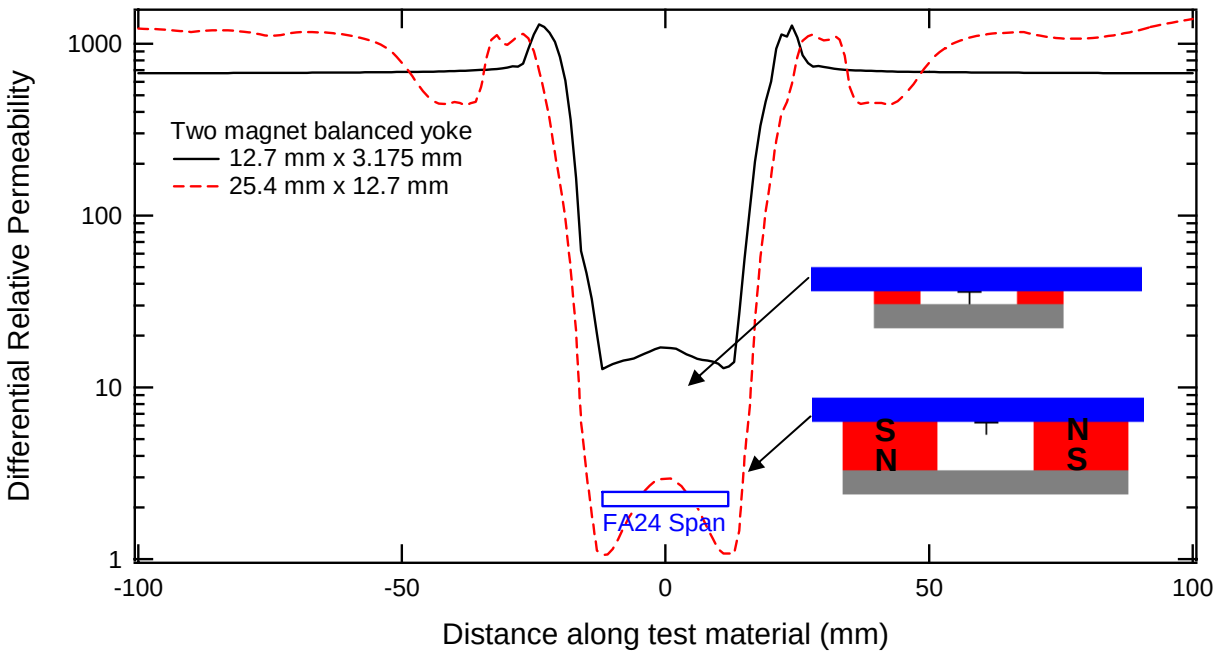

Figure 112. Differential relative permeability at a depth of 3.125 mm for a two magnet yoke geometry placed symmetrically around an MWM-Array.

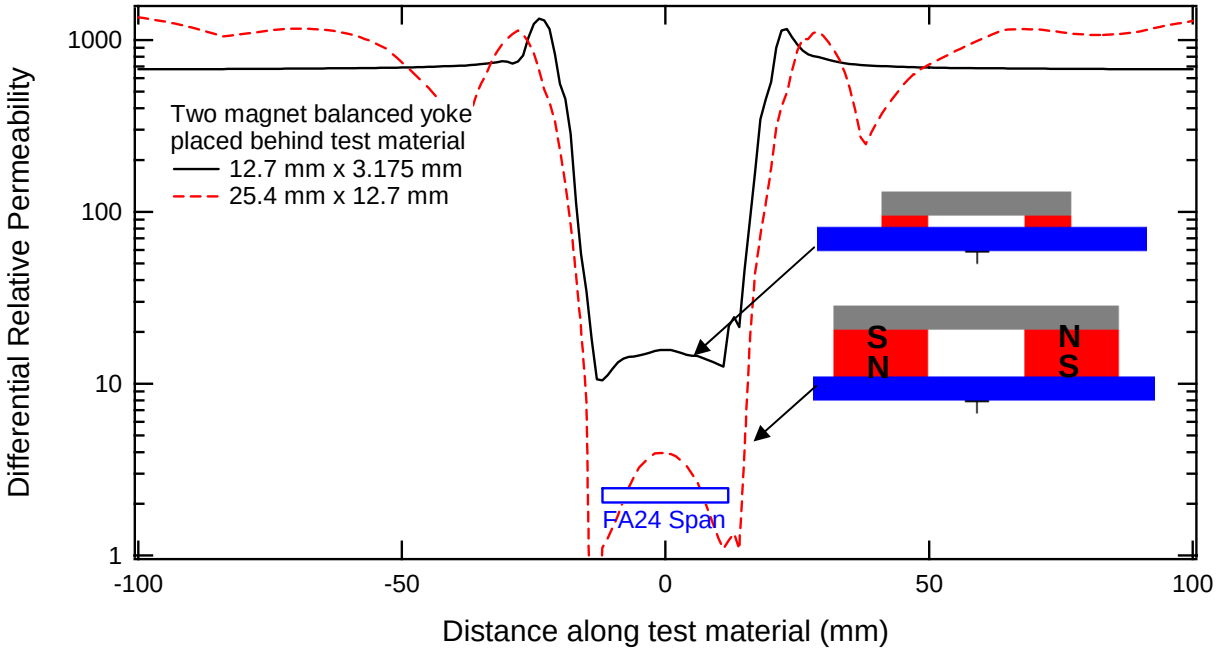

Figure 113. Differential relative permeability at a depth of 3.125 mm for a two magnet yoke geometry placed symmetrically around an MWM-Array but on the far side of the test material, opposite the MWM-Array.

Measurements were performed with an FA24 MWM-Array and several steel plates. The first set of measurements was performed on a 0.125-in. thick, 24-in. square steel plate as shown in Figure 114. A 0.04-in. layer of insulating plastic was placed over the steel plate to simulate the presence of a thin coating and to protect the sensor. An air-shunt calibration was performed. The measurement data was converted into effective permeability and lift-off values using measurement grids. When present, the magnets were placed on the back side of the steel plate, opposite the side scanned with the FA24. Figure 115 shows a representative photograph of a two magnet orientation with 0.125-in. thick steel pole pieces. The magnets were 12.7 mm (0.5-in.) thick, 25.4 mm (1.0-in.) wide, and oriented to match the magnetization direction of Figure 113. In most cases, the spacing between the magnets was about 500 mm (2.0-in.). (Note that this is larger than the 25.4 mm (1.0-in.) spacing shown in Figure 115.)

Figure 116 shows the effective properties at two frequencies (10 kHz and 100 kHz) for a single scan of the FA24, both with and without permanent magnets being present. The properties are relatively uniform before the magnets are applied, with an average relative permeability of about 36 and a lift-off of 0.04-in. The values are basically the same for both frequencies as well, which indicates that the properties are not varying with depth into the plate. However, after placing the magnets on the back-side of the steel there is a dramatic change in the effective properties. The effective permeability decreases as expected with the lowest permeability at the corners of the magnets and also in the region between the magnets. The variation in the effective lift-off is a result of the non-uniform properties in the steel not being modeled by the measurement grids; the grids assumed a thick layer of steel having uniform properties. While this grid assumption also affects the measured permeability values, these images show that the magnets are strong enough to reduce the permeability of the steel in this configuration.

Figure 117 shows a plot of permeability with position for a sense element channel that passes directly over the magnets. The reduction in permeability is similar to that predicted in Figure 113, with a significant variation in the permeability in the vicinity of the magnets and a region of approximately constant permeability between the magnets. The steel was not completely saturated, but the permeability decreased by a factor of about 8.

Figure 114. Measurement configuration for an FA24 and a large steel plate. The dimensions of the steel plate are 24-in. x 24-in. x 0.125-in.

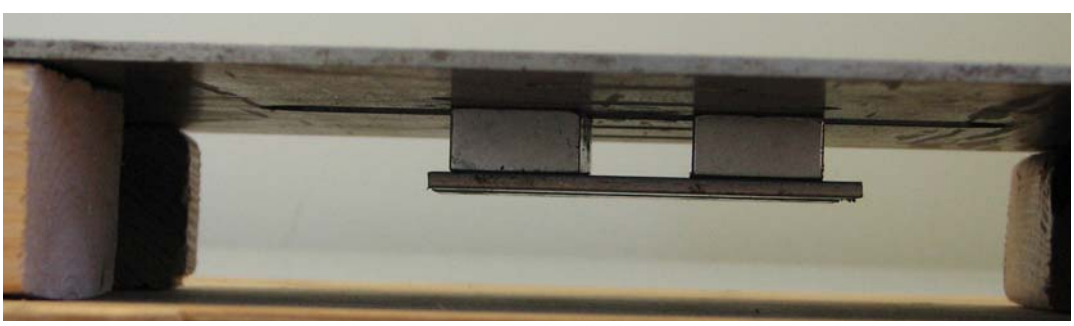

Figure 115. Photograph of the magnet geometry when the magnets are placed on the back side of the steel plates.

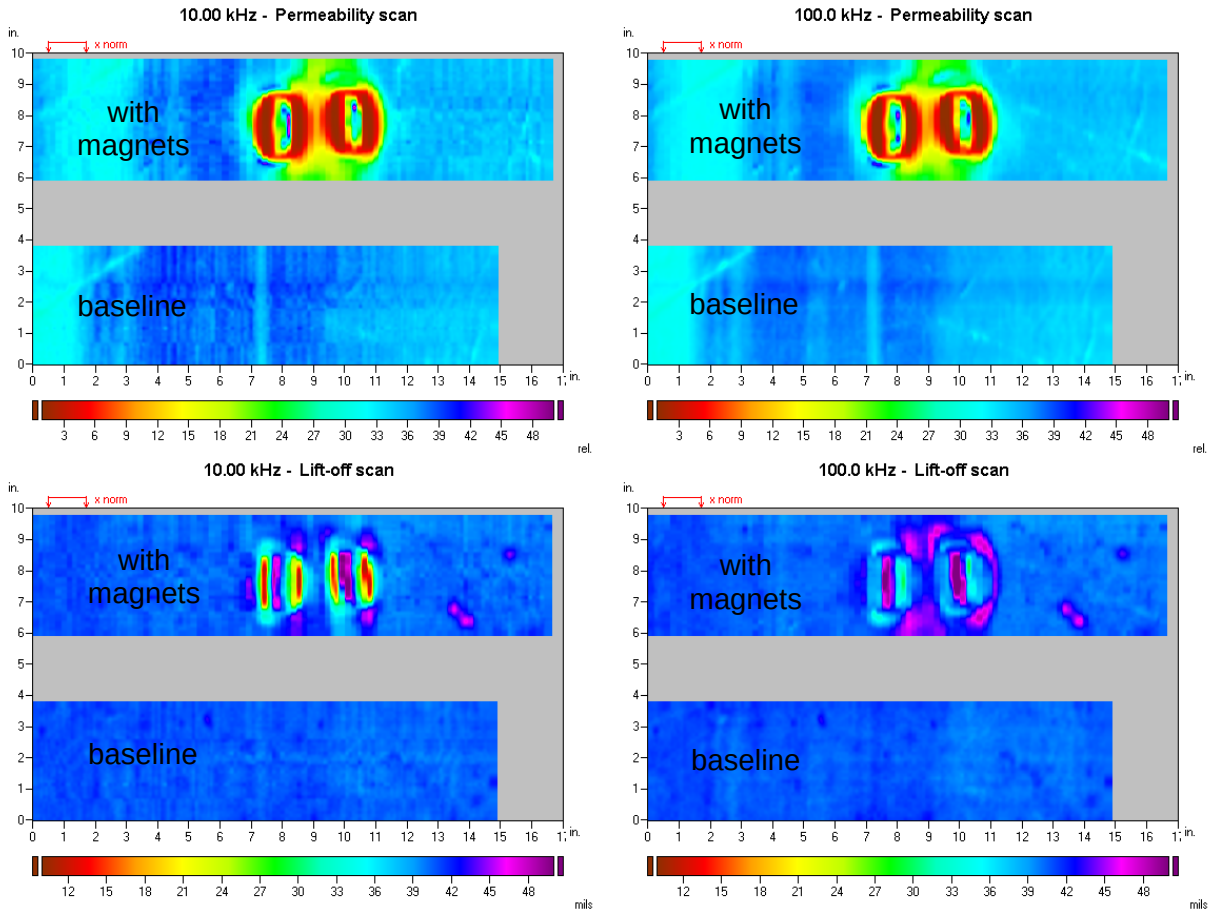

Figure 116. FA24 measurement scans with and without permanent magnets placed on the back side of a steel plate. The permeability (upper) and lift-off (lower) images were obtained for 10 kHz (left) and 100 kHz (right).

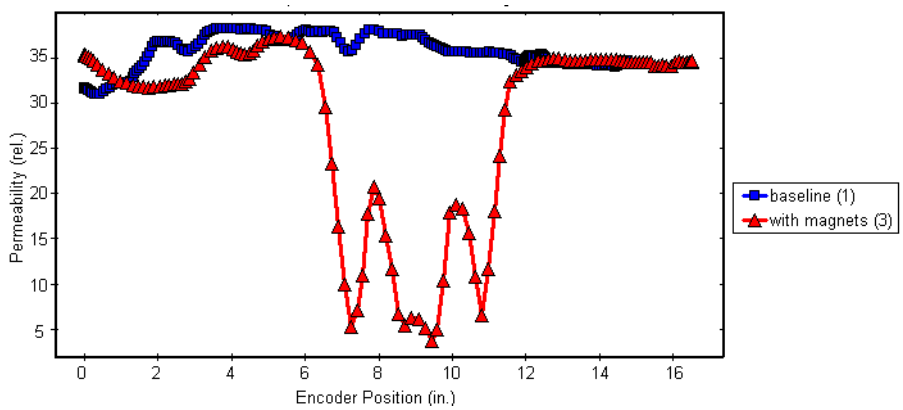

Figure 117. Permeability plot versus encoder position for a channel that passes directly over the magnets on the back-side of a steel plate. The frequency was 100 kHz.

The second set of measurements was performed on several 0.125-in. thick, 12-in. square steel plates as shown in Figure 118. Each plate has several machined regions to simulate material loss. These material loss regions were placed on the bottom so that the scanned surface was relatively smooth. The machine areas in each plate have different sizes and depths, with the deepest and largest region of material loss located near the center of the plates and with a minimum remaining steel thickness of

0.025-in. Three plates were placed side-by-side to try to minimize edge effects in the scans. As before, a 0.04-in. layer of insulating plastic was used and an air-shunt calibration was performed.

Figure 119 shows baseline scan images across the center section of two of the plates. The permeabilities and lift-offs are relatively uniform across the plates, but there is a faint shadow and change in properties associated over the machined areas. Although it is possible that the 10 kHz images reflect the plate thickness changes, these responses are most likely an effect of the machining process leading to a change in the material properties. At 100 kHz the depth of penetration of the magnetic field is less than 0.01-in., so it is unlikely that the sensor would respond to steel thickness changes for thicknesses greater than 0.025-in. at such high frequencies. Thus, these shadows are most likely caused by permeability changes associated with the machining process.

Figure 118. Measurement configuration for an FA24 and several smaller steel plates. Magnets, when present, were placed underneath the middle plate, opposite the side scanned with the FA24.

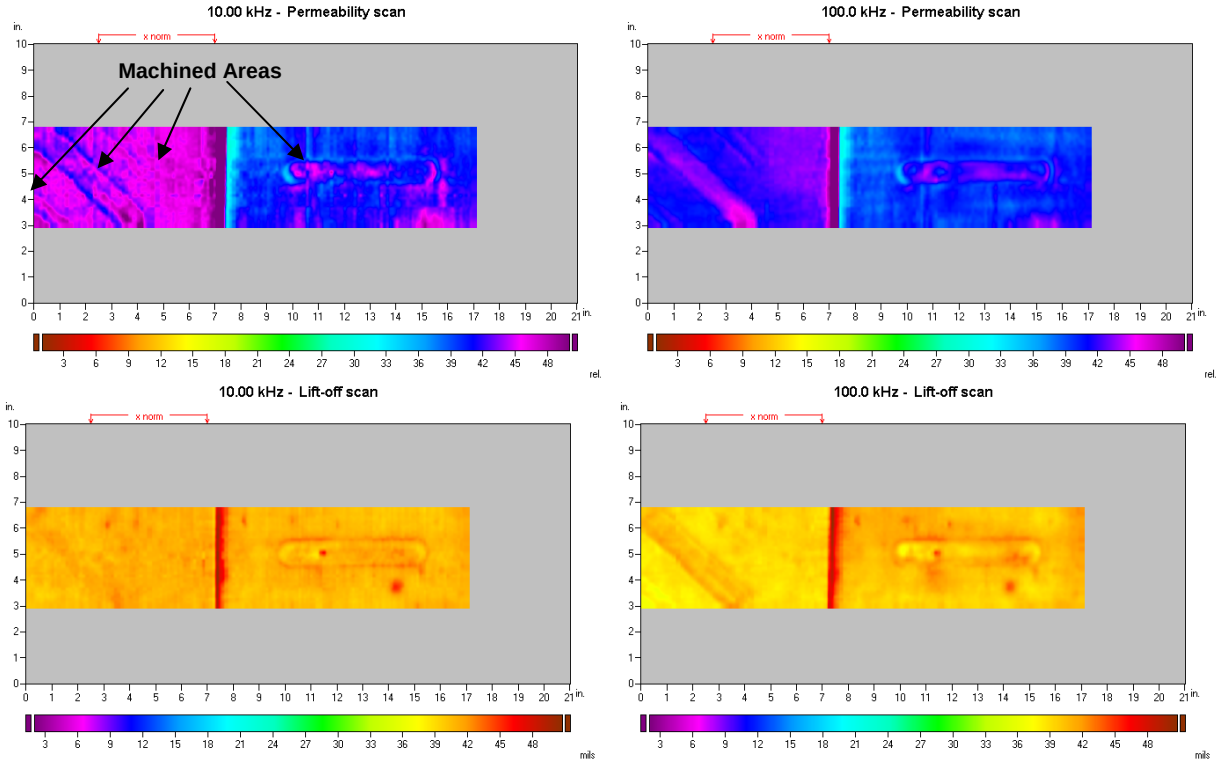

Figure 119. FA24 baseline measurement scans across the center portion of two of the 12-in. square steel plates with machined areas of material loss. The permeability (upper) and lift-off (lower) images were obtained for 10 kHz (left) and 100 kHz (right).

Figure 120 shows measurement images for the steel plates when the magnets were placed behind the center plate. In this case, the magnets were orientated parallel to the central machined-loss area and the scan direction. Four magnets were used to try to broaden the area over which the DC magnetic field was applied. Note also that the left-most plate was rotated 180º so that the orientation of the shadows associated with the machined-loss areas changed from Figure 119. Again, in the vicinity of the magnets there is a substantial reduction in the relative permeability. The non-uniform permeability also leads to noticeable spatial variation in the effective lift-off as well. In contrast with Figure 116, the permeability in the region between the magnets is not very uniform. This suggests that the thickness change in the steel plate is influencing the magnetic field distribution and hence the magnetic permeability. However, as expected the DC magnetic field itself is not very uniform; thus it is difficult to isolate the perturbation in the permeability associated with only the material loss.

While these measurements showed that a hybrid approach combining DC magnets to reduce the permeability of the steel with an MWM-Array for sensing the steel property changes is feasible, additional work is required to demonstrate the inspection capability. For example, the DC magnetic circuit should be attached to the scanning sensor fixture. This would reduce the DC field variations in the vicinity of the sensor and the effect of the large spatial variations in the magnetic permeability observed in the demonstration measurement would be absent. This should permit reliable imaging over wide areas.

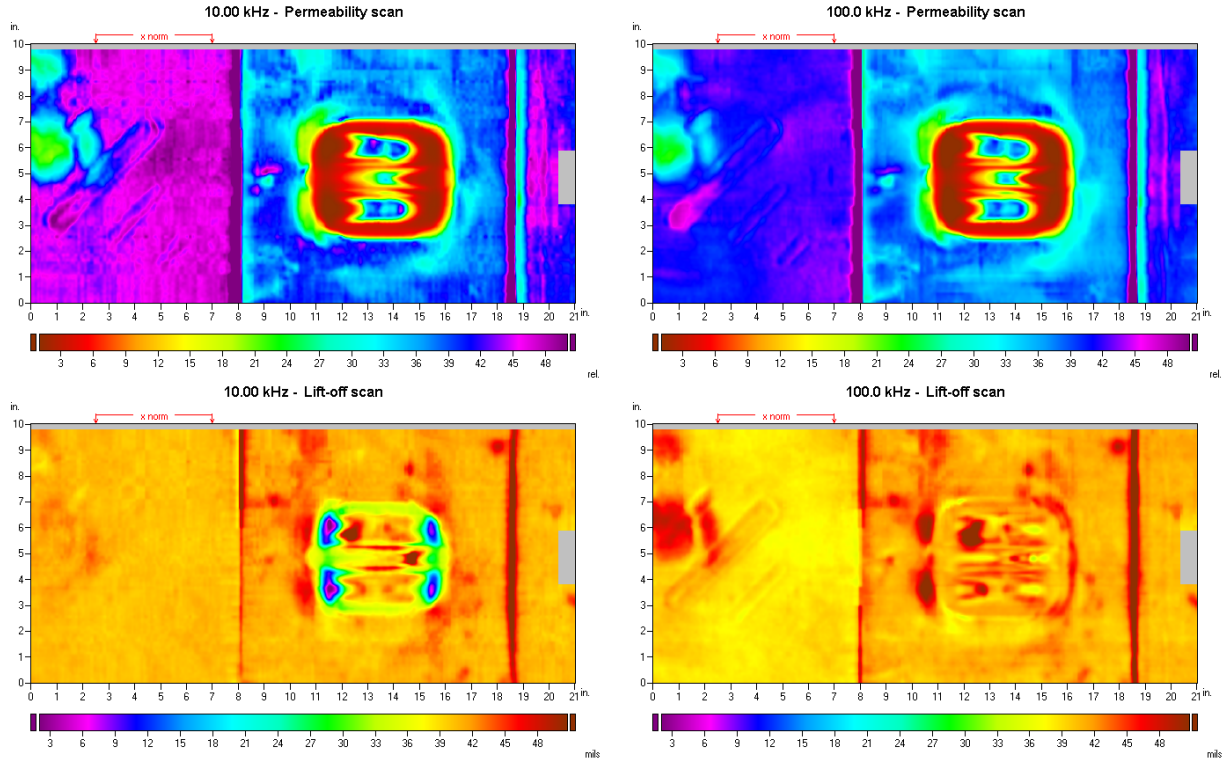

Figure 120. FA24 measurement scans across the 12-in. square steel plates with machined areas of material loss. The permeability (upper) and lift-off (lower) images were obtained for 10 kHz (left) and 100 kHz (right). Magnets were placed under the center plate.

6.4.4 Far-Surface Material Loss (Corrosion) Imaging

For inspecting through the thickness of the steel walls and also for inspecting through magnetic and/or conducting coatings or liners, low excitation frequencies are needed. Example barrier layers include aluminum weather jacket layers and corrosion resistant alloys used as internal liners. Frequencies of 1-10 kHz can be used for inspecting through nonmagnetic conducting layers but lower frequencies of order 30 Hz are needed for inspecting through the magnetic layers and the steel wall thickness. Experiments showed that the VWA001 can be operated down to approximately 1 kHz, but to achieve the low operating frequencies it is better to use sense elements that respond directly to the magnetic flux, such as magneto-resistive (MR) sensors or Hall effect devices, in place of inductive loops that respond to the time rate-of-change of the magnetic flux.

To guide our selection of the appropriate sense element, Table 5 was constructed to summarize the features, benefits, and disadvantages associated with candidate sense elements. Other sense element choices are also possible for low frequency measurements, such as SQUIDS, but these other sense elements are not considered mature enough for incorporation into a fieldable system.

A prototype 37 channel MR-MWM-Array was made available for testing in this program and used to investigate the independent measurement of lift-off, steel magnetic permeability, and steel wall thickness using multiple frequency measurements. This array has 37 MR sense elements, as shown in Figure 121(left), and is designed to fit within a large (12-in. x 6-in.) drive winding as shown in Figure 121(right). The array has a basic geometry similar to the FA24 used for high frequency/thin coating applications, but uses a larger drive winding. Through minor hardware and software adjustments, the current instrument's low frequency range was extended to 31Hz; previously, the lowest frequency for the instrument was 100 Hz. Note that at 30 Hz, the skin depth for a steel having an electrical conductivity of 5%IACS and relative permeability of 70 is approximately 6.35 mm (0.25-in.). If the measurement noise is low enough, this suggests that the instrumentation could be sensitive to a wall thickness of order 0.5-in.

In principle multiple frequency data, taken simultaneously over a 31 Hz to 3.16 kHz range, permits estimation of the wall thickness, relative permeability, wall thickness of the steel as well as the sensor lift-off. However, since the precomputed response lattices are multi-valued over the property ranges of interest, different estimation results can be obtained depending upon the frequencies and approach used. By separating the multiple unknown inverse method into two problems each having fewer unknowns, robust property estimates were obtained. Instead of using a wide range of frequencies to simultaneously estimate lift-off, thickness and permeability, it is better to use high frequencies to accurately estimate the liftoff and then lower frequencies to estimate the thickness and permeability of the material given the previously estimated liftoff.

To demonstrate an initial scanning capability, a series of measurements were performed on flat 4340 steel plates having dimensions of 12-in. by 12-in. by 0.125-in. In two of these plates, as shown in Figure 20, five regions were machined on one side of the plate to represent areas of material loss. Although the MR-MWM-Array has large dimensions compared to the plate edge effects were not an issue if the sensor array was positioned near the center of the plate. Assuming the plate thickness and that the array was not over a flawed area, it was possible to use permeability/conductivity/lift-off lattices and multiple frequency measurements to determine a nominal plate conductivity of 8%IACS. Subsequent measurements used this electrical conductivity value so that the local plate thickness, permeability, and lift-off could be estimated.

Table 5. List of benefits and disadvantages for several alternative sense elements.

Sensing Element	Features	Benefits	Disadvantages
Hall Effect	- Four terminal, solid state device capable of producing an output voltage (Vh) proportional to the product of the input current (Ic), the magnetic flux density (B) and the sine of the angle between B and the plane of the Hall sensor: Vh = K*Ic*B for 90° angle, K is the open circuit product sensitivity constant - Needs power between 0.1 and 0.2W - Operation between -273°C and 200°C.	-Geometry of the sensing element itself is very flexible making it easily adaptable to different applications -Sensing areas can be very small. Active areas as small as 0.010-in. x 0.010-in. are available	- Largest noise source is thermal. - Hall effect active element must be chosen to limit the temperature coefficient, generally trading against sensitivity. - Not as sensitive as an MR element - Relatively high power requirements
Magneto-resistive (MR)	- Based on the MR effect, where a change in resistance is caused by a change in external magnetic field. Materials commonly used (e.g.,Permalloy) can be given a preferred magnetic orientation such that a current causes the material to magnetize parallel to the direction of the current. External fields applied perpendicular to current cause the magnetization direction to rotate, the angle depending on the external field magnitude. - Needs power between 0.1 and 0.5mW. - Operation between -55°C and 200°C.	- Sensitive to fields orders of magnitude smaller than Hall Effect elements. - Low sensitivity to electrical interference due to low source resistance. - High temperature operation, and temperature deviations can be corrected with a bridge circuit design.	-Fundamental characteristic is not non-linear and hysteretic. -Operating range limited to linear region. -Presence of demagnetizing fields that increase with decreasing sense element size -Barkhausen noise lead to similar changes as MR effect. -May require periodic resetting of the sensor due to drift, possibly due to Barkhausen noise.
Giant Magneto-Resistive (GMR)	-Giant magnetoresistance is a property observed in certain magnetic superlattices, also called magnetic multilayers. Constructed with alternating layers of nonferromagnetic and ferromagnetic metal. The relative thickness of the layers is chosen such that in the absence of an external magnetic flied, the moments of neighboring ferromagnetic layers are antiparallel. As an external field is applied, the ferromagnetic layers align, resulting in lower resistance.	-Almost an order of magnitude more sensitive than MR elements	- Fundamental characteristic is not non-linear and hysteretic. - Operating range limited to linear region which typically must remain small compared to biasing voltage. - These drawbacks can be mitigated using a feedback loop.
Inductive	- Also known as the search-coil magnetometer, based on Faraday's Induction Law. As magnetic flux through a coiled conductor changes, a current is induced in the coil and a voltage is generated between its leads proportional to the rate of change of the flux. MWM is an example. - Needs power between 1 and 10mW.	-JENTEK's MWM capability well developed. -MWM can be printed on a flexible media commonly used for flexible circuits.	- Sensitivity depends on rate of change of magnetic flux through coiled conductor. The sensor is limited to higher frequencies, and when stationary, DC fields are not measurable. - Larger sensing elements than the other devices.
Inductive with Ferrite Backing	- Placing a permeable, non-conducting material, such as ferrite, as the backing of the inductive sensor amplifies the magnetic flux through the coiled conductor and the rate of change of the flux and the signal produced. Commonly used in NDT eddy-current bolt-hole probes.	-Sensitivity may be increased. However, noise sources, such as material noise are also amplified. Depending on the significant sources of noise in the application, SNR may change very little.	- Sensitivity is still directly proportional to rate of change of the magnetic flux, and therefore the sensor is still limited to higher frequencies. - Flexibility of sensor is lost

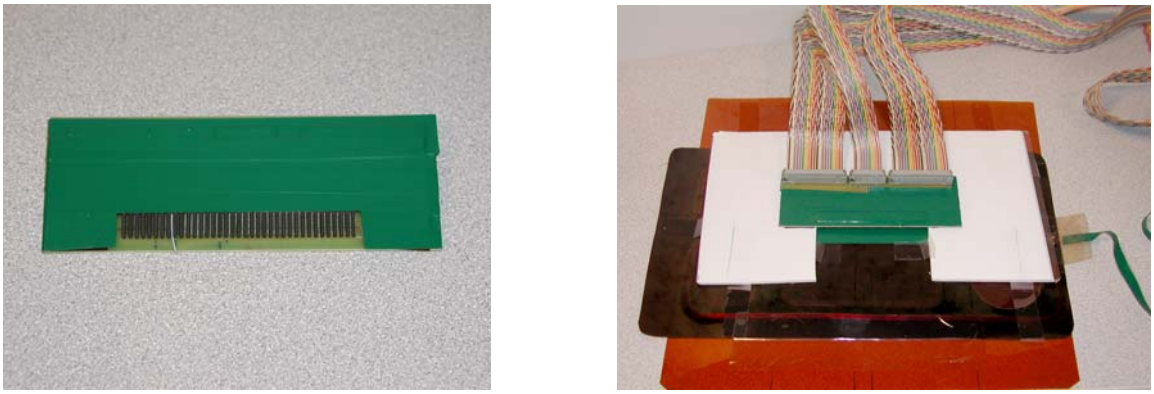

Figure 121. Photographs of a 37 channel MR sensor array (left) and the MR-Array within a large hand-wound drive winding (right).

Figure 122 through Figure 125 show representative images obtained for the multivariate inverse methods over the center material loss region which has a depth of 0.10-in. and a remaining plate thickness of 0.025-in. A 0.25-in. thick Neoprene layer was used as a simulant coating. The horizontal axes provide a measurement number since the measurements were taken at discrete intervals of approximately 0.25-in. over the plate surface. The vertical axes provide the sense element number. Frequencies of 1.0 and 2.5 kHz were used for the high frequency lift-off estimation while frequencies of 31, 100, and 316 Hz were used for the low frequency thickness estimation. In each set of images, the thickness decreases from the nominal plate thickness of 0.125-in. to approximately 0.050-in., which is approaching the thickness of the material loss region. The lift-off ranges from approximately 0.34-in., which includes the Neoprene thickness of 0.25-in. and the internal lift-off of the sense element in the array of 0.10-in.) to 0.44-in. when the material loss is on the upper surface of the plate nearest the sensor. As shown in Figure 123 and Figure 125, when the material loss is on the bottom surface of the plate (the side opposite the sensor array), the plate thickness shows the material loss but the lift-off is relatively constant. **This series of measurements demonstrates the capability of the MR-MWM-Arrays to independently determine near-surface and far-surface material loss,** for 0.125-in. thick steel layers.

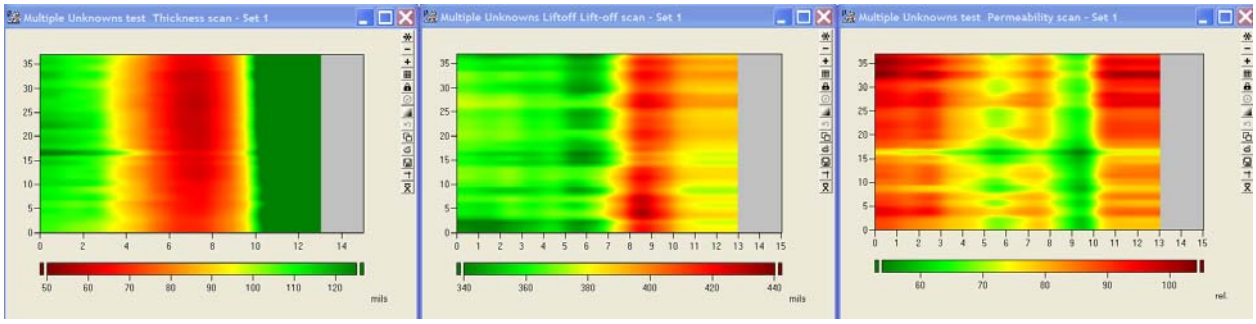

Figure 122. Representative property images for vertical slots in the upper surface of the plate showing plate thickness (left), lift-off (middle), and relative permeability (right).

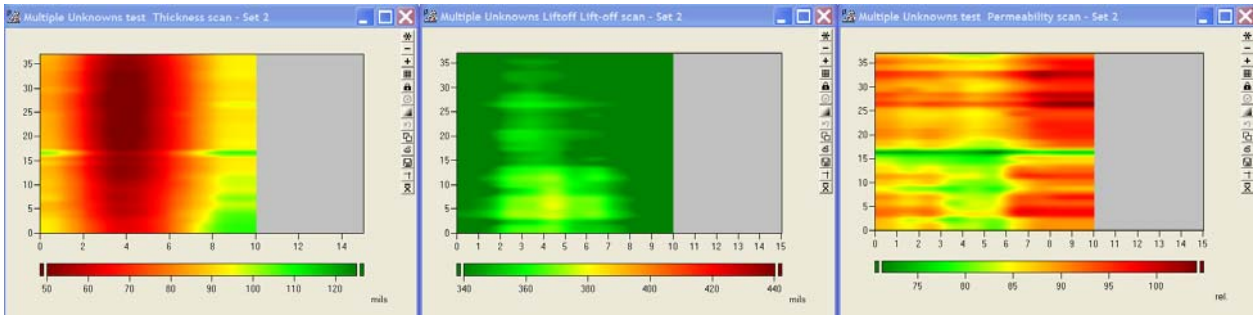

Figure 123. Representative property images for vertical slots in the bottom surface of the plate showing plate thickness (left), lift-off (middle), and relative permeability (right).

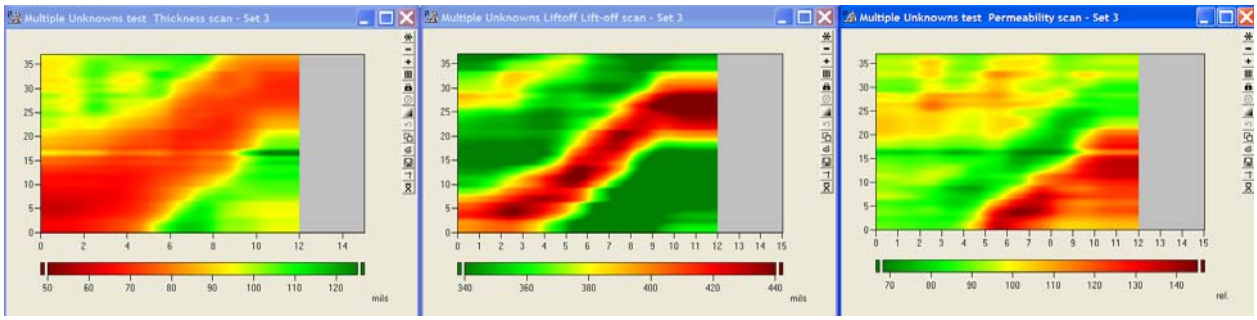

Figure 124. Representative property images for diagonal slots in the upper surface of the plate showing plate thickness (left), lift-off (middle), and relative permeability (right). (Note that the elongation of the diagonal at the ends is due to scanning in the middle in larger increments than on the ends.)

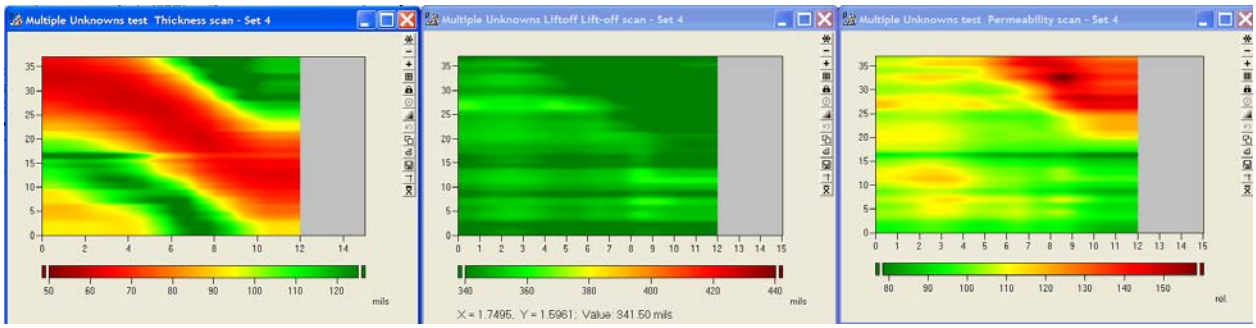

Figure 125. Representative property images for diagonal slots in the bottom surface of the plate showing plate thickness (left), lift-off (middle), and relative permeability (right).

Measurements were also performed on larger steel plate samples that did not contain machined flaws. Following the method described above, the thickness, permeability, and lift-off were estimated using an assumed value for the electrical conductivity. The estimated plate thickness is shown in Figure 126 though Figure 127 at several positions on the plates; these thickness values are in reasonable agreement with the nominal thickness and were relatively consistent for each sense element. Based on our measurements, the appropriate value for the electrical conductivity decreased with increasing plate thickness as 10%IACS for the 0.125-in. plate, 9%IACS for the 0.19-in. plate, and 7.5%IACS for the 0.25-in. plate. All of the measurements here used an air calibration and a reference calibration may help to minimize any dependence on the assumed conductivity value.

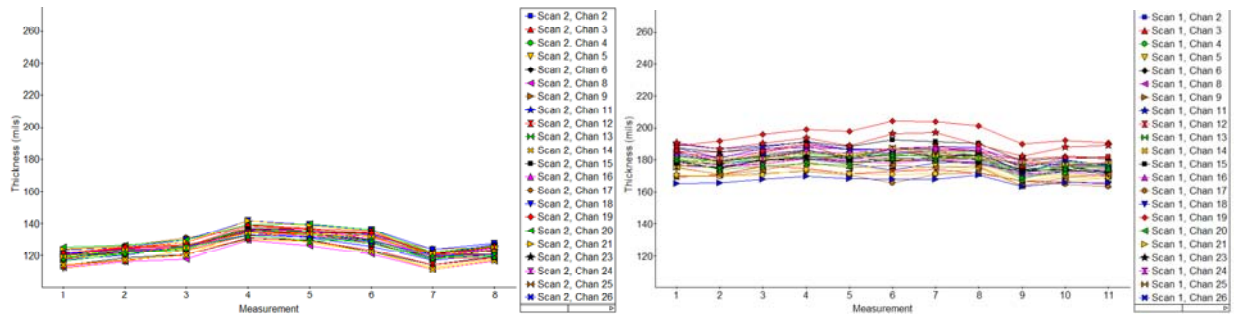

Figure 126. Plate thickness estimates at several measurement locations for (left) a 0.125-in. steel plate assuming an electrical conductivity of 10%IACS and (right) a 0.19-in. steel plate assuming an electrical conductivity of 9%IACS.

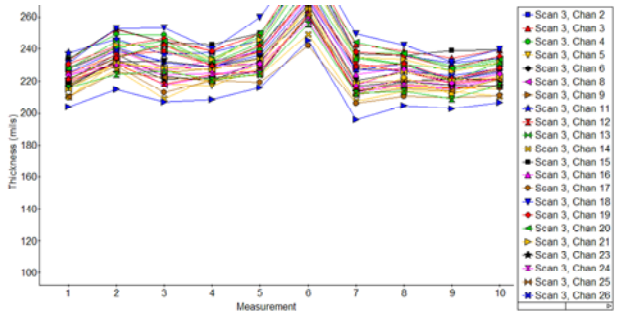

Figure 127. Plate thickness estimates at several measurement locations for the 0.25-in. steel plate assuming an electrical conductivity of 7.5%IACS.

Figure 128 shows the result of measurements on the 0.125-in. steel plate with and without an extra 0.5-in. layer of Neoprene. While the permeability estimate appears to be more reliable for the 0.25-in. layer of insulation, **the plate thickness estimate is independent of the presence of the extra Neoprene**. These results are consistent with the results of the VWA001; the gap between the drive and the MR sense element array is approximately 22 mm and, based on a 25.4 mm (1.0-in.) gap with the VWA001, reasonable results are expected for coatings thicknesses of at least 1.0-in. Ongoing work is aimed at improving this measurement capability for thicker steel walls.

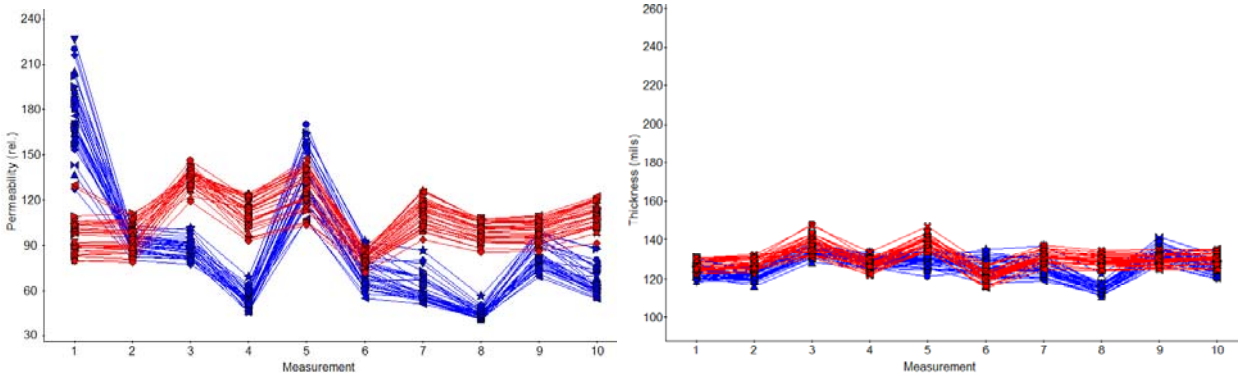

Figure 128. Permeability (left) and thickness (right) of the 0.125-in. plate with a 0.25-in. (red) or 0.75-in. (blue) Neoprene insulation layer.

For practical implementation of an MR-MWM-Array in pipeline inspections, instead of using a flat, rigid array of sense elements, a flexible array similar to the VWA001 design, would permit inspection of pipelines having different diameters. This led to the fabrication of the next generation version of the MR-MWM-Array, which has a linear array of 12 magnetoresistive (MR) sensors placed 6.35 mm (0.25-

in.) apart. Each sensor provides three outputs corresponding to three orthogonal field directions. Since this leads to 36 sensor outputs, JENTEK's standard 37-channel impedance measurement instrumentation can be used. The same drive winding used with the prototype MR sensor array was used the new MR array. Figure 129 shows a photograph of the next generation MR-MWM-Array.

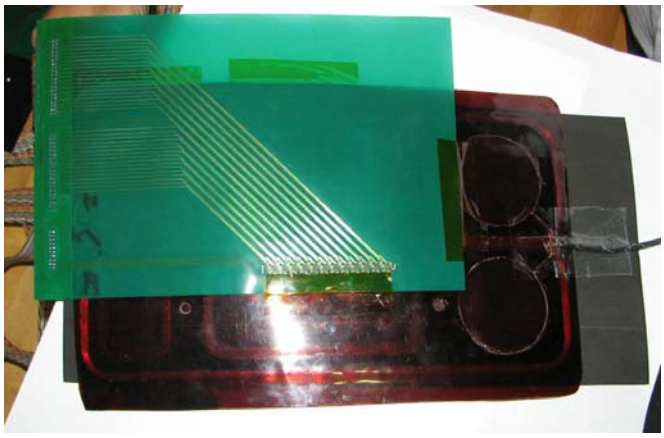

Figure 129. Photograph of the next generation MR-MWM-Array with the old (dual rectangle) drive winding placed on a flexible substrate of 0.25-in. thick Neoprene.

The sensor array configuration with a separate drive winding and sense element array is similar to that used with the VWA001 and VWA003. However, the capability to measure three magnetic field directions simultaneously provides new challenges and potentially complementary information about detected flaws. The magnetic field created by the drive winding has a large component normal to the face of each sensor. This is the orientation used in the inspections with the inductive sense elements and the MR sensors act as absolute sense elements. The other two (tangential) components of the magnetic field are substantially smaller, with the field component in the direction of the array elements ideally zero; in these orientations the MR sensors act more like differential sense elements since the fields are small unless a flaw is present. The emphasis of the preliminary measurements has been on the response to the normal fields but ongoing work will test the response to the other field components as well.

To test the next generation MR-MWM-Array, one set of measurements were made on large steel plates (approximately 24-in. x 24-in.) that did not contain machined flaws. Using multivariate inverse methods, the thickness, permeability, and lift-off were estimated using an assumed value for the electrical conductivity. Measurements were taken using frequencies from 30 Hz to 1 kHz. The sensor array was placed inside one of the drive winding loops approximately 0.5-in from the central drive winding conductor. An air calibration was performed.

Figure 130 shows the estimated thickness for several steel plates for several sensors in the MR-MWM-Array. Plates of thickness 0.125-in., 0.190-in., and 0.25-in. were used. For the 0.375-in. material, the 0.250-in. plate was stacked on the 0.125-in. plate. For the 0.565-in. material all the plates were used. A small FS33 sensor was used to determine the electrical properties of the 0.25-in. plate to be an electrical conductivity of 6.5%IACS and a relative permeability of 80. These results were comparable to those obtained with the MR-MWM-Array and there was better agreement between the different types of sensors than had previously been obtained with the older MR sensor array prototype. An electrical conductivity of 6.5%IACS was assumed for the multivariate inverse methods even though there was some plate-to-plate variability in this value. Assuming a constant electrical conductivity across different plates adversely affects the absolute accuracy of the thickness estimate, but as shown in Figure 130 the thickness estimates are reasonable. The thickness estimates are expected to improve when the constant conductivity assumption is relaxed. Figure 130 also shows that the MR-MWM-Array was sensitive to thickness of plates thicker than 0.25-in. It appears that the sensitivity to plate thickness is lost somewhere

between 0.375-in. and 0.5-in. Since at 30 Hz, the skin depth for a steel having an electrical conductivity of 6.5%IACS and relative permeability of 80 is approximately 5.6 mm (0.22-in.), lower frequencies should help to extend the sensitivity of the approach to thicker plates. Ongoing work is aimed at developing new electronics for operation below 30 Hz to enable inspection of thicker plates.

Figure 131 shows estimates for the lift-off (sensor proximity to the steel surface and which is proportional to the coating thickness) and the relative permeability of the steel plates that were obtained along with the thickness estimates of Figure 130. Insulating coatings having a thickness ranging between 0.125-in. and 0.5-in. were placed between the sensor array and the steel plate, but the plate thickness estimate was essentially constant. This indicates that the **plate thickness estimates are independent of the coating thickness** or sensor lift-off. As with the VWA001 and VWA003 sensor arrays, the gap between the drive winding and sensor array can be increased to accommodate thicker coatings. Similarly, the magnetic permeability is essentially independent of the coating thickness. However, there are substantial variations in the magnetic permeability between the plates. Some of this variation is associated with the assumed constant electrical conductivity between the plates. For the 0.125-in. thick plate, portion of the plate had been magnetized with some previous tests. This leads to a slight difference in the thickness estimates (Figure 130) depending upon the magnetization state of the steel; future work should investigate the sensitivity of the measurement approach to magnetization history, but the difference is relatively modest compared to the overall plate thickness. The magnetic permeability of the magnetized portion of the plate is relatively low compared to the non-magnetized areas (Figure 131), as expected.

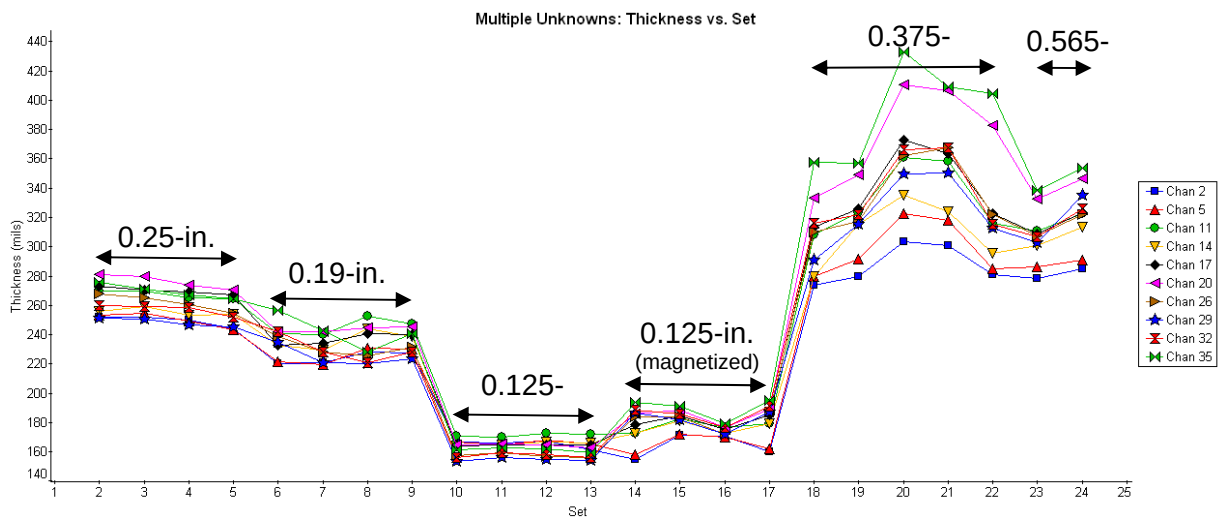

Figure 130. Thickness measurements for several steel plate combinations. Each group of 4 measurement sets used insulating coatings of thickness 0.125, 0.25, 0.375, and 0.5-in. of and the 0.250-in.

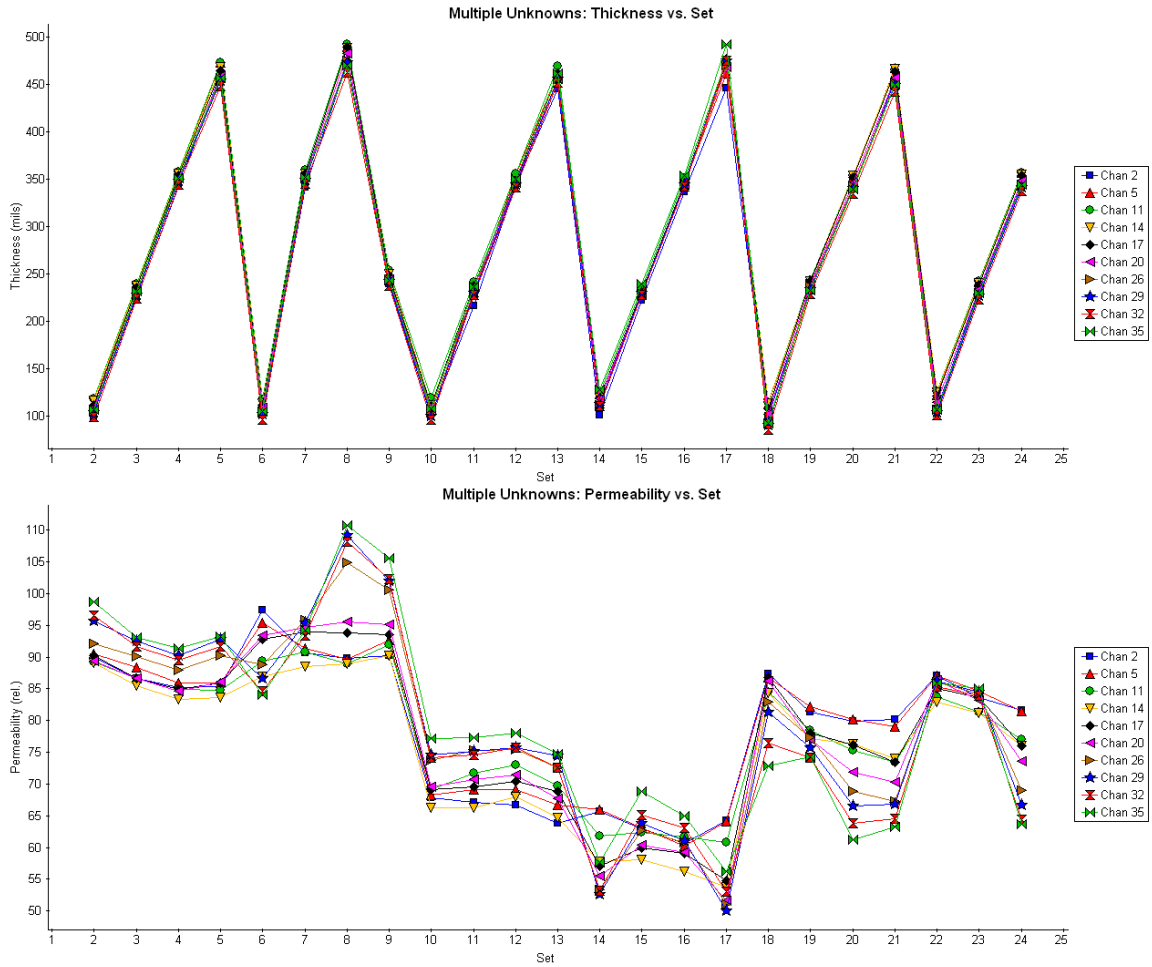

Figure 131. Liftoff and permeability estimates corresponding to Figure 130.

The flexible MR-MWM-Array of Figure 129 was then placed around a 4 ft long pipe section with internal flaws. This pipe section has an outer diameter of 6.625-in. and a wall thickness of 0.4-in. It has two rows of flaws machined into the inside surface to represent internal material loss, which was accomplished by drilling holes through the pipe on the opposite sides from the flaws. The flaws are located 90° apart and have nominal diameters of 0.5 and 1.0 inches. The flaws have depths corresponding to 25%, 50% and 75% material loss, so that the remaining wall thickness is 0.3, 0.2, and 0.1-in., respectively.

Figure 132 shows photographs of the MR-MWM-Array wrapped around the pipe section, with a 0.25-in. thick layer of Neoprene used as the sensor array substrate and placed between the sensor array and steel pipe. The sensor array and drive winding were both flexible enough to wrap around the pipe section and conformed reasonably well to the pipe contour.

For measurements with the MR-MWM-Array on the pipe section, an extra layer of 0.25-in. thick Neoprene was wrapped around the sensor array to hold it in place as shown in Figure 133. A suitable scanning fixture was not fabricated for this prototype array so an image of the pipe properties was obtained by taking a set of measurements at discrete intervals of approximately 6.35 mm (0.25-in.) over the pipe surface. Frequencies from 30Hz to 1kHz were again used for the inversion, along with an air calibration. This data is also undergoing further analysis to support follow-on work.

Despite the differences in the absolute electrical property values, measurements of the MR-MWM-Array on the pipe section and application of the multivariate inverse methods yielded

reasonable results. Images showed the wall thickness, pipe wall magnetic permeability, and sensor lift-off. Images were obtained for measurements taken over the 1.0-in. diameter internal material loss regions. The results were encouraging since they demonstrated the capability of the approach for simultaneously estimating multiple pipe wall parameters using only an air calibration. Ongoing work is aimed at reducing the measurement time for each location to demonstrate a scanning capability.

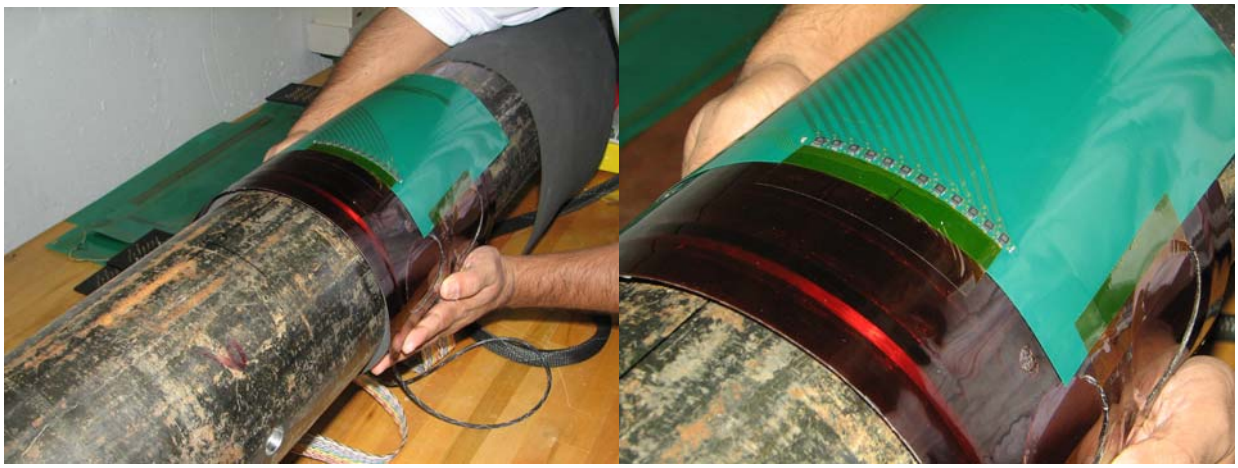

Figure 132. Photographs of the flexible MR-MWM-Array wrapped around a 6-in. diameter pipe section with several 25.4 mm (1-in.) diameter flat-bottom regions machine out of the inner surface.

Figure 133. Photograph of the flexible MR-MWM-Array wrapped around a 6-in. diameter pipe section with an extra layer of 0.25-in. thick Neoprene wrapped around the sensor array.

6.4.5 Mechanical Damage Imaging

Several measurements have shown that the MWM-Arrays can image mechanical damage in steel. These measurements involve scanning an MWM-Array over the surface, processing the data with measurement grids to obtain lift-off (sensor proximity) and permeability images of the material being inspected, and evaluating these images to determine the presence and extent of the damage. Mechanical damage appears as both an increase in sensor proximity, i.e., lift-off (associated with denting or gouging of the surface), and a variation in the local magnetic permeability (which is associated with variations in the residual stress around the damage site and other microstructure changes due to plastic deformation).

Measurements were performed on a flat steel plate to demonstrate the capability of the MWM-Arrays to image mechanical damage through thin and moderate thickness coatings. The steel plate had dimensions of 12-in. x 12-in. x 0.064-in. A hydraulic press was used to introduce a dent into the center of the steel plate. As shown in Figure 134, the 1-in. diameter punch created a shallow (0.100 in.), flat-bottomed depression, surrounded by a depressed region. For the measurements, JENTEK's small-size FA24 and the VWA001 MWM-Array sensors were scanned over the plate. The smaller size of the FA24 makes it more suitable for obtaining high spatial resolution images of damage through relatively thin coatings while the VWA001 is more suitable for thicker coatings. For both sensors, an air-shunt calibration was performed. This type of calibration uses a measurement in air and a measurement with a shunt sensor in which the sense elements are shorted. The frequency used for both sensors was 100 kHz.

Figure 135 shows B-scans across the damage region, and the corresponding images. The peak change in lift-off is approximately 0.100-in., consistent with caliper measurements on the plate itself. Based on some of the other research with thicker coatings, as long as the damage region is large compared to the coating thickness, the change in the lift-off associated with the damage provides a reasonable measure of the depth of the damage. Additional information is available in the magnetic permeability plot. There is a considerable change in the magnetic permeability beyond the region where the lift-off change was apparent (about an extra 1.0-in. in this case). This probably reflects the residual stress distribution; additional work is required to confirm the spatial variation in the stress distribution for this type of damage, either with finite element analysis of the stress or through a comparison to literature, if available.

Figure 134. (Left) A dented steel plate. (Right) Plate with an FA24 MWM-Array and a 0.020-in. plastic sheet.

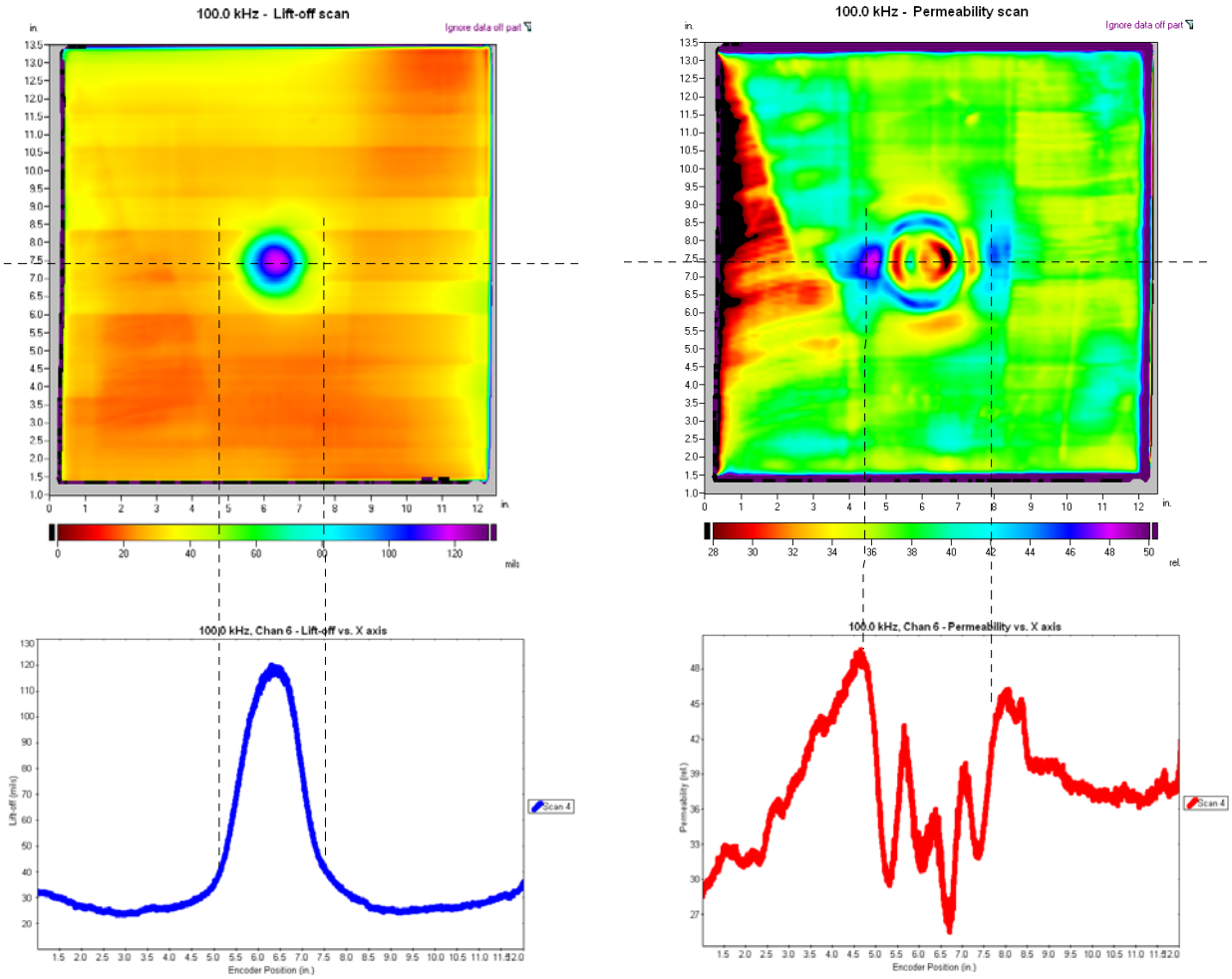

Figure 135. B-Scans of lift-off (left) and permeability (right) across the damage region with an FA24.

Similar measurements were performed with the VWA001 and a thicker (0.5-in.) coating. For these measurements, the gap between the drive and sense elements was set to 1.0-in. The VWA001 was placed in a 2D scanner for creating scan images. Due to limitations on the y-axis for the scanner and the large sensor array size, data was only obtained for angles of -45° and +45°. In these scans, the surface of the Neoprene coating, used to create the 0.5-in. stand-off, was found to be somewhat sticky and an additional 0.010-in. Mylar shim was placed over the surface to facilitate scanning.

Figure 136 shows a set of images obtained with the VWA001 and an angle of -45°. The mechanical damage region is again visible in both the lift-off and permeability. However, the spatial resolution of the images is lower and there is a broadening of the responses to the regions compared to the FA24. This is illustrated more clearly in Figure 137, which plots the responses for both the FA24 and VWA001 relative to the center of the mechanical damage region. The lift-off change is the measured lift-off minus the nominal coating thickness. For the VWA001, the response is slightly wider because the fields diffuse or spread out further through the thicker coating. The peak is also smaller for the VWA001 as the coating thickness becomes comparable to the size of the damage region and a shape correction should be used with the measurement grids. For the permeability, there is a shift in the baseline responses that may be a result of the sensor array being large compared to the sample and edge effects as part of the sensor is off of the plate. For the VWA001, the sharp features in the spatial permeability variations are averaged together so that more gradual trends are observed.

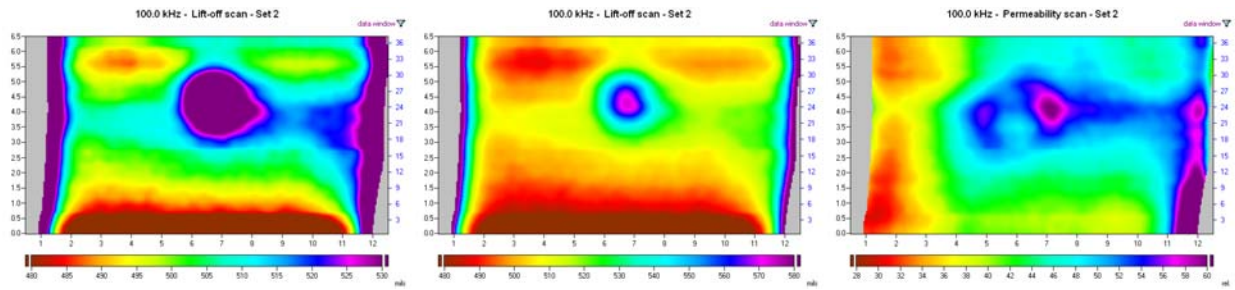

(a) (b) (c)

Figure 136. Mechanical damage scan images for (a and b) lift-off [in two different color scales] and (c) permeability for a VWA001 MWM-Array having a 1-in drive-sense gap.

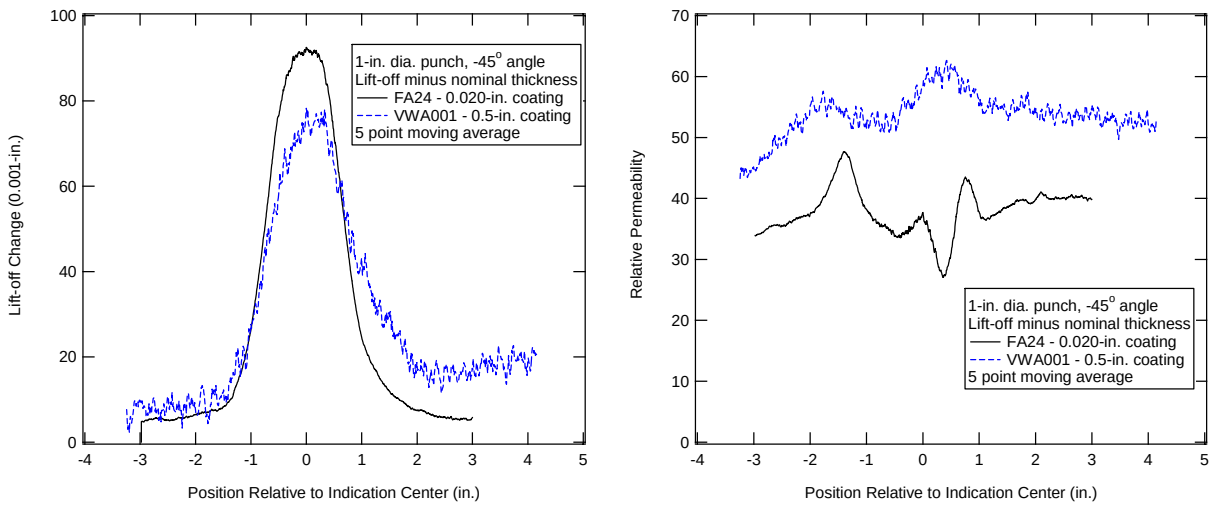

Figure 137. Comparison plots of the lift-off change (left) and relative permeability (right) for FA24 and VWA001 sense elements that pass over the center of the mechanical damage region.

Several scans were also performed over a region on the outer surface of the 16-in. diameter pipeline section. This region included a small (< 0.5-in. diameter) area of mechanical damage as shown in Figure 138. Two 0.010-in. plastic shims were attached on to the sensor with double-sided tape (each 0.003-in.) and two pieces of 0.010-in. plastic were placed on the surface of the pipeline section. As shown in Figure 139, the mechanical damage appears as a change in both the lift-off and permeability.

Figure 138. Area of mechanical damage on the external section of a pipe section.

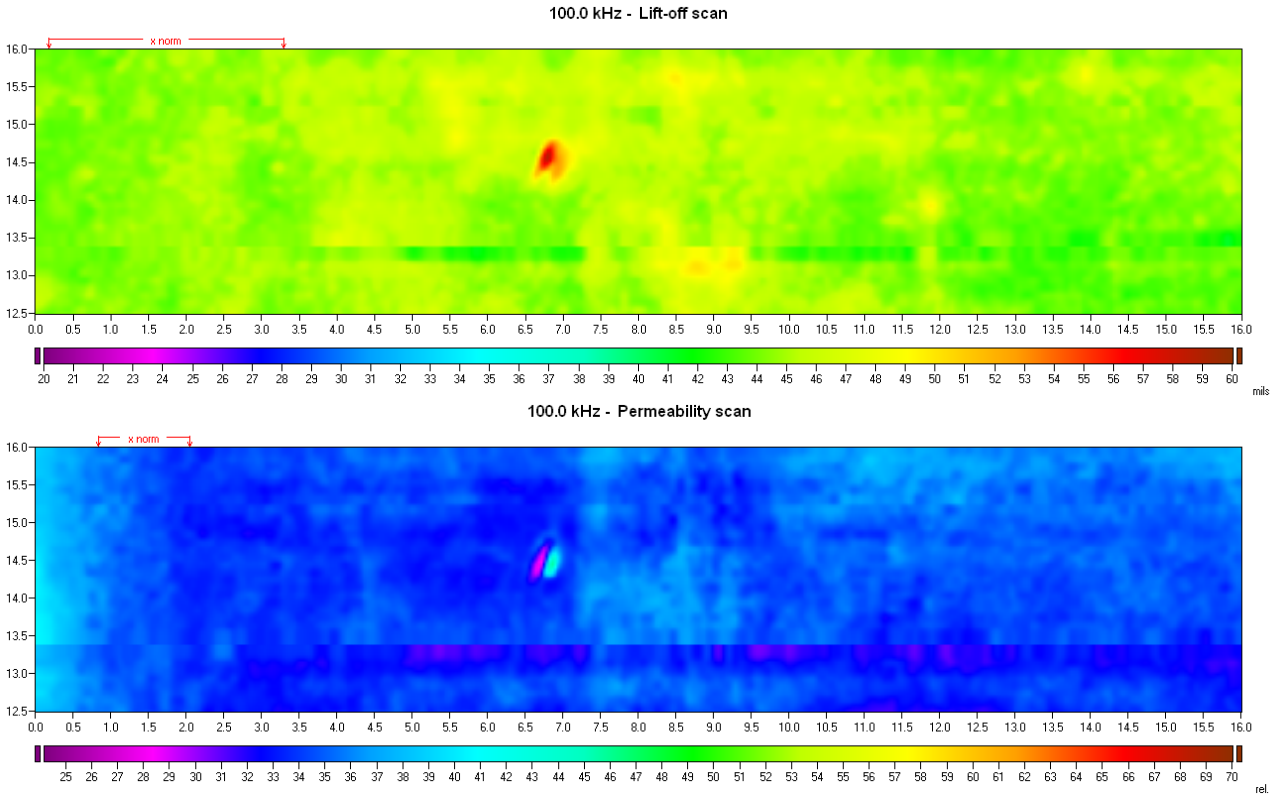

Figure 139. Lift-off scan image (upper) and permeability image (lower) of the region of external mechanical damage using an FA24 MWM-Array through a 0.046-in. coating.

6.5 Technology Transition

Transitioning of this technology for in-service use in pipeline applications has several components. One component has been to review the requirements expected for ILI tools. Another is the development of a commercialization plan that reviews the technology status and also reviews likely transition paths. Another component is the development of training information and standards since this information needs to be available to facilitate widespread adoption by the industry. Finally, preparing papers and presenting at conferences increases awareness of the technology throughout the industry. Each of these components is described below.

6.5.1 ILI Tool Requirements

For integration into an ILI platform and in order to help guide the adaptation of the MWM-Array technology for ILI applications, numerous discussions were held with ILI providers, such as NDT Systems and Services, Applus/RTD, Weatherford, and SIG. Typical tools have the following features:

- Power availability – tethered tools have an umbilical that provides power and data communication while untethered tools are battery powered. The battery powered tools have stricter limits on power consumption as well as weight and size.
- Data acquisition rate – depends upon the number of sense elements, travel speed, and desired image resolution.
- Image resolution – a typical image resolution for damage is 1 cm by 1 cm. Other requirements typically include 10% material loss with an accuracy of 5%.
- Physical dimensions of instrument – the maximum weight is platform dependent and the size is determined primarily by the pipelines to be inspected. We expect the initial focus to be on 16-inch diameter pipelines.
- Travel speed – 0.5 mph for the tethered tools and 5-10 mph for untethered tools, but untethered tools have been operated at lower speeds of order 0.1-0.2 mph.
- Length of line to be inspected – this affects the storage requirements for the acquired data as well as the power requirements for the tool.

As an example, a typical tool with standard MFL sensing methods has a spatial resolution of 8-12 mm circumferentially and 2-3 mm axially, but some tools have a smaller circumferential spatial resolution. Eddy current and ultrasonic methods are increasing being used in conjunction with the MFL; the circumferential spatial resolution is typically 4 and 8 mm, respectively. For example the eddy current sensor provides information about the presence of internal corrosion. The sensors are typically placed on spring-loaded structures which allows the tool to be collapsible and navigate through bends while continuing to maintain sense element proximity to the pipe wall surface. A typical tool is able to collapse to 25% from the inner diameter of the pipe and needs to be able to pass through 1.5 diameter bends.

6.5.2 Commercialization Plan

In broad terms, the commercialization plan involves demonstrations of inspection capability for prototype systems that can be made available to lead customers. The plan started with demonstrating advancements and adaptations of the MWM-Array sensor technology in laboratory and field settings. These demonstrations are planned to have increasing levels of complexity of the integrated components with an eventual goal of implantation into a stand-alone tool. This capability would be transitioned into a commercial product either through a partnerships with existing ILI service providers, possibly with the MWM-Array technology installed in a module that become a part of the entire tool, or as stand-alone devices, such as an instrumented cleaning tool with limited inspection capabilities.

The development path for the technology has been to demonstrate technology advancement through a series of capability demonstrations. Initial demonstrations have focused on tethered platforms so that the power requirements would not be an issue. These have also focused on the use of high frequency measurements with the measurement grid methods to demonstrate the capability to image and

characterize near-surface (internal) material loss from the inside and local material property changes through measurements of the magnetic permeability. The first pull test used a single MWM-Array and a cable for data transmission to an impedance instrument kept outside the pipeline. The second pull test used two MWM-Arrays and impedance instrumentation integrated into the prototype tool so that only a power cable was required. Ongoing work is aimed at developing the capability to accommodate a larger number of MWM-Arrays for complete circumferential coverage and inclusion of a battery pack for self-contained power, and hardening of the instrumentation to withstand the immersion environment of the tool. In the mean time, additional efforts are focused on developing the low frequency measurement technology for assessing the far-surface (external) material loss and imaging of damage through conducting coatings such as corrosion resistant alloys. This technology would be incorporated into the ILI tools as it becomes available.

We are also continuing to investigate instrumentation enhancements that are expected to be necessary to transition this technology to field use. For example, the second generation prototype ILI tool used in the expanded field capability demonstration incorporated two MWM-Arrays mounted on each side of a prototype tool. While this demonstration established the feasibility of the use of multiple MWM-Arrays and impedance measurement instrumentation integrated into a tool, additional MWM-Arrays are need for complete circumferential coverage. Additional MWM-Arrays will also require additional instrument boards for monitoring each channel in parallel and/or some level of multiplexing. We are continuing to evaluate the tradeoffs between instrument size and complexity versus required data acquisition rates. Other factors being reviewed with a vision toward transitioning the technology are the mechanical requirements, such as the MWM-Array size that will be suitable for passage through typical bends, and usage considerations, such as battery operation and memory requirements for storage of acquired data.

6.5.3 Development of Industry Standards and Training Information

To help transition and establish a basis for the technology, a standard guide was drafted for imaging of damage in metallic materials using flexible eddy current sensor arrays. The guide covers the use of model-based sensor arrays and is suitable for damage inspections with and without coatings and/or insulation between the sensor array and the metallic material of interest. It reviews factors that need to be considered as part of the examination procedure as well as standardization and calibration procedures along with the associated verification of the system performance for a particular application. The guide is generic enough to cover crack detection, material loss, and SCC imaging.

After the standard was completed, it was submitted to ASTM International for approval as an NDE procedure involving eddy current sensor arrays. ASTM International, particularly Committee E07 on Nondestructive Testing, is an appropriate standards organization since this committee is responsible for the maintenance of existing standards and development of new standards related to inspection methods. It is also our understanding that for specific applications the inspection requirements using this type of array will be specified in documents from other organizations, such as API. The standard was not accepted at the first round of balloting because it was too considered too broad to be practice that describes a specific examination procedure; consequently, the standard was converted into a guide, which is intended to be a broad description of a methodology. This approach is expected to lead to standard practices that describe the details of examinations for specific applications, but the initial standard should help to establish the use of imaging eddy current sensor arrays as a mature technology suitable for field implementation.

For the training manuals, JENTEK has general manuals that cover basic operation of the equipment and software. Presentation slides also cover the fundamentals for eddy current sensing methods and the use of Grid Measurement Methods. Specific manual and presentation information will be generated as necessary for the inspection of steel pipeline walls. This includes information about the scanning fixtures, selection of the sensor array configurations and operating frequencies, software configurations, measurement grids being used, and considerations for estimating damage conditions.

6.5.4 Increased Industry Awareness of the MWM-Array Technology

Ongoing work is aimed at increasing awareness of the capabilities of imaging eddy current sensor arrays, and the MWM-Array technology in particular, throughout the industry. This includes preparing papers for publication, presenting at conferences and workshops, and participating in industry forums. Example technical meetings that have been attended include the 2010 PRCI Pipeline Program Research Exchange Meeting, the 2010 and 2011 International Pipeline Conferences, the 2008, 2009, 2010, and 2011 Fall ASNT Conferences, and the 2010 Chevron NDE Forum.

6.5.5 Recommendations for future work

This program demonstrated the technical feasibility of incorporating the MWM-Array technology into an ILI tool. This included the capabilities for a high spatial imaging resolution and also the use of model-based methods for reducing calibration/standardization requirements and data conversion into meaningful material or geometric properties. However, additional development is required for commercial application of this technology into an ILI tool. The areas of development include:

1. Increase the number of channels to provide complete coverage. Figure 140 provides a conceptual drawing of this type of tool. This may be accomplished by adding a trailing caboose to house the power supply, data storage and computer processing units. This will accommodate the increased number of impedance channels.
2. Develop methods for higher data throughput per channel to increase the maximum speed of the tool through the pipe.
3. Include on-board power onto tool and reduce power consumption for battery operation of instrumentation. The "trailing caboose" configuration of item 1 could accommodate on-board power with a separate module for housing the batteries.
4. Improved durability and hardening of the instrument, including sealing for environmental protection in oil and gas environments and shock protection.
5. Enhance durability of the sensor articulating mechanisms. This could be included in item 4 but the focus is on the mechanisms that affect the sensor array proximity to the pipe wall surface.
6. Enhance position encoder technology.
7. Detailed evaluation of requirements for passing through bends in pipelines.
8. Integrate low frequency measurement technology for pipeline wall thickness measurements. The high frequency measurements performed in the first and second pull tests demonstrated the capability to image near surface (internal) damage and material loss, but a low frequency measurement is required for far surface (external) damage assessment. This imposes different constraints on the power consumption, sense element types, and data acquisition rates than the high frequency measurements.
9. Continued discussion with established ILI service providers. It is anticipated that involvement of at least one established ILI service provider will increase the likelihood of transitioning this technology into commercial platforms.

Items 1 and 2 could be considered the next steps leading to another pull test, with the objectives of the pull test being complete circumferential imaging of the internal pipe wall surface at pull speeds and data acquisition rates typical for ILI tools. This could also include Item 3, but the pull test could still have a tethered instrument. Items 3 and 4 would develop the necessary capabilities for autonomous operation and could be followed by a demonstration in a flow loop facility. This flow loop demonstration would probably also require items 5-7. Item 8 for low frequency measurement capabilities would be integrated into the ILI tool as the technology becomes available but should involved separate pull tests.

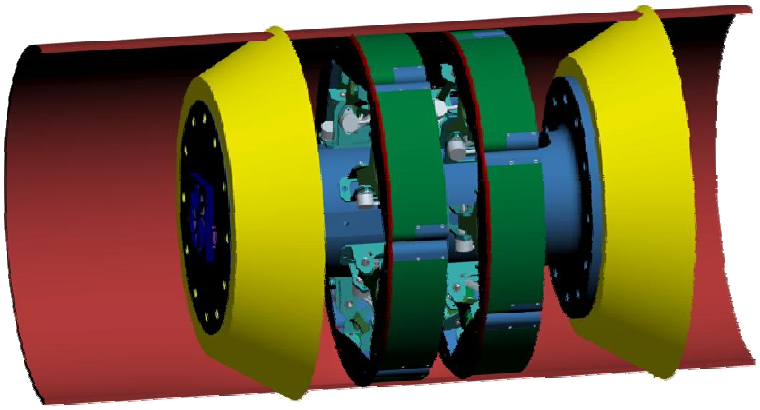

Figure 140. Concept for a full-coverage tool. The sensor array modules used for the 2nd pull test (Figure 19) are arranged in two rows of six arrays to provide complete circumferential coverage of the pipe.

6.6 References

1. N. Goldfine, V. Zilberstein, T. Lovett, "Pipeline & Piping Damage Mapping and Tracking using High-Resolution Imaging MWM-Arrays," ASNT International Chemical and Petroleum Industry Inspection Technology (ICPIIT) X Conference, Houston, TX, June 20-23, 2007.
2. N. Goldfine, "Magnetometers for Improved Materials Characterization in Aerospace Applications," *Materials Evaluation*, Volume 51, No. 3, March 1993.
3. N. Goldfine and D. Clark, "Introduction to the Meandering Winding Magnetometer (MWM) and the Grid Measurement Approach," SPIE NDE Techniques for Aging Infrastructure and Manufacturing, Scottsdale, Arizona; Dec., 1996. SPIE Proceedings, Vol. 2944, 1996. pp. 186-192.
4. N. Goldfine, et al., "Surface Mounted Periodic Field Current Sensors for Structural Health Monitoring," SPIE, Smart Structures and Materials NDE for Health Monitoring and Diagnostics, Newport Beach, California; March 2001.
5. N. Goldfine, V. Zilberstein, A. Washabaugh, D. Schlicker, I. Shay, D. Grundy, "Eddy Current Sensor Networks for Aircraft Fatigue Monitoring," *Materials Evaluation*, Volume 61, No. 7, July 2003, pp. 852-859.
6. U.S. Patent Nos. 5,453,689, 5,629,621, 5,793,206, 5,966,011, RE39,206, 6,784,662, 7,049,811, 7,385,392, 7,467,057, and pending patents.
7. Haus, H.A. and J.R Melcher, Electromagnetic Fields and Energy, Prentice Hall, Englewood Cliffs, NJ, 1989.
8. N. Goldfine, Y. Sheiretov, D. Schlicker, A. Washabaugh, "Rapid, Nonlinear "System" Identification for NDT, Using Sensor Response Databases," *Materials Evaluation*, Vol. 66, No. 7, July 2008.
9. N. Goldfine, A. Washabaugh M. Windoloski, V. Zilberstein, "Replacing magnetic particle and liquid penetrant inspections with high resolution MWM-Array eddy current imaging," ASM AeroMat Conference and Exposition, Baltimore, MD; June 26-27, 2007.
10. "Mechanical Damage, Final Report", submitted to U.S. DOT, PHMSA, Office of Pipeline Safety under delivery order DTRS56-02-D-70036 in April, 2009.